

University of Nottingham
UK | CHINA | MALAYSIA

TWO-PHOTON POLYMERIZATION OF ALGINATE HYDROGELS FOR APPLICATIONS IN CELL CULTURE

Irene Henning, MSc

Thesis submitted to the University of Nottingham

for the degree of Doctor of Philosophy

School of pharmacy

September 2019

Acknowledgements

To my supervisors for giving me the opportunity to do my PhD at the University of Nottingham. A special Thank you to Mischa Zelzer who did not only supervise me but was also a great moral support throughout the project.

To my collaborators Mahetab Amer who performed the cell culture experiments with human mesenchymal stem cells and Jonathan Moore who synthesised the photoinitiator P2CK.

To my colleagues across the school of pharmacy, Additive manufacturing and the Centre for Biomolecular Sciences (CBS) with whom I shared this exciting and challenging journey.

To my family for their infinite love and support who always help putting things back into perspective.

To my friends who made this time in Nottingham a beautiful and unforgettable experience.

Abstract

This work presents two-photon polymerization (2PP) of microstructured 3D hydrogels using alginate for the first time. Alginate is one of the most prevalent biopolymers used for hydrogels due to its biocompatibility, reversible ionic gelation and natural abundance. 2PP enables the fabrication of structures with sub-micron feature size, on the scale of single cells. Combining the high resolution of 2PP with the hydrogel properties of alginate, enables control of the mechanical and geometrical properties of artificial micro-environments.

To provide a curing mechanism using 2PP, alginate is functionalised with methacrylate groups using an amidation reaction. The 2PP photoresist is composed of methacrylated alginate dissolved in water and a cyclic benzylidene ketone-based photoinitiator, P2CK, developed for efficient 2PP of biocompatible water-soluble photoresists.

To investigate the 2PP characteristics of methacrylated alginate, various photoresist compositions were systematically studied in relation to the alginate concentration, the viscosity and the degree of functionalisation with crosslinking groups of alginate. This revealed that higher degrees of functionalised alginates featured lower polymerization- but higher damage-threshold powers resulting in the largest dynamic power ranges. Increasing concentrations of alginate reduced the deformation of all alginate hydrogels. Stable 3D hydrogels could be fabricated using at least two weight percent for alginates functionalised with 30 percent or more methacrylate groups. Optimal printing parameters were identified for alginate photoresists that enable efficient 2PP of hydrogels with high structural integrity. An unprecedented resolution for alginate hydrogels was

demonstrated with minimal linewidths down to 175 nm for two weight percent alginate with 30 percent functional groups.

The alginate hydrogels were probed for potential cytotoxic effects on bacterial and mammalian cells. A representative for Gram-negative and a Gram-positive bacteria grown on a set of different micro-topographies resulted in distinct differences of bacterial attachment which could be exploited to prevent bacterial growth. The microfabricated alginate hydrogels were further shown to support the growth of human mesenchymal stem cells (hMSCs) with first results indicating that microstructures influence the attachment and morphology of hMSCs cultured for 48 hours.

2PP of alginate allows for precisely engineering artificial cell environments which may enable novel tissue engineering strategies and microbiology investigations. The increased understanding of the variables influencing 2PP of alginate will inform and accelerate the development of other novel water-based photoresists for 2PP.

Table of contents

List of figures **ix**

List of tables **xiv**

1 Introduction **1**

1.1 Hydrogels for biomedical applications 1

1.2 Materials used for hydrogels 4

1.2.1 Synthetic polymers 4

1.2.2 Biopolymers 5

1.3 Additive manufacturing of hydrogels 10

1.3.1 Bioprinter systems 10

1.3.1.1 Inkjet printer 11

1.3.1.2 Extrusion printer 12

1.3.2 Photolithography 13

1.3.3 Two-photon lithography 15

1.3.3.1 Two-photon absorption 15

1.3.3.2 Two-photon polymerization 18

1.3.4 Two-photon polymerization of hydrogels 21

1.3.4.1 Water-soluble photoinitiators for 2PP of hydrogels . 23

1.3.4.2 Synthetic polymers for 2PP of hydrogels 25

1.3.4.3 Biopolymers for 2PP of hydrogels 28

1.4 Thesis rationale 37

2 Methodology 39

2.1 Two-photon polymerization 39

2.1.1 CAD design and structure optimisation 39

2.1.2 Sample preparation and development 41

2.2 Microscopy techniques for studying microfabricated structures 43

2.2.1 Bright-field microscopy 43

2.2.2 Scanning electron microscopy 43

2.2.2.1 Cryogenic SEM 44

2.2.2.2 SEM imaging of cells 44

2.2.3 Confocal fluorescence imaging 45

2.3 Viscosity measurements using a liquid handler 45

2.4 Raman spectroscopy 46

2.5 Bacterial cell culture 47

2.5.1 Bacterial growth 47

2.5.2 Bacterial attachment assays 47

2.5.3 Colony forming unit (CFU) count to determine number of viable bacterial cells 48

2.5.4 Encapsulation of living cells 48

2.6 Mammalian cell culture 49

3 Chemical modification of alginate to facilitate two-photon polymerization 51

3.1 Introduction 51

3.2 Experimental Methods 53

3.2.1 Synthesis of methacrylated alginate 53

3.2.1.1 Alginate amidation using 2-chloro-4,6-dimethoxy-1,3,5-triazine (CDMT) 54

3.2.1.2 Alginate amidation using carbodiimide chemsitry . 54

3.2.2 ^{1}H NMR characterization 55
3.2.3 Gel permeation chromatography 56
3.2.4 Two-photon polymerization of methacrylated alginate 56
3.3 Results and Discussion 56
3.3.1 Synthesis and characterization of methacrylated alginate . . . 56
3.3.2 Photo-crosslinked alginate and the capability for additional modifications 60
3.3.3 Determining the degree of functionalisation of methacrylated alginate 63
3.3.4 Gel permeation chromatography 65
3.3.5 Two-photon polymerization of methacrylated alginate 66
3.4 Conclusions 68

4 Two-photon polymerization of alginate hydrogels 69
4.1 Introduction 69
4.2 Experimental methods 74
4.2.1 Two-photon polymerization 74
4.2.1.1 Polymerization- and damage- threshold power and dynamic power range 74
4.2.1.2 Processing window 75
4.2.1.3 Deformation ratio of 2PP alginate hydrogels 76
4.2.1.4 Minimal linewidth 76
4.3 Results and discussion 79
4.3.1 2PP of methacrylated alginate hydrogels 79
4.3.1.1 Viscosities of methacrylated alginate 79
4.3.1.2 Polymerization- and damage- thresholds 80
4.3.1.3 Dynamic power range 84
4.3.1.4 Processing window for alginate hydrogels 86

4.3.1.5 Minimal linewidth 88
4.3.1.6 2PP voxel shape affect the 3D hydrogel structure . . 91
4.3.1.7 Cryo-SEM of hydrated alginate hydrogels 93
4.3.1.8 Raman spectroscopy to determine the degree of conversion of hydrogels 96
4.3.1.9 Deformation ratio of 2PP alginate hyrdogels 97
4.4 Conclusions 100

5 Two-photon polymerized hydrogel structures for applications in cell culture 102

5.1 Introduction 102
5.2 Experimental methods 104
5.2.1 Design rationale of hydrogel microstructures 104
5.2.2 Confocal image analysis of encapsulated bacteria 106
5.3 Results and Discussion 106
5.3.1 Bacterial growth 106
5.3.1.1 Bacterial growth in the presence of monomers and photoinitiators used for 2PP 106
5.3.1.2 Microstructured hydrogels affect bacterial attachment 109
5.3.1.3 Encapsulating bacteria in BSA/gelatin based hydrogel microstructures 119
5.3.2 Mammalian cell culture 121
5.4 Conclusions 129

6 Conclusion 130

References 132

Appendix A Appendix 1 145

List of figures

1.1 Histogram showing the exponential increase in publications per year related to hydrogels. 2

1.2 Biological extracellular matrix and synthetic hydrogels involving reversible chemistries. 3

1.3 Chemical structures of widely used synthetic polymers for biomedical applications. 5

1.4 Overview of most common biopolymers for biomedical applications. . 6

1.5 Pubmed queries for hydrogels based on most commonly used biopolymers. 7

1.6 Chemical structures of most commonly used biopolymers for hydrogels. 8

1.7 Schematic of inkjet and extrusion based bioprinter. 12

1.8 Simplified schematic of UV lithography set-up compared to two-photon lithography set-up. 14

1.9 Portrait of Maria Göppert-Mayer. 16

1.10 One-photon absorption (1PA) versus two photon absorption (2PA) . . 17

1.11 Scanning electron micrograph of the first 2PP microstructures fabricated. 18

1.12 Schematic of photo-polymerization of a hydrogel by free radical chain polymerization 19

1.13 Chemical structures of latest advancements in water-soluble photoinitiators for 2PP with low cell toxicities. 24

1.14 Scaffold seeded with cells by means of laser-induced forward transfer (LIFT). 26
1.15 Two-photon induced degradation and complete erosion of photodegradable hydrogels. 27
1.16 Optical microscopy images of free-standing BSA microstructures made from BSA photoresist with and without viscosity enhancer. 29
1.17 Entrapping living bacterial cells within 2PP hydrogel microstructures. 30
1.18 2PP of three-dimensional scaffolds from photosensitive gelatin to support the adhesion and differentiation of MSC's for applications in tissue engineering. 31
1.19 Viability of cells encapsulated in gelatin-based hydrogel structures produced by 2PP. 31
1.20 Comparison of swelling-related deformation between Gel-MOD and Gel-MOD-AEMA. 32
1.21 Microscopic images of 2PP hyaluronic acid (HAGM) scaffold geometries. 33
1.22 Fluorescence images of 2PP fabricated structures based on HA-Tyr with EosinY. 34
1.23 Optical microscope images of ring-like microstructures fabricated of photosensitive CHGM hydrogel using 2PP. 35
1.24 Two-photon patterning of photodegradable hydrogels. 36

2.1 Laser path of simple cube structure showing the slicing and hatching distance. 40
2.2 Schematic of the typical voxel shape of a 2PP reaction volume. 41
2.3 Schematic of 2PP procedure for the microfabrication of hydrogels . . 42
2.4 2PP sample prepared on a sample holder. 43
2.5 Schematic of encapsulating bacteria in 2PP hydrogel. 49

3.1 Schematic of the chemical modification of alginate to facilitate two-photon polymerization 53
3.2 ^{1}H NMR spectra of AEMA, alginate and methacrylated alginate . . . 58
3.3 ^{1}H NMR spectra in D_2O of methacrylated alginate obtained by using CDMT based chemistry. 59
3.4 ^{1}H NMR spectra in D_2O of A) Irgacure 2959, B) methacrylated alginate before and C) after UV irradiation 61
3.5 ^{1}H NMR spectra in D_2O of alginate modified with 2-aminoethyl methacrylate and L-alanine benzyl ester 62
3.6 Gel permeation chromatography (GPC) of unmodified and modified alginate 65
3.7 Photoresist composed of methacrylated alginate, water-soluble 2PP optimized photoinitiator P2CK and water. 66
3.8 2PP of methacrylated alginate with precipitated P2CK 67
3.9 Example structure of successfully two-photon polymerized (2PP) alginate hydrogel. 68

4.1 Schematic of increasing Degrees of Functionalisation (DoF) of alginate against increasing alginate concentrations. 70
4.2 Schematic of possible crosslinking mechanisms of methacrylated alginate 71
4.3 Gaussian profile representing the light intensity in the central disk of a diffraction pattern created by a circular aperture. 78
4.4 Laser path simulation of ladder structure to determine the minimal linewidth in relation to the laser power applied. 78
4.5 Method of determining polymerization- and damage- threshold powers for a photoresist. 81

4.6 Polymerization- and damage- threshold powers for varying degrees of functionalisation of methacrylated alginate as a function of different alginate concentrations. 83
4.7 Dynamic power ranges for varying degrees of functionalisation of methacrylated alginate and different concentrations. 85
4.8 Processing windows for three different concentrations of Alg-MA30 . 86
4.9 SEM images of 2PP alginate hydrogels in the shape of the letter 'A'. . 88
4.10 Scanning electron micrographs of ladders printed with increasing laser powers for each ladder step from left to right. 89
4.11 Line width of varying concentrations of Alg-MA 30 as a function of the laser power 90
4.12 SEM images of microstructures printed with different objectives . . . 92
4.13 Varying aspect ratio of voxel forming 3D structure 93
4.14 Bright-field and SEM image of 2PP alginate hydrogel of 'ALGINATE' 94
4.15 Comparison of dry and hydrated 2PP alginate hydrogels using Cryo-SEM. 95
4.16 Raman spectra obtained for alginate hydrogel, methacrylated alginate and P2CK 96
4.17 Confocal images of 2PP fabricated alginate hydrogel cubes. 98
4.18 Deformation ratio of 2PP alginate hydrogels 99

5.1 CAD design of microstructured surface featuring short micro-pillars with 8 μm spacings. 105
5.2 CAD design of microstructured surface inspired by Topochip design 1008. 105
5.3 Growth curves for *P. aeruginosa* 107
5.4 Colony forming units (CFU) for *P. aeruginosa* in 200 μL LB medium. 109

5.5 Representative scanning electron micrographs of *S. aureus* growing on microstructured alginate hydrogels with short pillars and variable spacings. 111
5.6 Bacterial total cell count of *S. aureus* growing on microstructured alginate hydrogels with short pillars and variable spacings. 112
5.7 CAD files of topography designs and bright-field images of 2PP alginate hydrogels 113
5.8 Representative fluorescence images of *P. aeruginosa* growing on microstructured alginate hydrogels 114
5.9 Number of bacteria attached to the different surfaces. 115
5.10 SEM micrographs of *P. aeruginosa* growing on microstructured alginate hydrogels. 117
5.11 Bacterial cell count of *P. aeruginosa* attached to microstructured alginate hydrogels based on SEM micrographs. 118
5.12 Confocal fluorescence images of *P. aeruginosa* cultured in hydrogel microarchitectures 120
5.13 Bright-field and fluorescence images of microstructured alginate hydrogels with various topographies 122
5.14 Confocal micrograpghs of live/dead stained hMSCs grown for 48 hours on microstructured alginate hydrogels. 124
5.15 Cell number per surface determined for live/dead stained cells. 125
5.16 Close-up images of confocal micrographs of live stained hMSCs grown for 48 hours on microstructured alginate hydrogels. 126
5.17 SEM images of hMSCs growing on microstructured alginate hydrogels. 128

A.1 Bright-field images of energy dose array for 2% and 3% w/v Alg-MA30 with the associated processing windows. 146

List of tables

1.1 Comparison of Additive Manufacturing methods used for biomedical applications that are suitable for hydrogels. 11

3.1 Integration of methacrylate and Irgacure 2959 peaks 64

3.2 Actual methacrylation and methacrylation efficiency 64

4.1 Viscosities of various alginate concentrations and DoF of alginate with methacrylate groups 80

A.1 Raw viscosity values for various alginate concentrations and DoF of alginate with methacrylate groups. 146

Chapter 1

Introduction

1.1 Hydrogels for biomedical applications

According to the International Union of Pure and Applied Chemistry (IUPAC), a gel is defined as a "non-fluid colloidal network or polymer network that is expanded throughout its whole volume by a fluid". Thus, a hydrogel is a gel that swells in water while it is composed of a three-dimensional (3D) hydrophilic polymeric network that can be either of natural or synthetic origin.

Hydrogels can be classified into physical or chemical hydrogels depending on the chemistry of the precursors used to form the polymeric network. Physical gels are characterised by crosslinking based on secondary forces including ionic, hydrogen bonding or hydrophobic forces. These network interactions are reversible, meaning that physical hydrogels can easily disintegrate as a result of changing environmental conditions (e.g. pH, temperature or pressure). Chemical crosslinking requires a low-molecular-weight agent mixed with a polymer to form a polymer network and is considered to provide permanent gels because a covalently crosslinked network is very stable [1].

Hydrogels for biological use have been first introduced by Wichterle and Lim in 1960, defining three major prerequisites that are still valid today. Firstly, the 3D structure

of the hydrogel has to facilitate the desired water content. Secondly, the hydrogel should be inert to biological material and lastly, be permeable to solutes [2]. Their research resulted in the first clinical application of hydrogels namely the production of soft contact lenses [3]. An interest in hydrogels for biomedicine was born, slowly gaining more attention by researchers until an exponential growth in the number of publications started around the 1990's up until today. Figure 1.1 illustrates the number of publications that result from a pubmed search for the key word 'hydrogel' between 1960 up until 2018. The medical use of hydrogels cover a wide range of applications today, from soft contact lenses to surface coatings, wound dressings, drug delivery systems and tissue engineering [4][5][6].

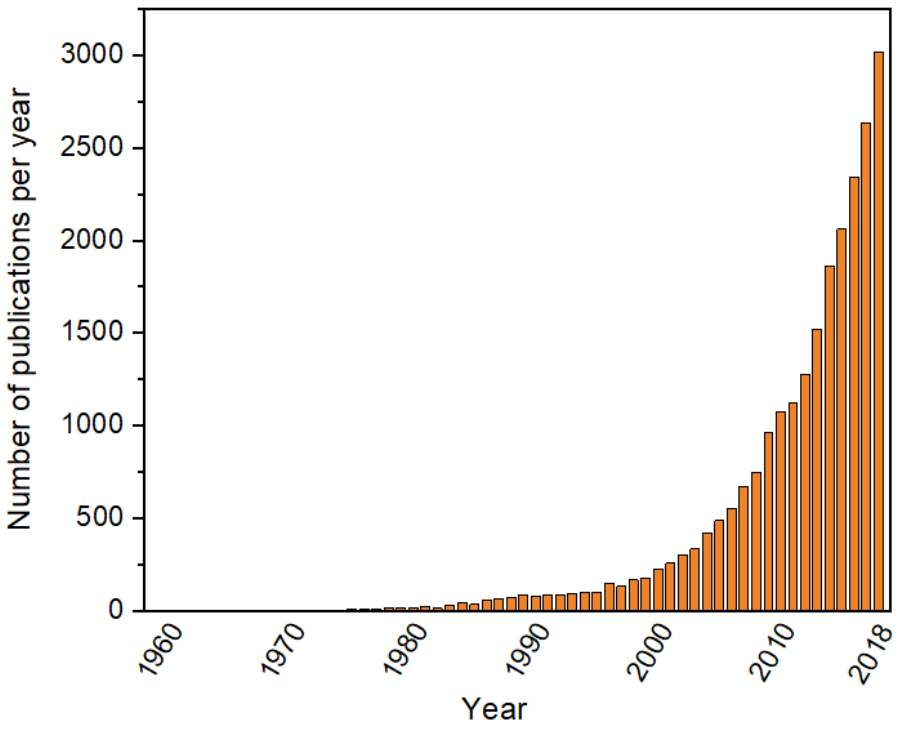


Fig. 1.1 Histogram showing the exponential increase in publications per year related to hydrogels on *pubmed* since 1960 up until 2018.

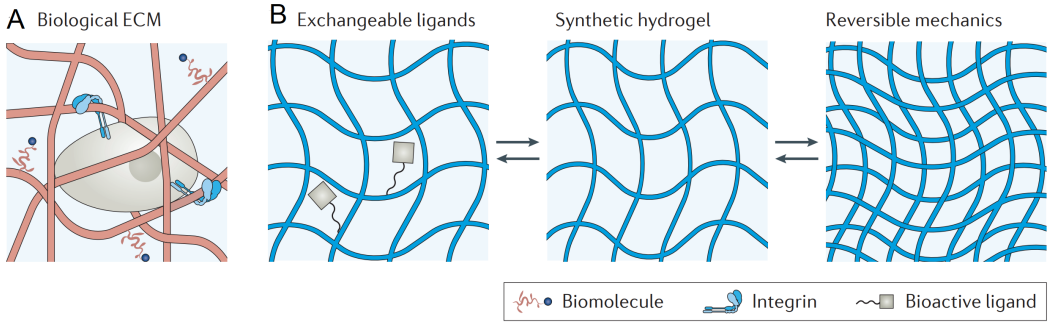


Fig. 1.2 Biological extracellular matrix and synthetic hydrogels involving reversible chemistries. A) The native extracellular matrix (ECM) is a heterogeneous fibrillar network that provides biochemical and physical cues to cells. B) Synthetic hydrogels are traditionally static, polymeric networks (middle panel). Dynamic hydrogels can capture aspects of the native ECM by temporally controlling ligand presentation (left panel) or reversibly cycling through changes in mechanics (right panel). Although these dynamic chemistries do not fully capture the complexity of the biological environment, they provide an enhanced precision over matrix cues in vitro, which will have a powerful impact on tissue engineering and regenerative medicine. Figure adapted from Rosales *et al.* [7].

Hydrogels are crucial for tissue engineering because they represent the most popular model to mimic the extracellular matrix (ECM), the supporting network surrounding cells within tissue. The ECM consists of complex interactions between macromolecules such as polysaccharides, proteins and DNA as well as a high amount of water. Hence, the ECM can be regarded as a highly complex and dynamic hydrogel that provides signalling and regulatory functions in tissues on top of structural support. Figure 1.2, adapted from Rosales *et al.* [7], shows schematically a biological ECM in comparison to a synthetic hydrogel. The figure points out approaches for introducing complexity and dynamic to improve hydrogel systems as artificial ECMs for application in regenerative medicine.

1.2 Materials used for hydrogels

Hydrogels used for biomedical applications can be produced from a variety of materials that can be classified into two main categories depending on the origin of the precursors that form the hydrogel. These precursors can be either naturally derived such as gelatin, alginate and silk or based on synthetic polymers, for example polyvinyl alcohol (PVA), poly(2-hydroxyethyl methacrylate) (polyHEMA) and poly(ethylene glycol) diacrylate (PEGDA). Both classes of material have advantages and disadvantages and it can be beneficial for some applications to use hybrid hydrogels composed of a mixture of natural and synthetic polymers.

1.2.1 Synthetic polymers

Synthetic polymers often have the advantage that their chemistry and properties are reproducible and can be easily controlled. The first clinical application of contact lenses for example used polyHEMA (Figure 1.3A) based hydrogels that provided the required mechanical properties and transparency alongside with good biocompatibilty [8]. Poly(ethylene glycol) (PEG) is amongst the most popular synthetic polymers for tissue engineering scaffolds [9] (Figure 1.3B). PEG is usually modified with acrylate- or methacrylate- groups that can be crosslinked in the presence of a suitable photoinitiator using UV light, called photopolymerization. Photopolymerization is a very efficient and precise technique which makes these materials popular for tissue engineering applications. The lack of biochemical cues for cells could be overcome by modifying synthetic polymers with bioactive molecules, e.g. short amino sequences (RGD sequence) that often serve as protein recognition sites or mixing them with biopolymers that naturally carry necessary cues [10][11].

Potential cytotoxic effects, in particular stemming from the monomers, have to be considered when using synthetic polymers for biological applications. A lot of literature can be found examining the effects of acrylate monomers on living organisms. It has

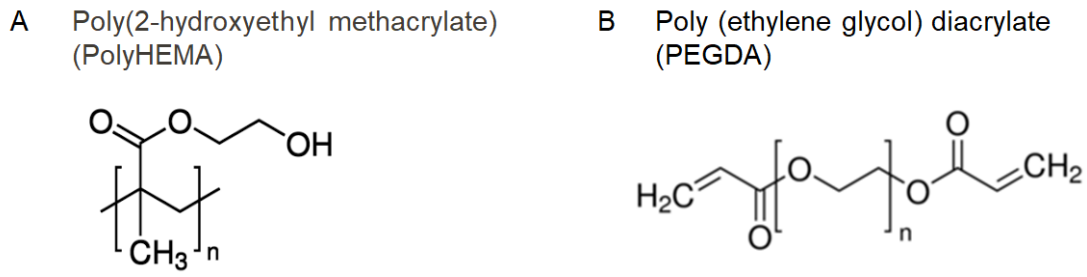


Fig. 1.3 Chemical structures of widely used synthetic polymers for biomedical applications.

been reported that short acrylates such as methyl acrylate are cytotoxic at high concentrations [12]. This is particularly challenging for cell encapsulation since there is a high concentration of non-polymerised acrylates present in solution. Synthetic polymers should therefore be polymerised and thoroughly washed prior to cell experiments to minimize toxic effects.

1.2.2 Biopolymers

Natural biopolymers are often advantageous for biological applications such as tissue engineering because they are either polymers that are components or structurally related to macromolecules of the biological ECM. Hence, they are often biocompatible and often feature recognition sites for cells. Figure 1.4 summarizes a variety of the most commonly used biopolymers and the organisms they are derived from. Alginate and chitosan for example are derived from algae and crustacean, respectively and can be extracted in abundance. Silk is being sourced from silkworms and ECM components as collagen, elastin and fibrin are typically sourced from mammals. Due to their origin, biopolymers often already feature relevant properties and recognition sites that are required to support living cells. Much like synthetic polymers can be modified, e.g. to feature biological cues, biopolymers are often modified to optimize mechanical properties and enable additional crosslinking mechanisms such as photo-polymerization by introducing photo-active functional groups.

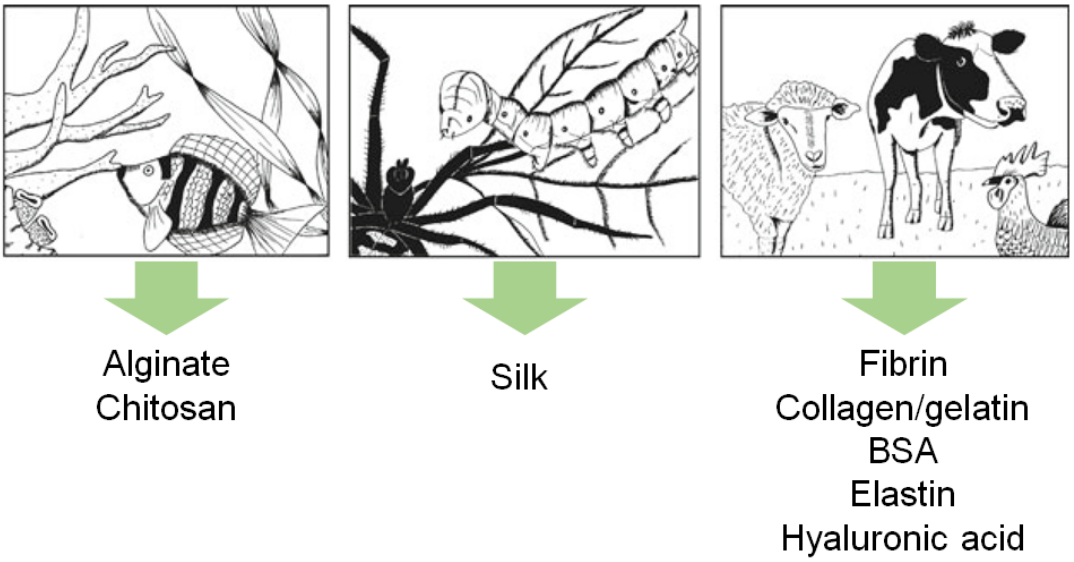


Fig. 1.4 Overview of most common biopolymers for biomedical applications that are derived from a diverse variety of organisms including marine organisms, insects, birds and mammals. Figure adapted from Monzack *et al.* [13].

Figure 1.5 shows the number of publications of the most popular biopolymers for hydrogels according to a pubmed query reflecting their importance in regenerative medicine. Most publications used collagen which represents a dominant part of the ECM of connective tissues (bone, cartilage, tendon, cornea, blood vessels, and skin). It plays a major role in maintaining biological and structural integrity of cells and is highly dynamic [14]. Collagen is primarily a polypeptide that forms secondary structures of triple-helices that combine to elongated fibrils (Figure 1.6A). Scaffold structures comprised of collagen are often fabricated using freeze-drying or photo-polymerization techniques [15].

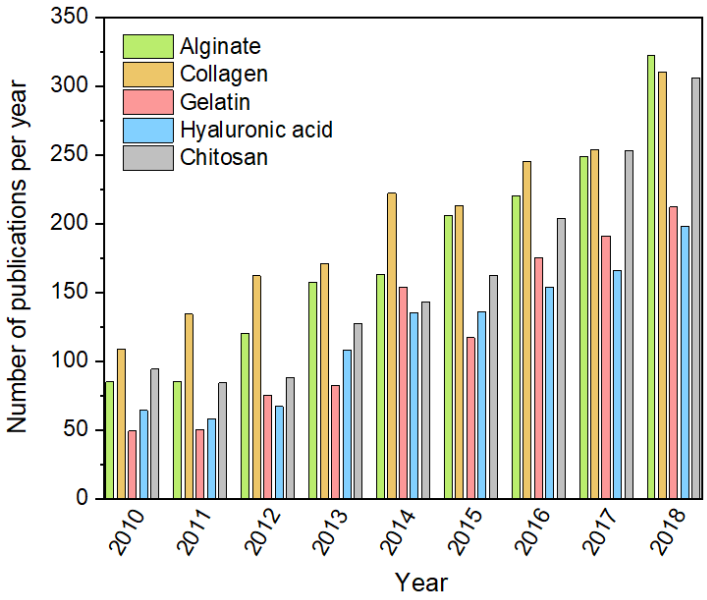


Fig. 1.5 Pubmed queries for hydrogels based on the most commonly used biopolymers: Alginate, Collagen, Gelatin, Hyaluronic acid and Chitosan.

Gelatin is derived from collagen and can be obtained by hydrolytic degradation of collagen, illustrated in Figure 1.6B. Gelatin dispersed in water forms physical gels below a certain gelation temperature that is usually about 30°C depending on the concentration and composition of the gelatin solution [17]. In order to form hydrogels that are stable at an average mammalian body temperature (∼37°C), gelatin is often modified to facilitate a stable crosslinking mechanism to form a polymeric network. A methacrylamide-modified gelatin (GelMA) for example, is widely used to enable photo-crosslinking of gelatin [18][19]. Gelatin represents a good material for tissue engineering applications due to its favourable mechanical properties and cell recognition sites that promote the attachment and proliferation of cells [20][21].

Chitosan has become one of the most prevalent biopolymers used for hydrogels after collagen and alginate which is reflected in the research interest in Figure 1.5. It is being used for a wide range of applications such as for pesticides in agriculture, as food additives as well as in regenerative medicine and tissue engineering. Chitosan is a cationic polysaccharide that is derived from the chitin in shells of crustacea (e.g. crabs and

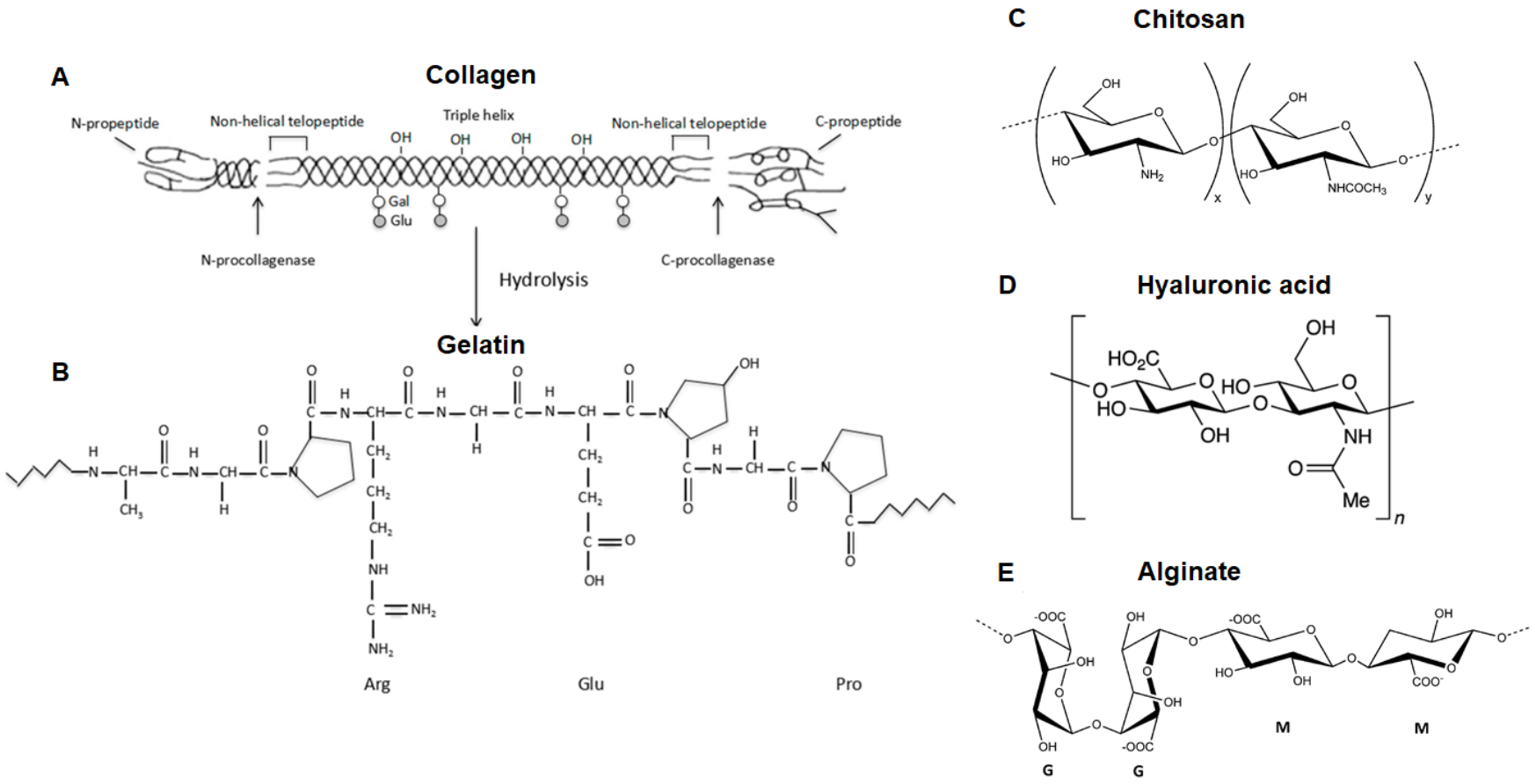


Fig. 1.6 Chemical structures of most commonly used biopolymers for hydrogels. A) Gelatin that is derived from collagen, B) Hyaluronic acid, C) Alginate, and D) Chitosan [16][13].

shrimps) by partially deacetylating chitin (Figure 1.6C) [13]. In a basic environment, chitosan solutions can be gelated at temperatures above 37°C which enables stable chitosan hydrogels at mammalian body temperatures without any modifications [22].
Hyualoronic acid (HA) is a polysaccharide composed of alternating units of D-guloronic acid and D-N-acetylglucosamine (Figure 1.6D), and represents an important component of cartilage and skin tissue [23]. A wide variety of HA modifications has been reported in the literature, including various different crosslinking mechanisms [24]. For example, thiol-modified HA crosslink spontaneously in air [25]. A wide-spread strategy of crosslinking HA is based on introducing photo-active groups similarly to gelatin described above [26][25].
According to the pubmed summary (Figure 1.5), alginate is the most predominant biopolymer next to collagen that is applied for hydrogels. The anionic polysaccharide alginate, mainly derived from brown seaweed, stands out from other biopolymers for its ionic gelation. The ionic crosslinking in the presence of divalent cations (e.g. Ca^{2+}, Ba^{2+}) is favourable for biomedical use because it allows the formation of hydrogels at mild pH and temperature conditions and is reversible [27]. Alginate is structurally similar to hyaluronic acid and chitosan since it is also composed of two alternating sugars namely α-L-guluronic acid and β-D-mannuronic acid (Figure 1.6E) [28]. Numerous modifications of alginate were reported, e.g. a recent combinatorial approach, by Vegas *et al.*, to identify variants of alginate that reduce the immune response of alginate hydrogels when implanted into rodents [29]. Additional crosslinking mechanisms can be introduced through functional groups. Jeon and co-workers for example, demonstrated photo-crosslinking of degradable alginate hydrogels by modifying the alginate molecules with methacrylate groups [30].
The ability to mimic not just chemical characteristics of an artificial cell environment but precisely control the surrounding on the scale of single cells, allows to study the effect of microscopic features and can ultimately be exploited to spatially control cells in three dimensions. For example, to regulate the initial attachment of cells, thereby

improving cell seeding or fabricate cell repellent surfaces with micron- to nano sized topographies.

A lot of effort has been invested into advancing microfabrication methods of hydrogels [31]. Microfabrication of hydrogels encompasses simple emulsification for industrial applications as well as complex microfluidic tools that can offer spatial control over concentration gradients [31]. In the following chapters, the focus lies on Additive Manufacturing (AM) techniques that are being applied to micro-fabricate hydrogels including the state of the art photolithography technique, namely two-photon polymerization (2PP).

1.3 Additive manufacturing of hydrogels

1.3.1 Bioprinter systems

Today's achievements in Additive Manufacturing (AM), also referred to as 3D printing or Rapid Prototyping (RP), date back until the early 1980's to C. W. Hull's work on designing plastic materials based on photopolymers [32]. In 1986, Hull patented an apparatus for the production of three-dimensional objects by photolithograph [33], which was followed by several other patents advancing the technology of 3D printing. He created the STL (Standard Tesselation language or STereo Lithography) file format that has been the established format until the present time, coupling the design of 3D structures using computer aided design (CAD) softwares and the 3D printing process [32]. Most recently, 3D printing has been forwarded as a revolutionary technology for both major industries and the medical sector including applications in hospitals and research. The major AM methods used for biomedical applications that are suitable for hydrogels are photolithography, inkjet printing and extrusion printers that are discussed in more detail in the following chapters [34]. Table 1.1 summarises the key characteristics of these AM methods to fabricate hydrogel structures for applications in cell culture.

Table 1.1 Comparison of Additive Manufacturing methods used for biomedical applications that are suitable for hydrogels.

	Bioprinter Systems		Photolithography	
	Inkjet Printer	**Extrusion Printer**	**UV Polymerization**	**2-photon Polymerization**
Resolution	≥ 50 µm	≥ 100 µm	1 – 30 µm	≥ 100 nm
Advantages	• Cost-effective • Wide range of material choice	• Fast and inexpensive • No toxic binder or photoinitiator required • Structures with multiple materials possible	• Fast ad cost-effective • Good mechanical strength • Large structures possible	• High resolution below the diffraction limit of light • Allows printing within photoresist -> enables cell encapsulation
Drawbacks	• Toxic liquid binding materials needed • Often lack of transparency for microscopy	• High temperatures required • Low mechanical strength • Smooth surfaces	• UV irradiation damages living cells • Toxic photo-initiators • Scaffold shrinkage due to water evaporation	• Expensive set-up • Long fabrication times for high resolution structures • Toxic photoinitiator

1.3.1.1 Inkjet printer

Commonly, inkjet printer are used for printing inks on paper. However, since 2001 inkjet printing has evolved for printing 3D structures using water-soluble and conductive polymers, ceramic, metal proteins and nucleic acids [36][37]. An important feature in 3D inkjet printing is the dispensing and precise positioning of very small volumes of fluid (1–100 picoliters) on a substrate before transformation to a solid. It is mainly a powder-based method, where a thin layer of powder is cast onto a movable stage. Then a printing head prints liquid binding material onto the powder to form one layer of the object. The stage lowers by a defined distance so that the process can be repeated layer-by-layer, forming a 3D structure (Figure 1.7A). Problematic for biomedical applications, particularly in the presence of living cells, is the toxicity of many liquid binding materials [38]. Due to the lack of transparency, caused by incomplete interaction of binding liquid with powder particles, inkjet printed materials are often not suited for microscopic studies. In order to overcome this problem, there are

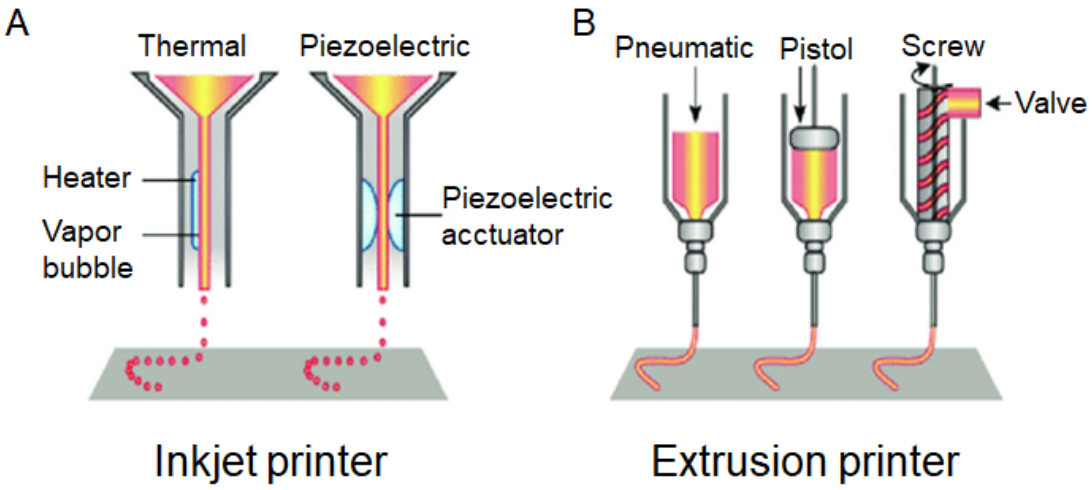


Fig. 1.7 Schematic of inkjet and extrusion based bioprinter as they are being used for the microfabrication of hydrogels. Figure is adapted from Piagesi *et al.* [35].

other approaches of inkjet-printing which are non-powder based such as polymer-based inkjet methods and natural adhesives (e.g. proteins) were successfully printed based on inkjet methods [38]. Using simultaneous ink-jetting of multiple cell types, Xu *et al.* developed a method to fabricate complex and heterogeneous three-dimensional tissue constructs [39]. The biological functions of the 3D printed constructs were evaluated in vitro and in vivo and the bioprinted constructs were able to survive and mature into functional tissues with adequate vascularization in vivo. This approach however, is very complex, time-consuming and requires extensive individual optimisation to adjust to different experimental conditions.

Most recently, resolutions down to 50 μm could be achieved for multi-component hydrogels using an inkjet printer [40]. This work was based on a series of very rapid bio-orthogonal Michael type addition reactions during the fusion of bio-ink droplets before reaching the target substrate [40].

1.3.1.2 Extrusion printer

The main representative for extrusion based systems is fused deposition modelling (FDM), which is a heat-based manufacturing technology and the most widely used 3D

printing method due to its relatively simple mechanism and cost-effectiveness. In this method, a plastic filament for example, is directed into a heating block where it is heated to a semi-molten state, which can be printed onto an adjustable stage for a layer-by-layer fabrication (Figure 1.7B). Accordingly, a 3D scaffold can be deposited layer-by-layer as molten polymers are extruded through a nozzle, merging with the biomaterial that was deposited in the previous layer. Korpela *et al.* investigated biodegradable porous scaffold structures using different materials and determined fibroblast cell response of the structures [41]. Many biological processes however are vulnerable to high temperatures needed for the melt process. To overcome this limitation, various dissolution processes that surrender high temperatures have been tested to produce hydrogels [34]. For example, Liu *et al.* used a multi-nozzle low-temperature deposition method to fabricate scaffolds with heterogeneous materials and gradient hierarchical porous structures [42]. By means of a syringe-based volume-driven injecting (VDI) nozzle, they demonstrated the extrusion of the synthetic polymer poly (lactic-co-glycolic acid) (PLGA) combined with the biopolymers collagen, gelatin and chitosan to form a hierarchical porous scaffold. Such a scaffold with biological gradient properties could potentially be used in the reconstruction of multi-tissue organs (e.g. liver, kidneys). The primary advantage of extrusion based systems is cost-effectiveness, while compared to photolithography and inkjet printing there is no need of a photoinitiator or binding liquids which can be toxic for living organisms. Particularly interesting for tissue engineering is the ability to produce structures comprising many materials. Drawbacks of these systems on the other hand, are limited resolution (typically above 100 μm), low mechanical strength and smooth surfaces which hinders cell adhesion [34].

1.3.2 Photolithography

As the first AM technique, photolithography remains one of the most powerful and versatile methods due to its efficiency, high fabrication accuracy and the increasing

number of materials that can be processed [43]. The manufacturing of 3D objects by photolithography is based on the spatially controlled photo-polymerization of a liquid resin. For a common negative-tone photoresist, these regions become insoluble whereas the unexposed regions can be removed in a development step. The most popular strategy for photolithography is based on radical photo-polymerization [44]. Commonly, photoresists (light sensitive materials) consist of radical initiators based on aromatic ketones and monomers with vinyl groups such as (meth)acrylates [45]. Upon the absorption of photons, the photoinitiator becomes a radical which initiates the polymerization reaction. The basic installation of a photolithography set-up, shown in

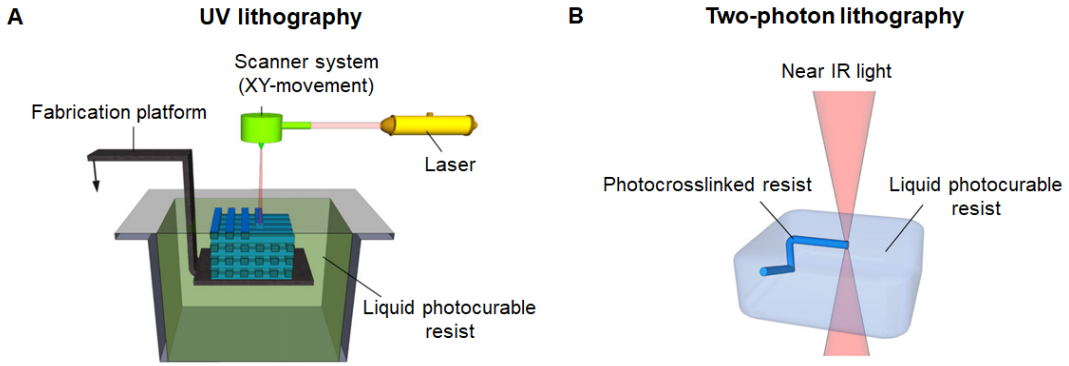


Fig. 1.8 Simplified schematic of A) a UV lithography set-up compared to B) a two-photon lithography set-up, Figure adapted from Billiet *et al.* [34].

Figure 1.8A, consists of a movable stage, a tank of liquid photo-polymerizable resin, a laser source (commonly UV light) and a computer interface. An alternative set-up contains an additional mask in the form of a digital mirror device (DMD), facilitating the fabrication of a whole layer at once. The build-up of a 3D construct is enabled by a layer-by-layer fabrication. After the photo-polymerization of the first layer that produces individual 2D patterns of polymerized material, the platform is moved to polymerize a pattern in a second layer [43].

1.3.3 Two-photon lithography

The state of the art photolithography technique is two-photon polymerization (2PP) which can achieve feature sizes below the diffraction limit of visible light (down to 100 nm) [46]. Contrary to one-photon absorption (1PA) in conventional photo-polymerization, two-photon absorption (2PA) is a non-linear process and allows for free form fabrication because of its capability of direct exposure of the internal volume, whereas conventional one-photon lithography is based on its planar nature [47] (Figure 1.8B). Due to the nature of 2PA discussed in the following chapter, polymerization only occurs at the focal point of a powerful laser facilitating the highest resolution possible.

1.3.3.1 Two-photon absorption

The German theoretical physicist Maria Göppert-Mayer, portrayed in Figure 1.9, predicted two-photon absorption (2PA) in her dissertation in 1931 [48]. Maria is one of only two women to have won the Nobel Prize in physics for her discoveries concerning nuclear shell structure alongside E. P. Wigner and H. D. Jensen in 1963. Her correct mathematical prediction of 2PA could only be proven experimentally with the invention of the laser in 1961 by Kaiser and Garrett. This is because the light intensities required for 2PA are too high to be achieved with incoherent light which is emphasized with the following exemplification: In bright daylight, a molecule of rhodamine B, an excellent 1- or 2- photon absorber, absorbs a photon through a 1-photon process about once a second, a photon pair by 2-photon absorption every 10 million years; no 3-photon absorption is expected throughout the entire age of the universe [49]. Figure 1.10A demonstrates the localised nature of 2PA at the focal point of the laser versus 1PA occurring throughout the entire laser path. The photograph shows the excitation of fluorophores in solution for 1PA in comparison to 2PA.

Göppert-Mayer showed the theoretical possibility of two photons interacting in such a



Fig. 1.9 Portrait of Maria Göppert-Mayer. German physicist who mathematically predicted two-photon absorption in her dissertation, 1931. She is one of only two women to have won the Nobel Prize in physics for her discoveries concerning nuclear shell structure alongside E. P. Wigner and H. D. Jensen in 1963.

way that their combined energies can take an atom or molecule from the initial state to its excited state, illustrated in Figure 1.10B. For example, two photons at a certain wavelength could cause the same effect as a single photon with half its wavelength. 2PA of a molecule is expressed in the unit Göppert-Mayer (GM 10^{-50} cm^4 photon^{-1}) which describes the product of the two areas available (cm^4) for each photon to arrive at almost the same time (s) per photon and a scaling factor (10^{-50}) to simplify the values for conventional dyes. The critical limitation is that the absorption of the second photon has to occur very quickly (typically within 10^{-15} seconds = femtoseconds) after the first photon. The high intensities required for 2PA could only be realised with ultrafast pulsed mode locked laser such as a titanium sapphire laser. Although the peak intensities of ultrafast pulses can be quite high, ultrashort duty cycles enable high squared light intensities at low average powers, which reduces potential material damages. Winfried Denk and co-workers were the first to exploit the special features of 2PA for two-photon excitation microscopy which allows highly localised fluorophor excitation within a material without most background noise [50].

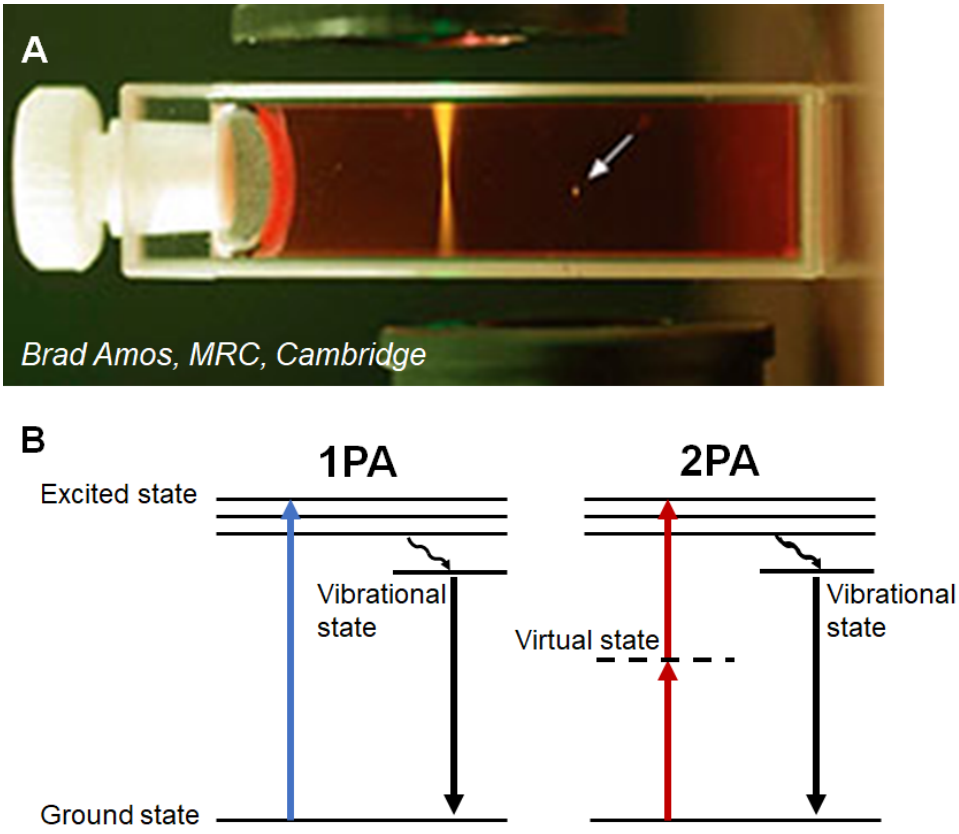


Fig. 1.10 One-photon absorption (1PA) versus two photon absorption (2PA). A) Photograph showing the excitation of fluorophores in solution via 1PA in comparison to 2PA. 1PA occurs throughout the entire laser beam with decreasing intensity further away from the focal point of the laser. 2PA only occurs at the focal point of the laser where the intensity is high enough for 2 photons being absorbed almost simultaneously. B) Simplified Jablonski diagram demonstrating 1PA vs 2PA.

1.3.3.2 Two-photon polymerization

In 1997, Maruo and co-workers introduced the free form fabrication of 3D structures with feature sizes down to 7 μm based on 2PA using an ultrafast pulsed infrared laser [51].

2PA based photo-polymerization was achieved applying laser peak powers of 20 mW within a photoresist consisting of photoinitiators, urethane acrylate monomers and urethane acrylate oligomer (Figure 1.11). This truly 3D approach of fabricating within a photoresist, as opposed to a layer-by layer fashion, takes advantage of the fact that the 2PA probability depends quadratically on the light intensity so that the intensity is only high enough in the focal point of a tightly focussed laser. The subsequent photoinduced chemical reaction is then also localized in this small volume allowing sub-micron resolution.

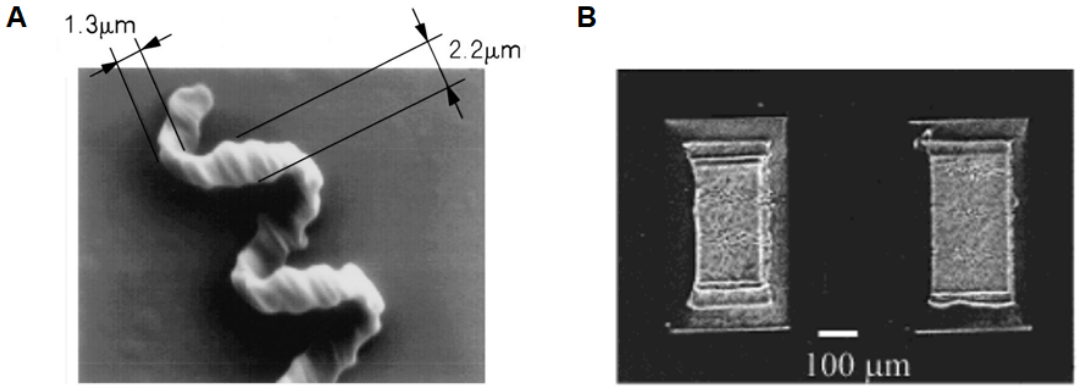


Fig. 1.11 Scanning electron micrograph of A) the very first 2PP microstructures fabricated using a photoresist consisting of urethane acrylate monomers and oligomers in combination with photoinitiators [51]; B) the first 2PP hydrogel microstructures using a water-based photoresist consisting of BSA with the dye rose bengal as the photoinitiator [52].

Since Maruo's first demonstration of 2PP based on radical photo-polymerization, it remains the most popular strategy for 2PP to date [44]. Commonly, photoresists (light sensitive materials) for 2PP consist of radical initiators based on aromatic ketones and monomers with vinyl groups such as (meth)acrylates [45]. Upon the absorption

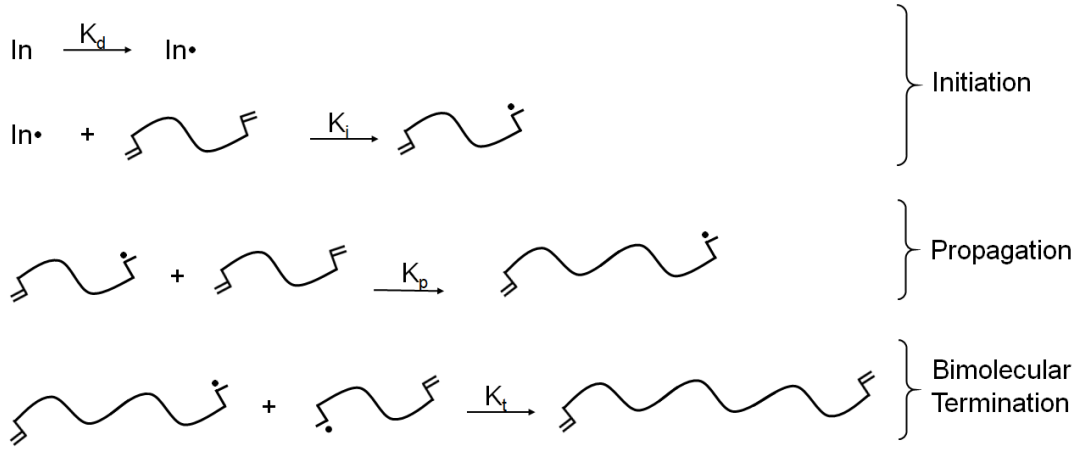


Fig. 1.12 Schematic of photo-polymerization by free radical chain polymerization of a multiple double-bond containing monomer. A typical free radical chain reaction can be classified into initiation, propagation and termination. k_d is initiator decomposition rate constant; k_i is initiation rate coefficient; k_p is propagation rate coefficient; and k_t is bimolecular termination rate coefficients, respectively.

of photons, the photoinitiator becomes a radical which reacts with the vinyl groups of the polymers featuring (meth)acrylate groups in the initiation step (Figure 1.12). During the propagation step the growth of the polymer chain occurs by addition of the monomer molecules to the radical center [53]. The growth of the polymer chain is stopped in the termination reaction, in which radical centres are eliminated from further reaction. The bimolecular termination, depicted in Figure 1.12, is usually the dominating termination reaction where two macro-radicals react with each other [53]. The fast and efficient nature of this type of reaction makes meth(acrylates) more popular than ionically polymerized monomers such as epoxides [45]. There are many mono- and multifunctional (meth)acrylates commercially available that readily photo-polymerize facilitating a large variety of photoresists.

For biomedical applications however, it is critical that photoresists are biocompatible, feature specific recognition sites for enzymes (e.g. RGD sequence) and degrade *in vivo* without any toxic side products [54][34]. Suitable candidates are often polymers derived from living organisms, referred to as biopolymers (e.g. proteins, DNA and polysaccharides). In regenerative medicine, several biopolymers are utilized to produce

hydrogels whose properties can be tailored to match the desired application [54]. For example, proteins like collagen isolated from the extracellular matrix (ECM) as well as polysaccharides assembled by living organisms are extensively used to fabricate hydrogel scaffolds in tissue engineering [15].

A number of factors affect the efficiency with which two-photon excitation can initiate polymerization. A critical factor is the 2PA cross-section δ_{2PA} of an initiator which quantifies the ability of a molecule to absorb two photons in one quantum event [55]. This can be best demonstrated looking at the 2PA cross-section unit in GM. 1 GM is equal to 10^{-50}·cm^4 ·s·photon^{-1} which describes the square of the area of two photons in cm within the time the two photons have to interact in order to excite a molecule in one event. The 2PA cross-section can be increased by several orders of magnitude by optimising the molecular design of photoinitiators compared to typically very low 2PA cross-sections of Ultraviolet initiators. Hence, the production of photoinitiators with high 2PA cross-sections is often the preferred route to reduce the laser power required for fabrication [56]. Other factors are for example the quantum efficiency for the creation of radicals, meaning the number of absorbed photons that cause the formation of radicals. The quantum efficiency QE is here described as the ratio of the number of radicals formed to the 2PA cross-section δ_{2PA} [57]:

$$QE = \frac{Radicals\ formed}{\delta_{2PA}} \tag{1.1}$$

Lastly, the initiation velocity of the formed radicals is crucial to the overall photoinitiation process because they represent the degree of reactivity of the radicals that are created.

Cumpston and co-workers advanced the efficiency of 2PP by synthesising photoinitiators with high 2PA cross-sections relative to conventional photolithography initiators using UV light [56]. They showed that molecules featuring the general structural motifs D-π-π-D, D-π-A-π-D and A-π-D-π-A (where π is a p conjugated bridge, D is a donor,

and A is an acceptor) have large δ relative to the parent unsubstituted conjugated molecules [58].

Optimization of 2PP efficiency requires an understanding of the polymerization kinetics, which is challenging to directly probe due to microscopic reaction volumes and fast reaction times. A common strategy is to apply knowledge of macroscopic polymerization kinetics based on conventional UV polymerization. Some properties that are difficult to study on microstructures, such as viscoelastic properties, are often determined for UV polymerized samples instead. While these results can help to gain relative information about interdependencies, they are not suitable to compare the polymerization kinetics due to the very different nature of 2PP [59][60][61][62]. The crosslinking density is dependent on the polymerization kinetics. UV polymerization and 2PP differ substantially in the reaction volume, UV polymerization is occurring throughout the entire volume of the irradiation whereas 2PP only occurs very localized at the focal point of the laser. This has to be taken into account considering oxygen quenching, diffusion dependent reaction steps of the polymerization and the amount of reactive molecules present in a very small volume which will all be affected examining such different reaction volumes.

1.3.4 Two-photon polymerization of hydrogels

This introduction focuses on the 2PP of hydrogels meaning using photoresists that consist of a monomer diluted in water mixed with a water-soluble photoinitiator as opposed to most commonly applied photoresists consisting of almost 100%, typically hydrophobic, monomers mixed with a photoinitiator.

Water-based photoresists are crucial for many biomedical applications because they are coming close to physiological and chemical requirements of living tissue with mechanical properties that are similar to the extracellular matrix (ECM) as discussed in chapter 1.1. Two-photon fabricated hydrogels are often permeable to biological solutes such as sugars, DNA and signal molecules produced by living cells as shown for BSA

based hydrogel microstructures [52][63]. In particular, this work is looking at biologically derived monomers for 2PP of hydrogels which are often favourable to mimic the natural cell environment because they are chemically the same or closely related to polymers surrounding living tissue. Common polymers as well as biological tissue show negligible linear absorption in the near-Infrared (NIR) range [64][65], allowing the laser to penetrate the photoresist as well as living cells without damaging them. The transparency of tissue to NIR light enables the microfabrication in the presence of living cells. Water-based photoresists for 2PP however, can be challenging to process. The monomers are typically highly diluted in water which affects the quantum efficiency and reactivity of the photoresist. Structures are often restricted to height due too low mechanical stability and vulnerable to swelling and deformation after the development. Additionally, water-soluble and biocompatible photoinitiators are limited and require further development.

In 2000, Pitts and co-workers showed 2PP of hydrogels for the first time using the protein bovine serum albumin (BSA) and rose bengal (RB) as the photoinitiator [52] (Figure 1.11B). They investigated the efficiency of photo-activated crosslinking in relation to the RB concentration and suggested that the protein crosslinking is due to a direct hydrogen transfer between an amino acid residue of the protein and the dye molecule itself. They also showed that BSA microstructures could be used for sustained release of bioactive molecules (e.g. polysaccharide) which could for example, be exploited for applications in drug delivery [52]. Up to date, the most frequently used biopolymers for 2PP of hydrogels are BSA and methacrylated gelatin [66][65][67], because they are cheap, easy to process and showed very good mechanical properties in comparison with other natural polymers so far tested for 2PP.

1.3.4.1 Water-soluble photoinitiators for 2PP of hydrogels

Since the first introduction of 2PP, much effort was put into the development of improved 2PA photoinitiators (2PI's) but most initiators are typically not soluble in water and toxic for living cells. The development of biocompatible and simultaneously highly efficient water-soluble initiators is crucial to make 2PP of hydrogels practical for biomedical applications. Figure 1.13 shows the chemical structures of the latest advancements in water-soluble photoinitiators for 2PP that feature low cell toxicities. Li and co-workers for example, synthesized a series of cyclic benzylidene ketone-based two-photon initiators containing acid sodium salts to improve water solubility (Figure 1.13A). They then tested the toxicity for the series of PI's with two different cell types. The cyclopentanone based initiator, called P2CK, yielded the highest cytocompatibility, compared to the widely used UV initiator Irgacure 2959, and featured a higher 2PA cross section (δ = 176 GM in water) [68]. Building on advancing the biocompatibility of 2PI's, Tromayer and co-workers tested an approach of reducing the cytotoxicity of a photoinitiator by attaching a polymeric hyaluronan backbone to the photoactive part of the molecule (Figure 1.13B) in order to prevent the migration of the initiator from the extracellular matrix into the cytosol [69]. More recently, Tromayer *et al.* demonstrated the first cleavable diazosulfonate (DAS) 2PI shown in Figure 1.13C. Double the concentrations of DAS are used compared to P2CK to overcome the lower 2PA cross-section. However, they showed that cell survival of cells within 3D microstructures was up to 5 times higher using DAS compared to P2CK [70]. In 2019, Zheng *et al.* published a novel water-soluble photoinitiator with a significantly higher 2PA-cross-section (Figure 1.13D) compared to the 2PI's discussed above (δ_{2PA} = 2999 GM in water) [71]. Low cytotoxicity was shown for Hela cells growing on microfabricated hydrogel structures for 48 hours demonstrating the potential for cell applications [71].

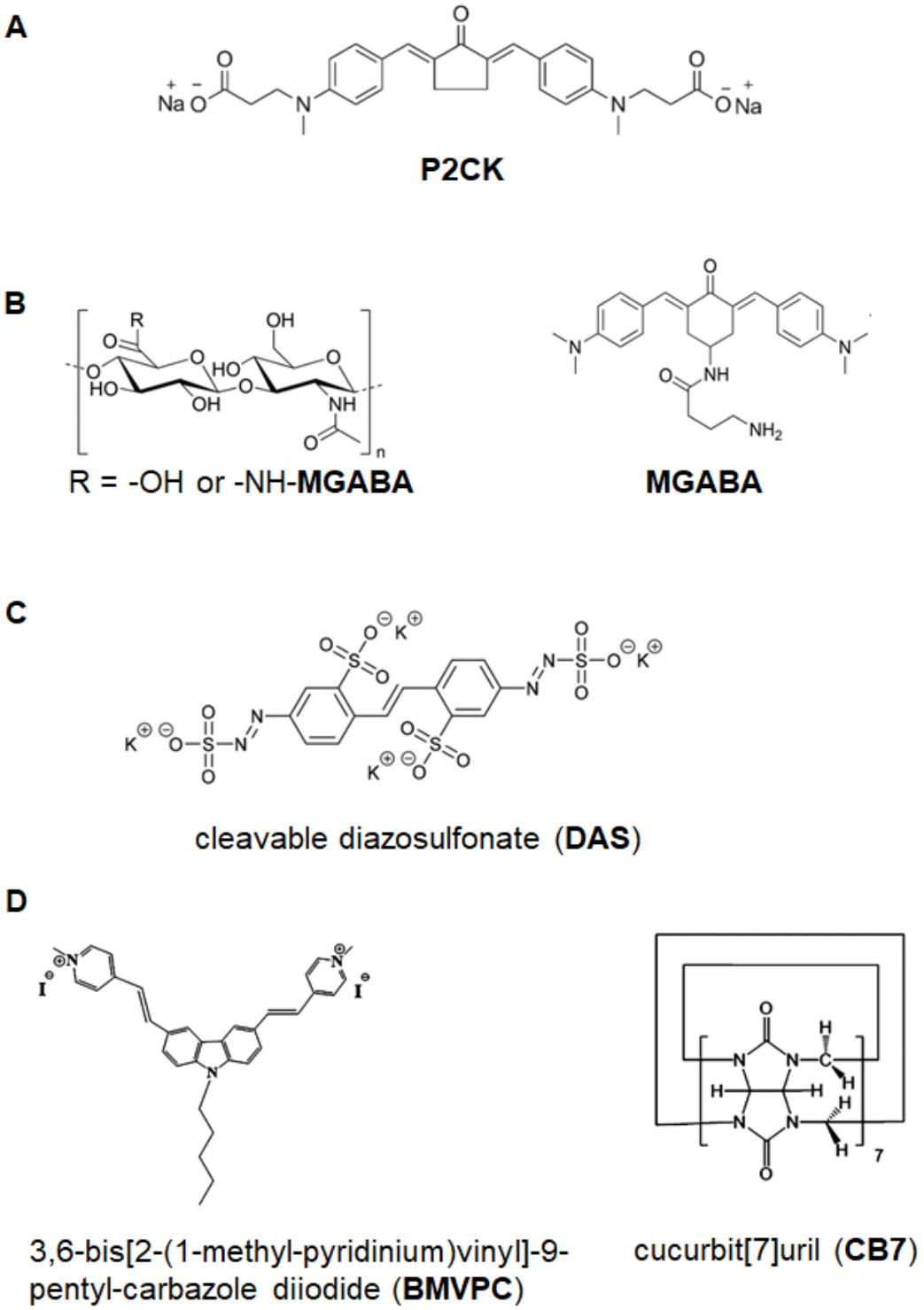


Fig. 1.13 Chemical structures of latest advancements in water-soluble photoinitiators for 2PP with low cell toxicities [68][69][70][71].

1.3.4.2 Synthetic polymers for 2PP of hydrogels

Only few synthetic polymers have been reported for 2PP of hydrogels. Poly (ethylene glycol) (PEG) is usually the key component of photoresists that are based on synthetic polymers. PEG has the advantage of being FDA approved and is widely used for applications in tissue engineering [72]. Synthetic hydrophilic polymers such as PEG diacrylate (PEGDA) on its own or as part of copolymers were demonstrated to be well suitable for 2PP photoresists. In combination with suitable 2PP initiators, PEGDA showed good 2PP characteristics facilitating the fabrication of 3D microstructures [73] when diluted in 50% water in order to obtain hydrogels [68][74].

Considering the major factors determining 2PP discussed in section 1.3.3.2, photoresists composed of synthetic polymers with more than one functional group per molecule, often exhibit higher quantum efficiencies than biopolymer based photoresists. The multifunctionality facilitates a chain reaction initiated by a radical formed upon 2PA. That radical attacks the functional group of a molecule which becomes a radical itself, and can react again with another molecule creating a new radical. This reaction can continue numerous times in form of a chain reaction, much like a domino effect, resulting in a high quantum efficiency. As defined in equation 1.1, the quantum efficiency increases with more radicals formed divided by the 2PA cross-section. A radical chain reaction efficiently produces many radicals through one starter radical (see chapter 3.1). Synthetic polymers have the advantage that their chemistry and properties are reproducible and hence, can be easily controlled. They are typically smaller than most biopolymers. PEGDA with molecular weights (MW) between 200 Da and 1000 Da were applied for 2PP which is comparably small to a single BSA molecule (MW $\approx$ 65.5 kDa [75][72]. In the following, varying approaches of using synthetic polymers for 2PP of hydrogels will be discussed.

Jahveri *et al.* for example, have fabricated hydrogels composed of 2-hydroxyethyl methacrylate (HEMA) and PEGDA in aqueous medium by using hydrophobic chro-

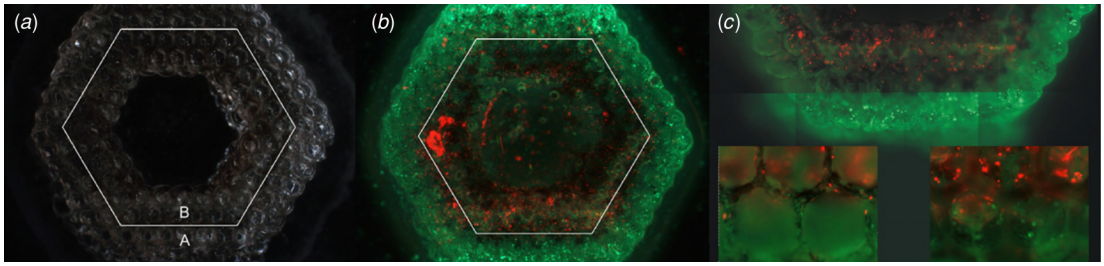


Fig. 1.14 Scaffold seeded with cells by means of laser-induced forward transfer (LIFT): a) Dark field image. The white hexagon indicates the border between the two scaffold areas seeded with vSMCs derived from adipose tissue and ovine endothelial cells (ECs), respectively; b) Fluorescence image indicating the location of different cell types after the LIFT procedure; c) Detailed image of the border area. The insets demonstrate that a sharp transition from vSMCs (red) to EC-seeded (green) regions is present along the entire thickness of the scaffold. Figure adapted from Ovsianikov *et al.* [75].

mophores with large 2PA cross-sections. To improve the dispersion and effectiveness of the chromophore in water an additional surfactant was used. Although, Jahveri and co-workers suggested this set-up for biological applications, they did not test for cytotoxicity [74]. Several new water-soluble photoinitiators with high 2PA cross-sections have been developed after this work, making the approach of using a hydrophobic chromophore for its high cross-section unnecessarily intricate.

Ovsianikov and co-workers demonstrated cell seeding into 2PP scaffold structures after the fabrication and washing by using laser-induced forward transfer (LIFT). This approach allowed to embed two different cell types in a controlled fashion, thereby avoiding toxic effects of non-polymerised PEGDA [75]. This technique is using a laser to send cells from a donor substrate to a receiver substrate upon a laser-induced shock wave. Figure 1.14 shows fluorescence images of two different cells types that were seeded into the two-photon fabricated scaffold structures. Ovsianikov *et al.* conclude that this approach could potentially be exploited to create 3D multicellular tissue constructs [75]. Tibbitt *et al.* demonstrated the suitability of PEGDA as a positive tone resist by eroding PEGDA hydrogel on the basis of 2PP in the presence of living cells [76]. Photodegradable hydrogels were formed from a photolabile PEG-based crosslinker (PEGdiPDA) and a monoacrylated PEG macromer (PEGA) mixed with

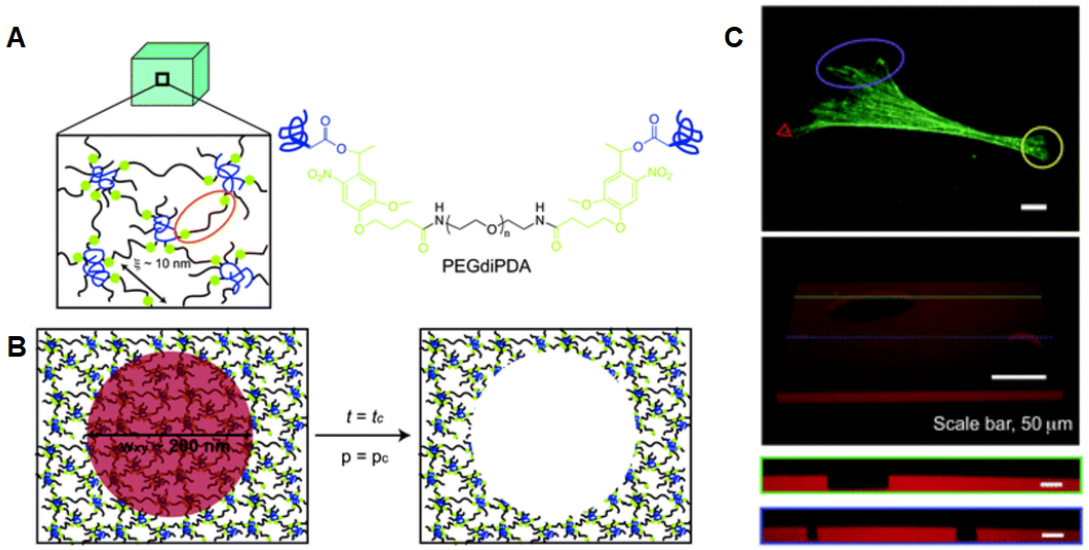


Fig. 1.15 Two-photon induced degradation and complete erosion of photodegradable hydrogels. A) PEG-based photodegradable hydrogels were formed (A, left) from PEGdiPDA (A, right) and PEGA with physically entrapped fibronectin. B) Two-photon irradiation induces complete gel erosion at the focal point (red circle). This photocleavage releases the polymer chains that comprise the hydrogel selectively from irradiated regions (B, right). C) Micronsized features were eroded via two-photon irradiation to disrupt adhesion at the anterior or posterior of adhered cells (purple oval and yellow circle) or to disrupt adhesion at individual filopodia (red triangle). To demonstrate this strategy, feature formation was performed in the absence of cells and was monitored with confocal microscopy. Figure adapted from Tibbitt *et al.* [76].

additional fibronectin to provide cell recognition sites in order to improve cell adhesion. Figure 1.15 illustrates schematically the two-photon induced degradation of photolabile PEGdiPDA crosslinks. Tibbitt and co-workers two-photon irradiated material at the cell–gel interface to remove cell adhesion sites selectively. They propose that this approach represents a useful tool to study cell adhesion and detachment to and from soft substrates which they exemplified by monitoring the cell retraction of mesenchymal stem cells after disrupting the cell - material interface through hydrogel erosion.

Overall, PEGDA is the polymer of choice for hydrogels to support living cells. PEGDA polymerizes well but is often problematic during the development process. The resulting microstructures, typically printed on glass substrates, are only loosely attached to the surface and flake off easily which makes it not suitable for cell culture. In order to avoid this problem, the glass substrates have to be pretreated with 3-(trimethoxysilyl) propyl

methacrylate (MAPTMS) to introduce a mono-layer of crosslinker groups facilitating covalent attachment of microstructures to the substrate [77]. A major disadvantage of PEG based precursors is their cytotoxicity which can be minimised by thoroughly washing 2PP hydrogels after development. 2PP in the presence of living cells however, would be toxic to the cells suggesting that biopolymer based hydrogels would be more suitable to avoid this complication [78].

1.3.4.3 Biopolymers for 2PP of hydrogels

The first hydrogel structures from natural polymers using 2PP were shown by Pitts *et al.* in 2000, using the unmodified protein bovine serum albumin (BSA) and fibrinogen (Figure 1.11B) [52]. They interrogated the efficiency of protein polymerization as the function of photoinitiator concentration and applied the optimized fabrication parameters then to entrap compounds within the microstructures during fabrication that can be released in a sustained fashion [52]. Pitts and co-workers used scanning electron microscopy (SEM) images to demonstrate that the surface texture depended on the fabrication material and appeared the roughest for BSA.

Up to date, the most frequently used biopolymers for 2PP of hydrogels are BSA and methacrylated gelatin [66][65][67]. BSA has been studied extensively, determining efficiencies dependent on initiator and polymer concentrations as well as additional characteristics such as maximal resolution possible [79][80]. Lay *et al.* showed for example, that a certain threshold viscosity of BSA in solution was required to enable efficient 2PP. They demonstrated that the addition of a viscosity enhancer (polyvinylpyrrolidone = PVP) improved the microstructure integrity after development which is illustrated in Figure 1.16 [81].

2PP of BSA with RB were used in a series of studies fabricating hydrogel structures to encapsulate bacterial colonies in a confined space in order to control bacterial population population size [82]. They entrapped single bacterial cells in microfabricated

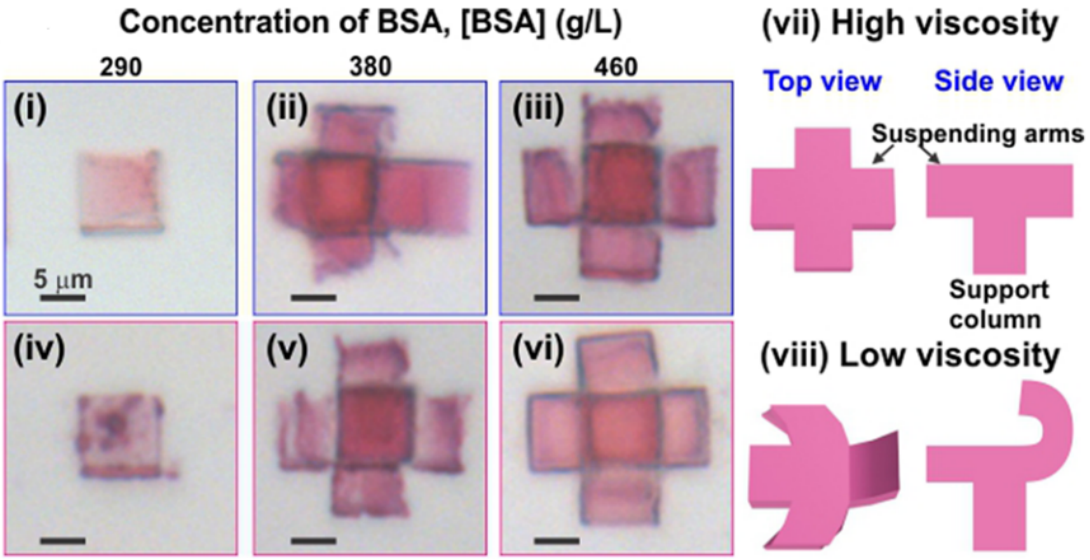


Fig. 1.16 Optical microscopy images of free-standing BSA microstructures made from BSA photoresists, (iiii) without (polyvinylpyrrolidone) PVP added and (ivvi) with 10 g/L PVP. (vii, viii) Schematic illustration of how drifts in photoresists affect the structural integrity of microstructures. Figure adapted from Lay *et al.* [81].

hydrogel structures and demonstrated that the cells remain viable within structures, growing normally compared to bacteria growing in a flask (Figure 1.17A and B). They concluded that this is due to the fact that the hydrogel structures are permeable for nutrients and signal molecules so that the bacteria can access nutrients for growth when the microstructures are placed within a growth medium, allowing them to proliferate normally. Using this approach, Connell and co-workers showed for example, that the ability to produce signal molecules via which bacteria communicate depends on the density of the population. Based on these results, Connell *et al.* optimized the photoresist composition to print in the presence of living cells by adding unmodified gelatin to the BSA/RB solution [83][63][84]. The improved photoresist composition gelates at room temperature which immobilizes the bacterial cells within the photoresist allowing to print around single bacterial cells as opposed to trapping them within the microstructures after the fabrication (Figure 1.17C). The highly increased viscosity of the photoresist also improves the polymerization efficiency. Higher viscosities often improve the 2PP efficiency due to reduced diffusion of molecules which especially

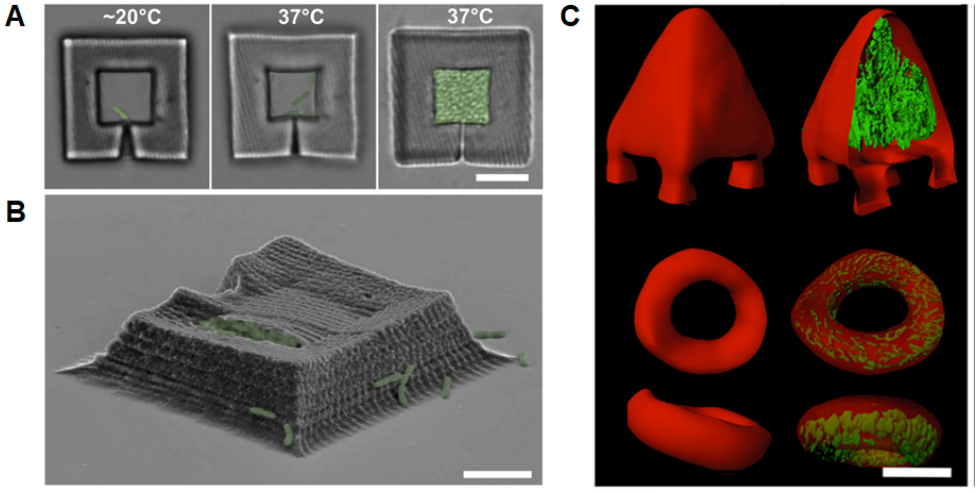


Fig. 1.17 A) DIC micrographs of *P. aeruginosa* captured in a 2PP hydrogel consisting of BSA and RB. A cell swims into the lumen of a trap (left), the entry pore is constricted by increasing the temperature to 37°C (middle), and the bacteria grow and fill the trap *P. aeruginosa* (right), scale bar = 10 μm. B) SEM image of the dehydrated hydrogel structure filled with *P. aeruginosa*,scale bar = 5 μm. C) Confocal fluorescence isosurfaces show isolated *P. aeruginosa* microcolonies within a surface-anchored 2pL pyramid (Top) and an untethered 3 pL torus (Bottom). Cells are false-coloured green for visualization, scale bar = 20 μm. Figure adapted from Connell *et al.* [82][83].

affects the termination reaction of the polymerization strongly [61].

Gelatin modified with methacrylate groups (GelMOD) is a popular material for tissue engineering in general [18], and in particular for 2PP. As a natural biopolymer derived from connective tissue, gelatin offers cell recognition sites and comes close to the physical environment of cells. Most importantly, it is easy to process and shows good polymerization efficiency. Ovsianikov and co-workers were the first to apply methacrylated gelatin (GelMOD) for 2PP in combination with the UV photoinitiator Irgacure2959 [66]. They started by optimizing the fabrication of simple scaffold structures for cell seeding. These structures were shown to support porcine mesenchymal stem cell (MSC) adhesion and differentiation into osteogenic lineage [66] (Figure 1.18). In 2014, Ovsianikov *et al.* developed this method further by demonstrating printing in the presence of living mammalian cells by applying a novel water-soluble photoinitiator with improved 2PA cross-section as well as improved biocompatibility, namely P2CK discussed above [65]. Figure 1.19 shows the successful encapsulation of cells within

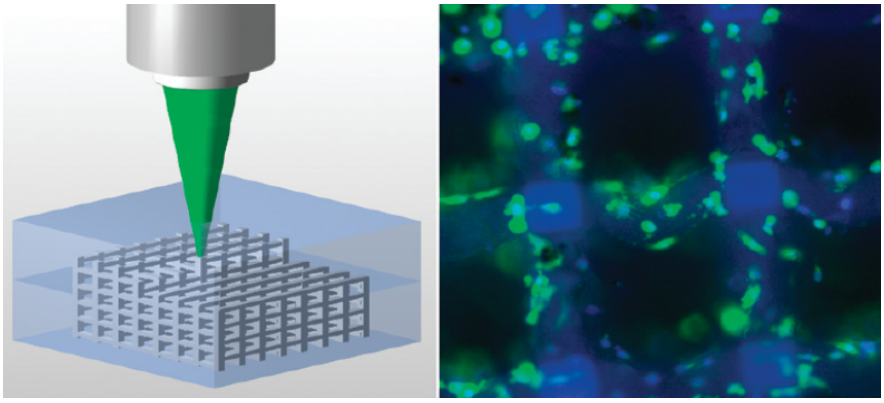


Fig. 1.18 2PP of three-dimensional scaffolds from photosensitive gelatin to support the adhesion and differentiation of porcine mesenchymal stem cell's (MSC's) for applications in tissue engineering [66].

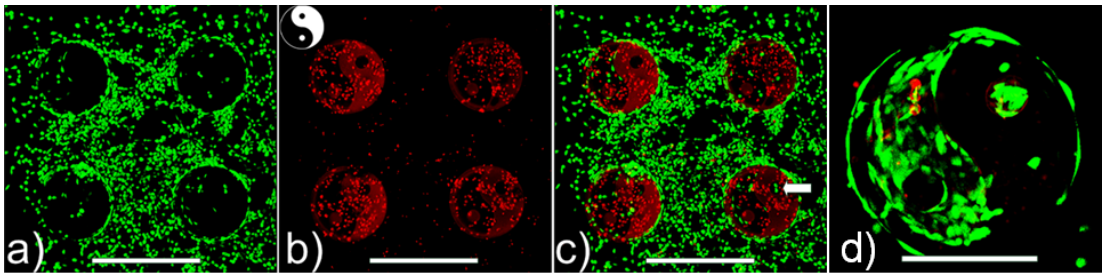


Fig. 1.19 Viability of cells encapsulated in gelatin-based hydrogel structures produced by 2PP: a) Green-stained live cells; b) Red-stained dead cells; c) Overlay, with an arrow indicating two live cells trapped within a cylindrical void, scale bar = 500 μm; d) Proliferation of MG63 cells trapped within the voids of a 2PP hydrogel construct after 3 weeks in culture, scale bar = 1 mm. Figure adapted from Ovsianikov *et al.* [65].

a 2PP hydrogel structure. After three weeks the few cells that survived within the polymerized structure proliferated and spread throughout the hydrogel construct. Based on control experiments, they concluded that the cells were initially damaged by reactive species produced during 2PP rather than the irradiation process itself [65].

More recently, Hoorick *et al.* aimed to improve the polymerization efficiency and the mechanical integrity of 2PP hydrogels using modified gelatin. For that purpose, they functionalized the primary amines of the gelatin using methacrylamide as for GelMOD and functionalized the carboxylic acids additionally with 2-aminoethyl methacrylate (AEMA) to increase the amount of overall functional groups attached to the gelatin substantially. They show that the heavily functionalized gelatin (gel-MOD-AEMA)

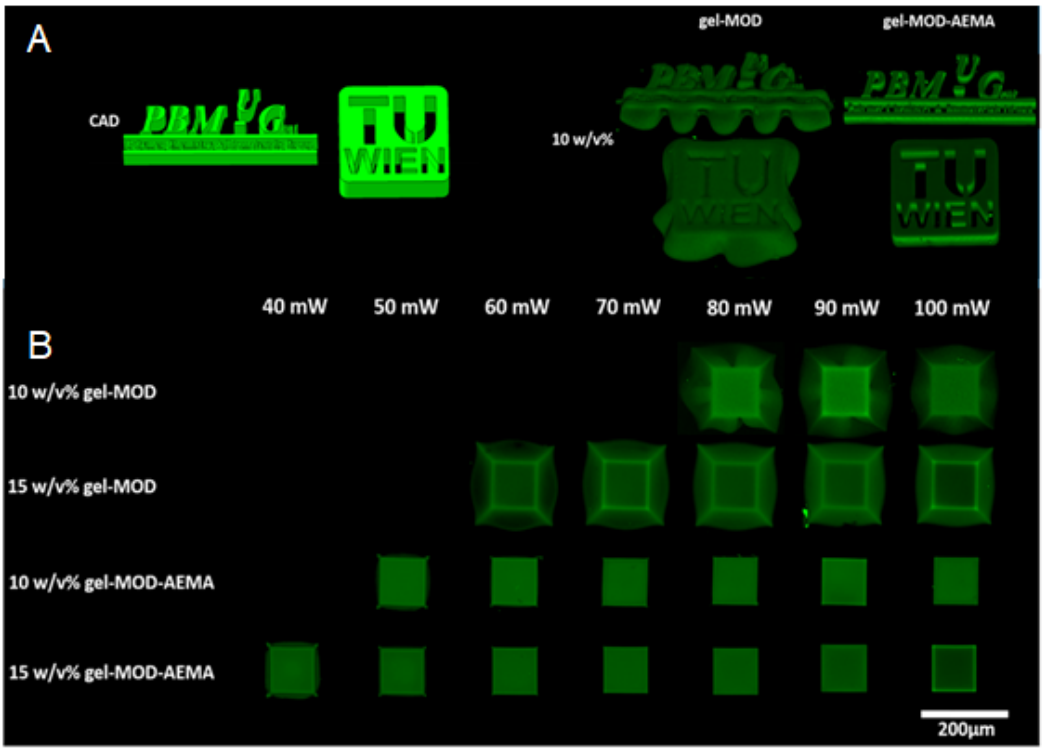


Fig. 1.20 Comparison of swelling-related deformation between Gel-MOD and Gel-MOD-AEMA. A) Applied CAD model and structured university logos expressing clear differences in swelling and swelling-related deformations between gel-MOD and gel-MOD-AEMA at different concentrations. B) Semiquantitative analysis of structuring range and related swelling for both derivatives via 3D renderings of the generated cubes (100 μm × 100 μm × 100 μm), imaged through the glass slide after 24 h of incubation at 37°C. Figure adapted from Hoorick *et al.* [67].

results in faster crosslinking kinetics compared to the conventional GelMOD, whilst reducing post fabrication deformation due to swelling and maintaining its compatibility to host living cells [67]. Figure 1.20 illustrates the reduced deformation of gel-MOD-AEMA in direct comparison to gelMOD for different gelatin concentrations of the photoresists. The degree of deformation was determined on the basis of fluorescence images of hydrogel cubes with the dimensions 100 μm × 100 μm × 100 μm and their University logo.

Only few other hydrogels using biopolymer precursors were reported so far. However, these examples using hyaluronic acid, collagen and chitosan appear to be proof-of concepts so far because they lack any further experiments investigating the 2PP effi-

ciency, mechanical integrity of the hydrogel microstructures after development as well as practical applications using those microstructures.

For example, Hyaluronic acid modified with glycidyl methacrylate (HAGM) in combination with Irgacure2959 was investigated for its suitability to fabricate microstructures using 2PP [85]. Comparably low scan speeds were necessary to achieve sufficient polymerization of HAGM namely 0.3 mm/s were used at an average laser power of 5 mW. In direct comparison, 3D hydrogel structures out of GelMOD in combination with the same photoinitiator Irgacure2959, were fabricated at the laser scan speed 10 mm/s using a lower average laser power of 3.5 mW [66] [85]. Figure 1.21 shows light microscope images of HAGM based microstructures fabricated using 2PP. These results suggest that further improvement of the processability of HAGM would be necessary to fabricate structures within a reasonable time frame. Kufelt *et al.* proposed and tested the approach of using hybrid materials based on HAGM mixed with a copolymer to improve the polymerization, e.g. with poly(ethyleneglycol) diacrylate (PEGDA) which allowed to increase the scan speed to 1 mm/s.

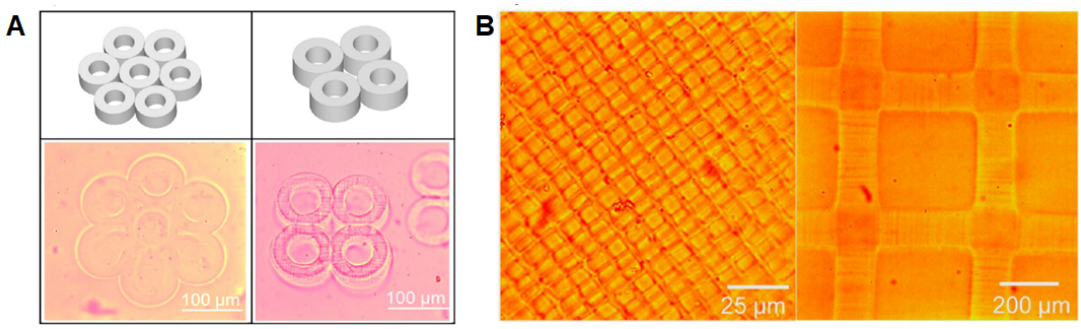


Fig. 1.21 Microscopic images of 2PP hyaluronic acid (HAGM) scaffold geometries. A) One-layered ring-like structures according to the applied CAD models; B) Grid structures with different pore sizes. Figure adapted from Kufelt *et al.* [85].

A different modification of hyaluronic acid was later on tested with 2PP namely tyramine-substituted hyaluronic acid (HA-Tyr) which facilitated the photo-crosslinking [86]. Although, Loebel *et al.* demonstrated effective UV polymerization of HA-Tyr, the 2PP results appear preliminary and only demonstrate weak crosslinking using the dye EosinY

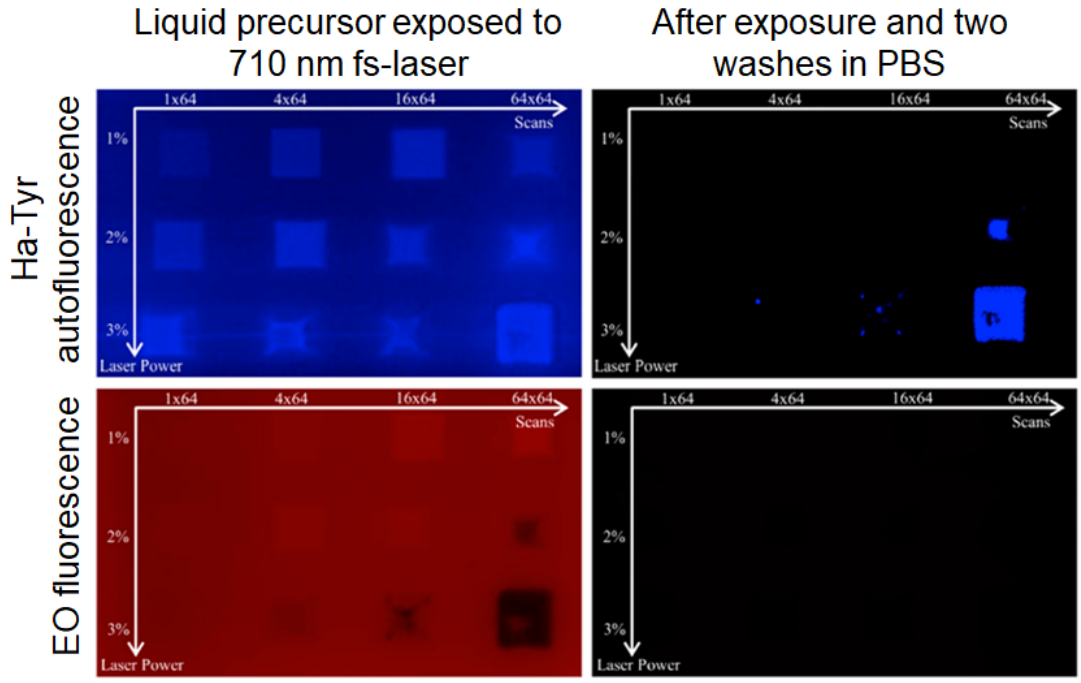


Fig. 1.22 Fluorescence images of 2PP fabricated structures based on HA-Tyr with EosinY. Liquid HA-Tyr precursor exposed to two-photon irradiation (left) and after exposure and two washes in PBS (right). Number of scans (per line x layer) is varied on the x-axis. Laser power is varied on the y-axis (1, 2, and 3% correspond to 1.55, 2.25, and 2.85 mW delivered at the sample). Photo-crosslinked cubes in the array are 10 μm in each dimension and imaged at mid-depth.

(EO) as the photoinitiator (Figure 1.22).

Kufelt *et al.* applied the same approach of attaching a glycidyl methacrylte to the biopolymer chitosan to make it photosensitive and suitable for 2PP. Similarly to the hyaluronic acid however, the processability of pure CHGM was not efficient enough and was part of a hybrid photoresist consisting of CHGM and PEGDA as tested for CHGM before. They reported an average laser power of 35 mW at a scanning speed of 3 mm/s to obtain high quality structures for pure CHGM in solution as well as for the hybrid photoresist CHGM and PEGDA [87]. Example structures of 2PP fabricated CHGM and CHGM-PEGDA blend are shown in Figure 1.23.

A most recent approach demonstrates a positive tone resist (i.e. removal of photo-sensitive material upon light irradiation) based on a hydrogel composed of HA and PEG with integrated photolabile *o*-nitrobenzyl (oBN) derivatives that were shown to

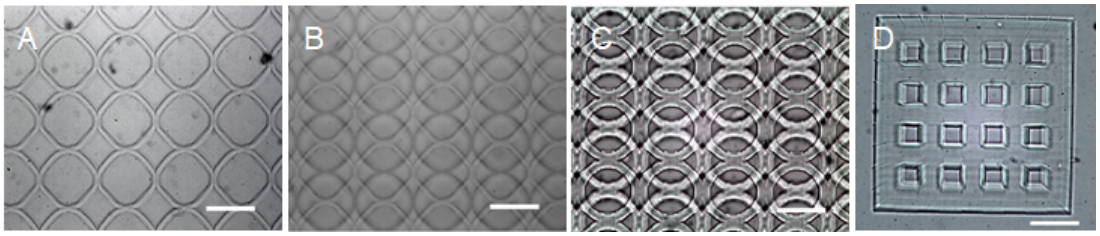


Fig. 1.23 Optical microscope images of ring-like microstructures fabricated of photosensitive CHGM hydrogel using 2PP. A) Single layer of CHGM; B) Stacked double layer of CHGM; C) Stacked double layer of CHGM with ring thickness of 30 μm; pore size: 180 μm (scale bars = 200 μm. D) 2PP-fabricated CHGM-PEG blend grid structure (scale bar = 100 μm). All images were taken at 10x magnification. Figure adapted from [87].

be biocompatible with living cells [57]. Versatile approaches like the work described by Lunzer and co-workers, demonstrate the adaptability of two-photon fabricated hydrogels. In this example, hydrogels can be dynamically tuned to allow the controlled adaptation of the micro-environment surrounding living cells. Figure 1.24A illustrates two-photon micro-patterning of the preformed hydrogel using a focused NIR-laser to erode polymerized material. Lunzer *et al.* showed that they could improve the efficiency of the the oNB ester cleavage upon two-photon excitation by adding the two-photon active small molecule P2CK that was previously introduced as an efficient water-soluble photoinitiator. Cytocompatibility was demonstrated by encapsulating adipose-derived mesenchymal stem cells (asc/tert1) within the PEG-HA-SH hydrogels. After 24 hours, the hydrogels were soaked in a solution of P2CK for 5.5 hours which then allowed to cleave the hydrogel in horseshoe-patterns connected to the encapsulated cells. After 14 days, the cells were still viable and spread throughout the entire channel structures (Figure 1.24B).

In summary, considerable effort has been invested into improving 2PP of hydrogels to enable efficient processing for medical applications and fabricate structurally stable as well as biocompatible hydrogel structures. Whilst synthetic polymers can be applied to obtain efficiently fabricated hydrogels, suitable monomers are currently restricted to PEG based materials. The major advantages of 2PP hydrogels, that stand out from other

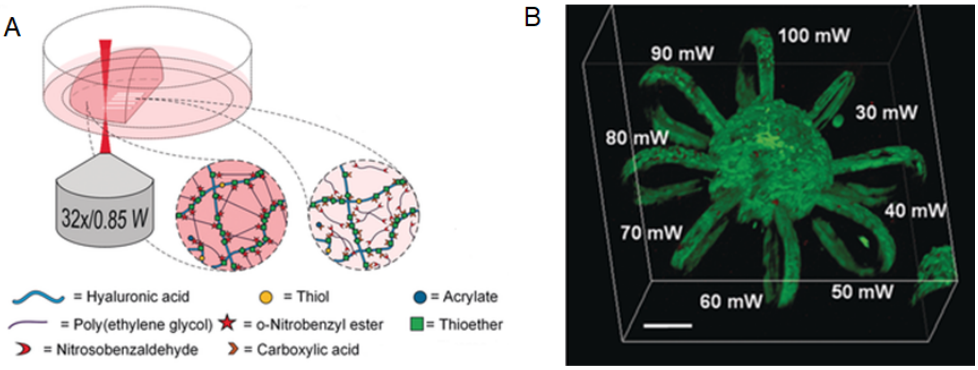


Fig. 1.24 Two-photon patterning of photodegradable hydrogels based on a composite material of hyaluronic acid (HA), PEG with integrated photolabile *o*-nitrobenzyl derivatives. A) Schematic illustration of 2PP of a preformed hydrogel using a focused NIR-laser; B) Cell spreading into micro-loops. GFP-labeled ASC-TERT1 spheroids were encapsulated in PEG-HA-SH hydrogel. The cells were viable after 14 days and populated all channels that were fabricated at different laser powers. Figure adapted from Lunzer *et al.* [57].

AM techniques, are the unprecedented resolution and the ability to print in the presence of living cells. This can best be exploited using materials with minimal cytotoxicity and maximal structural similarity to natural cell environments. The literature on 2PP for biomedical applications suggests that biomaterials are currently most suitable for this. Despite increasing research efforts in developing 2PP photoresist on commonly used biopolymers such as hyaluronic acid and chitosan, the printing efficiencies and structures are often not yet satisfying. Consequently, BSA and modified gelatin are currently the most applied materials for 2PP of hydrogels. The advances in synthesising novel water-soluble and 2PP efficient photoinitiators however, are paving the way for novel 2PP photoresists. Effective 2PP initiators could bypass the challenge of inefficient polymerization for biopolymer based photoresists and facilitate fast and accurate 2PP of hydrogels.

1.4 Thesis rationale

One of the major drivers for the future of medicine is a current societal challenge of an ever ageing population. An increasingly older population worldwide has lead to increased demand of organ transplantations which can not be matched by adequate numbers of organ donors resulting in a major organ shortage crisis [88].

A revolutionising approach is to regenerate tissue and even whole organs from cells cultured in laboratories which would also eliminate the problem of immune responses rejecting foreign body material. Regenerative medicine (RM), a multidisciplinary research field including biomaterials, stem cell biology, tissue engineering and the production of artificial organs is tackling these challenges today. The medical research council (MRC) defines RM as a scientific field that can help repair or replace damaged or diseased human cells or tissues to restore normal function. This requires combined efforts from many research areas due to the complexity and diverse challenges the artificial regeneration of functional tissue holds. For simplicity, these challenges can be divided into three main scientific areas to be addressed. The advancement of biomaterials that are resembling natural conditions and are enduring within a living organism. Development in culturing cells, especially primary cells obtained from patients and 3D cell culture [89]. Lastly, vascularisation of tissue replacing the function of blood vessels that allow for the exchange of nutrients, waste products and oxygen within the tissue.

The work presented in this thesis is structured in three main results chapters discussing an overarching aim each as outlined in the following.

The first aim was to develop a novel highly efficient photoresist for two-photon polymerization (2PP) using alginate that facilitates the microfabrication of alginate hydrogels with unprecedented resolution. For this purpose, two different chemistries are tested to synthesise methacrylated alginate. Three Degrees of Functionalisation (DoF) are produced and will be confirmed using nuclear magnetic resonance (NMR) spectroscopy. The varying alginate molecules will then be tested for two-photon polymerization.

The second aim discussed in Chapter 4, was to probe the alginate photoresists for its 2PP efficiencies and study the importance of the DoF with cross-linker groups versus alginate concentration that goes along with higher photoresist viscosities. Optimal printing parameters will be identified for each photoresist composition and a set of experiments will be performed to study the 2PP kinetics of alginate that could inform the development of novel photoresists in general.

The final aim was to demonstrate that the 2PP alginate hydrogels are cytocompatible and support the attachment and growth of representatives for bacterial cells and human stem cells. The results summarised in Chapter 5 show cells growing on alginate hydrogels featuring smart microstructures with the aim to influence the attachment of all tested cell types. A variety of microstructured surfaces will be screened for their potential to reduce bacterial attachment. Another set of surfaces will be probed on its suitability for culturing human mesenchymal stem cells (MSCs), testing for surfaces that influence the attachment and morphology of MSCs.

2PP of alginate hydrogels mainly feeds into one of the greater goals in regenerative medicine, providing protective cell carriers in form of 3D hydrogel structures, ideally with smart features to direct cell growth, proliferation and differentiation in a controlled way.

Chapter 2

Methodology

2.1 Two-photon polymerization

All 2PP experiments were performed on the commercially available *Nanoscribe* system (Photonic Professional). The set-up is equipped with a near infrared (NIR) fiber laser, a high-sensitivity microscope camera for real time observation of the printing process and an ultra-precise piezo mode for arbitrary 3D trajectories (FBMS) as well as the high-speed galvo mode (MBFS) for fast structuring in a layer-by-layer fashion. The laser features a center wavelength of 780 nm with a pulse repetition rate of 80 MHz and pulse duration of approximately 100 fs.

2.1.1 CAD design and structure optimisation

The designs for each structure presented in this work were created using the computer-aided design (CAD) software Spaceclaim (Ansys Inc). The 3D structure files can be exported in the form of a standard tessellation language (STL) file which then can be translated into a *dwl*.file, the final format that is being applied to simulate the laser path according to a desired 3D structure. The software *DeScribe* (Photonic Professional) offers several options to adapt the *dwl*.file which can be applied to optimize the

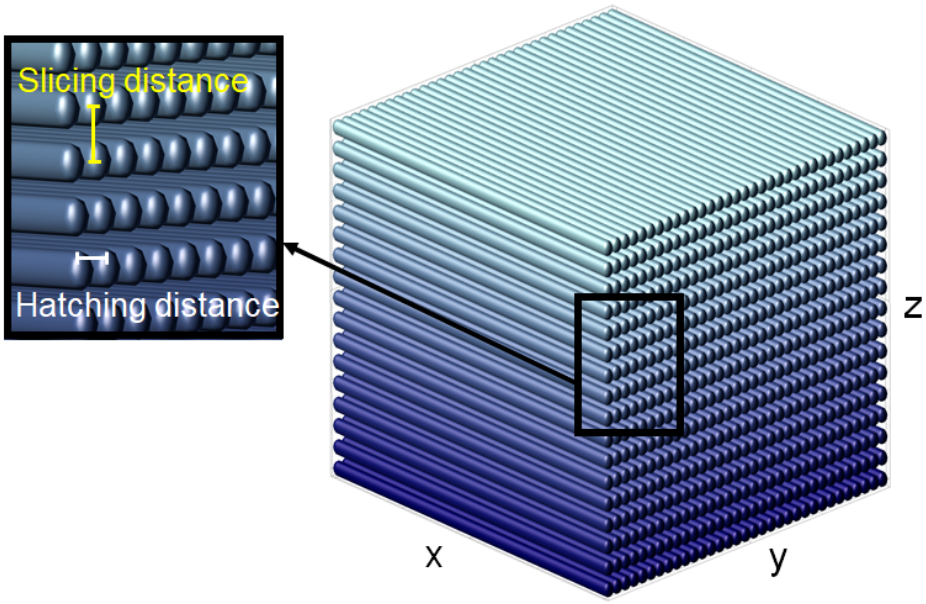


Fig. 2.1 Laser path of simple cube structure showing the slicing and hatching distance that can be adjusted and requires optimization for each photoresist to achieve a stable microstructure.

micro-fabrication result. Optimal printing parameters are characteristic for a particular photoresist and have to be assessed in order to ensure good quality microfabrication. After importing the STL model, printing parameters such as 'hatching' and 'slicing' have to be defined (Figure 2.1). *DeScribe* reads the STL file and slices the object by intersecting the 3D solid with a series of parallel planes in which the distance between the planes can be adapted. For each plane, *DeScribe* computes the intersection contours of the solid with the plane and subsequently fills each obtained contour with a line hatch (Figure 2.1). The optimal slicing and hatching distance are ultimately dependent on the size and shape of the volume, called voxel, that is being polymerized by a single laser exposure. It was found experimentally that voxels in 2PP mostly exhibit an ellipsoid shape with a higher axial than lateral length [90](Figure 2.2). This shape has to be considered when determining the optimal slicing and hatching distances for a given photoresist and parameters applied.

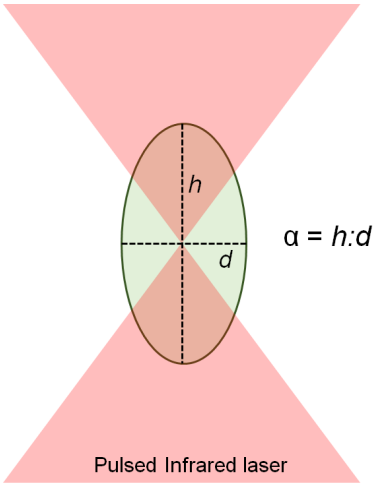


Fig. 2.2 Schematic of the typical voxel shape of a 2PP reaction volume. The voxel aspect ratio α is defined as the ratio of the axial length to the lateral length of the ellipsoid shape.

2.1.2 Sample preparation and development

Glass coverslips (22 mm $\times$ 22 mm) served as the substrates in all experiments. They were first rinsed with acetone ($\geq$99.9%, Sigma-Aldrich) to remove all organic residues followed by isopropanol (IPA) (anhydrous 99.5% Sigma-Aldrich) to wash off the contaminated acetone and then blow-dried with nitrogen. The cleaning facilitated better attachment of the printed microstructures and helped to contain the spreading of the photoresist droplet on the substrate. The coverslips were then fixed to the provided sample holders using sticky tape (Photonic Professional GT, Nanoscribe GmbH). A drop of immersion oil was applied on the bottom of the substrate and approximately 40 μL of photoresist were pipetted on the top side of the substrate (Figure 2.3A). The laser then scans through the photoresist according to a CAD design file starting at the glass/photoresist interface to ensure the attachment of the printed microstructure to the substrate. After the polymerization process, the microstructure as well as non-polymerized photoresist remain on the substrate which are being removed in the development step by washing the sample with a solvent the monomer is soluble in (Figure 2.3B and C), this is water in the case of 2PP of hydrogels. All photoresist

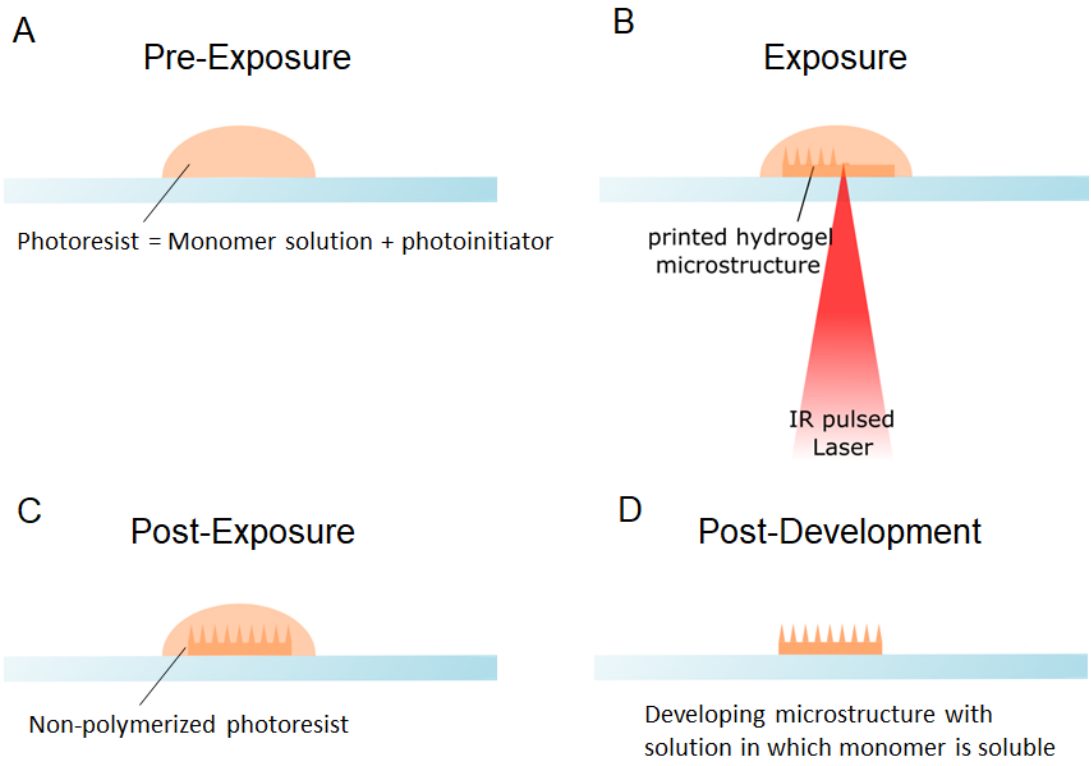


Fig. 2.3 Schematic of 2PP procedure for the microfabrication of hydrogels. A) Drop of photoresist casted onto glass coverslip, B) the laser scans through the photoresist according to the prepared design file starting from the glass/photoresist interface to ensure attachment of the microstructure to the glass substrate, C) the microstructure as well non-polymerized material remain, D) In a development step all non-polymerized material is washed in a solvent the monomer is soluble in.

solutions in this work were prepared beforehand and stirred for at least an hour at 50°C to ensure that the polymers were fully dissolved. Shortly before the printing, a water-soluble photoinitiator, P2CK for methacrylated alginate and Rose bengal (RB) for BSA, was added to the mixture and stirred for a few minutes before further processing. Figure 2.4 illustrates a sample of methacrylated alginate with P2CK on a sample holder provided by Nanoscribe GmbH. An additional spacer, that was 3D printed in-house, was sealed with silicon and another glass coverslip on top was used for long prints to avoid dehydration of the sample. The pre-designed gwl.file could be uploaded to the printing software *Nanowrite*. Provided that the interface between the glass substrate and the photoresist was identified, either automatically or manually, the direct laser writing

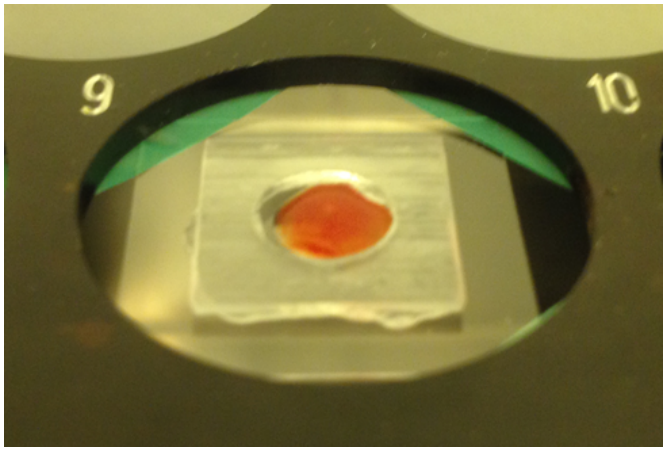


Fig. 2.4 Enclosed 2PP sample prepared on a sample holder.

procedure was started. The integrated microscope camera enabled the live observation of the printing process in real time. For the following removal of non-polymerized monomers (commonly termed *development* of the printed structure), the substrates were incubated in a warm water bath (T = 50°C) for approximately 15 minutes and subsequently blow-dried with an air gun.

2.2 Microscopy techniques for studying microfabricated structures

2.2.1 Bright-field microscopy

The bright field microscope Eclipse LV100ND (Nikon) with the NIS-Elements Imaging software was used to image 2PP hydrogel structures. 10x, 20x and 50x objectives were used depending on the individual experiment.

2.2.2 Scanning electron microscopy

Scanning electron microscopy (SEM) was used to obtain 3D images of the 2PP hydrogel microstructures by tilting the sample 0-45° and to resolve nanometer features. All samples were dried overnight and sputter coated with platinum to a nominal thickness

of about 10 nm to provide a conducting layer for SEM imaging. They were imaged using a table-top SEM by Hitachi TM3030 and FEI Quanta 650 if not specified otherwise.

2.2.2.1 Cryogenic SEM

Cryo-SEM enabled the imaging of frozen hydrated hydrogel structures fabricated using 2PP. The FEI Quanta 200 3D Dual Beam FIB-SEM system (Thermo Scientific Fisher) was used at high vacuum mode and 10 kV applying a tilt of 45° for all shown images. With the PP2000 Cryo-SEM preparation system, the sample was rapidly cooled by means of liquid nitrogen and transferred under vacuum to the cold stage of the preparation chamber, which is mounted on to the SEM chamber. The preparation chamber was pumped by a specially designed turbomolecular pumping system. The sample could then be loaded into the SEM chamber under vacuum where it was mounted on a cold stage specifically tailored to the SEM. At all stages of the procedure the sample was maintained at temperatures below -140°C.

2.2.2.2 SEM imaging of cells

SEM was used to examine the quality of the 3D printed architectures using Hitachi TM3030 and FEI Quanta 650 if not otherwise stated. Mesenchymal stem cells (MSCs) were imaged after being cultured for 48 hours on two-photon fabricated alginate hydrogel surfaces. Bacterial cells were imaged after being incubated for about 15 hours on two-photon fabricated alginate hydrogel. Samples were fixed in a series of solutions in the order listed below, each immersed for 15 minutes: 5% glutaraldehyde (VWR International Ltd), HEPES-NaCl buffer (pH 7.4), HEPES-NaCl buffer (pH 7.4), deionized water, 50% ethanol (EtOH), 100% EtOH, 50% EtOH – 50% methanol(MeOH), 100% MeOH, and 100% MeOH. After air drying overnight. The samples were coated with a thin platinum layer using a sputter coater to provide a conducting layer for SEM imaging.

2.2.3 Confocal fluorescence imaging

Laser scanning confocal microscopy (CSCM) enabled the visualisation of 3D hydrogel structures in their hydrated state using the laser scanning microscope LSM700 (Zeiss). All images were obtained with an oil-immersion objective (Plan-Apochromat 63x, NA = 1.40, DIC M27). The water-soluble photoinitiators applied in this work both absorb in a similar wavelength range, namely P2CK with an absorption maximum at $\lambda_{P2CK,max}$ = 506 nm [70] and Rose bengal at $\lambda_{RB,max}$ = 540 nm [91]. Therefore, an excitation wavelength of λ = 530 nm was applied. Some of the photoinitiator molecules remain trapped within the microstructures which facilitates the 2PP hydrogel microstructures with fluorescence and can be exploited to image them using confocal microscopy and reconstruct their 3D shape by scanning several parallel planes in z-direction, meaning vertical to the glass slide.

2.3 Viscosity measurements using a liquid handler

A four-channel liquid handling equipment (Microlab STARlet, Hamilton Robotics, Inc.) was used to measure the viscosity of the varying photoresists composed of methacrylated alginate. Using a liquid handler for high-throughput viscosity measurements was developed recently by Deshmukh *et al.* [92]. This approach was further developed and applied by Zhou and co-workers at the University of Nottingham, in order to screen a library of acrylate and methacrylate materials in a high-throughput fashion (manuscript submitted [93]). The liquid handler utilised air displacement pipetting, similar to a handheld electronic pipettor. Each channel was equipped with a pressure sensor to monitor pressure change during the overall aspiration or dispense process. 200 μL of each sample were added into a 1 mL 96-well plate (260252, Thermo Scientific), which was placed in a heating module at 25°C. During the test, four samples were simultaneously aspirated into 300 µL pipettes (235902, CO-RE non-filter tips, Hamilton

Robotics, Inc.) at 10 < μL/s for 20 seconds. The submerge depth was maintained at 2 mm below the liquid surface. Liquids were dispensed back to the well plate to minimise material waste during the test. Thereafter, the channels ejected the used pipettes and replaced them with fresh ones. They were immediately moved to the next position in the well plate to measure the subsequent four samples. The test was automatically run until completion and a pressure versus time curve for each aspiration was generated for analysis. The viscosity could then be calculated with a matlab programme that considered all parameters involved. Details on calculations are not provided in this work. Due to natural inconsistencies of the photoresist compositions, three repeats were measured for each sample.

2.4 Raman spectroscopy

Preliminary Raman spectra were collected at a laser wavelength of λ = 785 nm using a Horiba-Jobin-Yvon LabRAM (Horiba) instrument. Raman spectroscopy was evaluated for its ability to determine the degree of conversion (DoC) of 2PP hydrogel structures. Using Raman spectroscopy to measure the DoC is based on the detection of inelastic light scattering by the vibrational resonances of carbon double bonds (C=C). It has previously been applied for pure monomer solutions as opposed to monomers diluted in water [94][95]. During the crosslinking reaction, the double bonds of the methacrylate groups on the modified alginate are homolytically opened and converted to single bonds (C–C). Therefore, the relative height of the corresponding Raman peak (C=C) is lowered during the reaction polymerization whereas the carbonyl peak (C=O) of the alginate would keep the same and can serve as a reference [94]. The degree of conversion (DoC) can then be calculated based on the ratios of the integrated peaks.

2.5 Bacterial cell culture

2.5.1 Bacterial growth

Bacterial growth can serve as an evaluation of toxicity for certain substances as well as nutritious value of others. All monomers and photoinitiators that were used to fabricate hydrogel structures for culturing of bacteria, were investigated for their effect on bacterial growth. For this purpose, an overnight culture of *Pseudomonas aeruginosa* strain PAO1 or *Staphylococcus aureus* strain SH1000 was grown in Lysogeny broth (LB) medium in a 50 mL Falcon tube at 37°C. The overnight culture was then diluted to an optical density (OD) of 0.01 as the starting point inoculum. Different bacterial cultures were each prepared with a different compound of interest as well as two controls (bacteria only and only LB medium) to permit subtraction of any background absorption caused by the photoinitiator. A total volume of 200 μL of the culture was pipetted in each well of a 96-well flat bottom black polystyrene plate (Greiner). The microtiter plate was then covered with a sterile plastic cover to avoid evaporation and the OD (λ = 600 nm) was measured every 15 minutes at 37°C using the plate reader Infinite®200 Pro (TECAN) for 16 hours.

2.5.2 Bacterial attachment assays

Bacteria were routinely grown at 37°C on LB agar plates. An overnight culture was grown in LB medium in a 50 mL Falcon tube at 37°C. The overnight culture was diluted to an OD of 0.01 as the starting point for the surface attachments experiments. These cultures were then carefully added on top of the glass coverslip containing the alginate hydrogel structures. Samples were then incubated for about 15 hours with gentle shaking (30 rpm) at 37°C. To allow imaging of living cells, both strains used were expressing fluorescent protein genes, namely mturquoise2 and gfp for PAO1 and SH1000, respectively.

2.5.3 Colony forming unit (CFU) count to determine number of viable bacterial cells

A CFU count was performed for *P. aeruginosa* after the growth assay that is described above using the overnight culture. A series of dilutions was prepared out of the overnight culture with the dilution factor 10 down to a minimum dilution of 10^{-6}. All dilutions as well as the original overnight culture were plated on agar plates with three repeats on three separate agar plates for each dilution. The plates were incubated overnight at at 37°C. All visible colonies were counted the following day and used to calculate the CFU. Only dilutions with colonies that were distinct from each other were used to calculate the CFU as the counting error increases with too many as well as too few colonies on the plates. The CFU per 1 mL culture was calculated as follows:

$$CFU/mL = \frac{No.\,of colonies \times dilution}{Volume\,of\ plated\ dilution} \tag{2.1}$$

2.5.4 Encapsulation of living cells

The *Pseudomonas aeruginosa* strain PAO1 constitutively expressing the fluorescent marker *mCherry* was grown with shaking in tryptic soy broth (TBS) overnight (≈18 hours). The following day the culture was diluted to an OD of 0.01 (λ = 600 nm) and grown until the mid-logarithmic growth phase was reached after 2-3 hours. Subsequently, the culture was mixed with the photoresist solutions in a 1/10 ratio at 37 °C. The bacteria mixed into the photoresist solution were immediately applied to glass coverslips to fabricate 3D microarchitectures around bacterial cells using the *nanoscribe* system described above. To avoid contamination of the samples, the photoresist droplet containing living bacterial cells was embedded in a closed environment. Therefore, a spacer was placed on top of the glass coverslip and covered by another glass coverslip as illustrated in Figure 2.5. An in-built camera permitted viewing the printing process in real time. Single bacterial cells could not be identified because of too little contrast between the

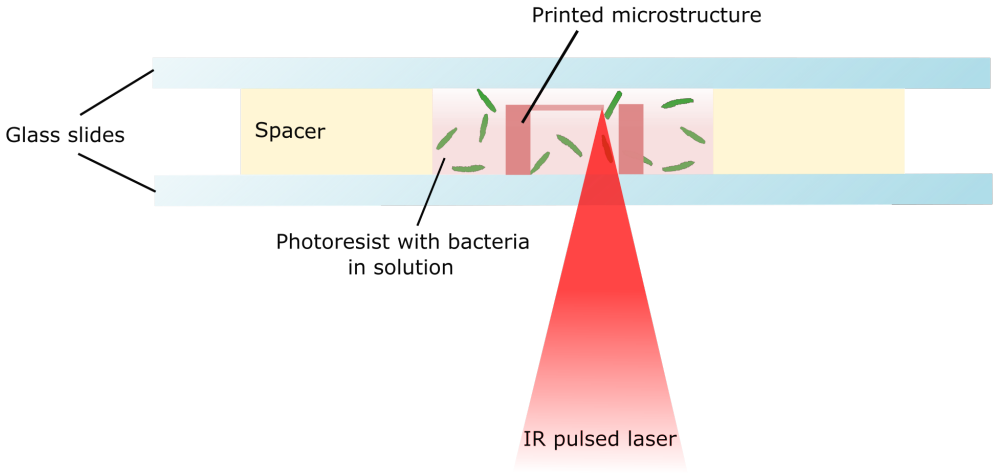


Fig. 2.5 Schematic of two-photon polymerization of hydrogel microstructures to encapsulate bacterial cells. The photoresist consists of BSA/gelatin with rose bengal as the photoinitiator. This solution was mixed with a dilution of *P. aeruginosa* culture at 37°C and cast onto a glass slide which was sealed using another glass coverslip on top separated by a 1.5 mm polymer spacer. An inverted microscope scanned a pulsed near infrared (NIR) laser with a frequency of 80 MHz and a wavelength of $\lambda = 780$ nm through the resin according to a prepared 3D CAD design of desired shape.

bacteria and the photoresist. After printing, the samples were washed several times with TSB medium (37°C) to remove non-polymerised photoresist. The samples were then transferred into sterile 6-well plates with fresh TSB medium and incubated at 37°C overnight for about 15 hours. The following day, the glass substrates were washed 3-4 times with phosphate buffered saline (PBS) (1x, pH=7.4, Sigma-Aldrich) for further image analysis.

2.6 Mammalian cell culture

The cell culture experiments were performed by Mahetab Amer at the Centre for Biomolecular Sciences (CBS), University of Nottingham. Immortalised human mesenchymal stem cells (hMSCs), generated in-house, were used for all experiments involving mammalian cell culture. The cells were prepared in Dulbecco's Modified Eagle's Medium (Gibco Life Technologies, Paisley, UK) supplemented with 10% v/v fetal calf serum (FCS), 1% (v/v) penicillin-streptomycin and 1% L-glutamine. For

routine passaging, a standard trypsinisation protocol was carried out using 0.25% w/v trypsin/2 mM Ethylenediaminetetraacetic acid (EDTA) solution. After trypsinisation, which detaches the cells from the substrate, the cells were centrifuged at 180xg for 5 minutes, and then reconstituted to the required cell density. The cell containing solution was then carefully added on top of the microfabricated alginate hydrogels that were attached to untreated glass coverslips and placed in a 6 well-plate, respectively. A hemocytometer was used to count the number of cells of 20 μL cell suspension. A final cell density of 15,000 cells/cm^2 was applied for all live/dead stain assays and 10,000 cells/cm^2 for scanning electron microscopy of hMSCs.

Assessment of cell viability was performed using a Live/Dead (viability/cytotoxicity) assay according to the manufacturer's instructions (Invitrogen Life Technologies, Paisley, UK). Calcein AM and ethidium homodimer-1 (EthD-1) were prepared in PBS to produce the Live/Dead staining solution. Samples were visualised using fluorescence microscopy (Leica Microsystems Ltd., Milton Keynes, UK), where live cells were stained green and dead cell nuclei stained red. Live-Dead-stained samples were visualised using a Leica DM IRBE microscope with an attached Leica DC 200 digital camera (Leica Microsystems Ltd., UK). SEM imaging was carried out using the JEOL 6060LV variable pressure scanning electron microscope (Jeol, UK) after coating with a thin layer of gold using a Leica EM SCD005 Sputter Coater.

Chapter 3

Chemical modification of alginate to facilitate two-photon polymerization

3.1 Introduction

This work aimed to develop a method that allows for the microfabrication of 3D alginate hydrogel structures using two-photon polymerization (2PP). Alginate is one of the most prevalent biopolymers used for hydrogels due to its biocompatibility, reversible ionic gelation and natural abundance [28]. 2PP enables the fabrication of structures with sub-micron feature size, on the scale of single cells. Combining the high resolution of 2PP with the adaptable and versatile hydrogel properties of alginate would enable to control the mechanical and geometrical properties of artificial micro-environments.

The first hydrogel structures fabricated using 2PP were shown by Pitts *et al.* in 2000, using the unmodified protein bovine serum albumin (BSA) [52]. Up to date, the most frequently used biopolymers for 2PP of hydrogels are BSA and methacrylated gelatin [66][65][67] because they are relatively easy to process and have more favourable mechanical properties in comparison with other natural polymers tested for 2PP. So far, only few other biomaterials (hyaluronic acid and chitosan [96][87]) have been evaluated for 2PP. Success was moderate due to inefficient 2PP and low mechanical

stability [96][87].

The aim of this work was to introduce an alternative to currently used biopolymers for 2PP to extend the limited range of biomaterials that can be processed, and develop an efficient photoresist that enables the microfabrication of robust 3D hydrogel structures. Alginate was selected to be investigated for 2PP because it is is one of the most characterized biomaterials including numerous modifications, cell compatibilities and crosslinking mechanisms promoting a versatile application range [27][28][97][98][99]. A photo-crosslinked and biodegradable hydrogel using methacrylated alginate has been demonstrated by Jeon *et al.* using ultraviolet (UV) light [100]. The physical properties were shown to be tunable and featured excellent cytocompatibility. Based on these promising results, 2PP of alginate would broaden the application scope immensely by allowing the microfabrication of alginate hydrogels with sub-micron feature size as well as the printing in the presence of living cells. 2PP of such micro-structured hydrogels would be particularly valuable in tissue engineering, for example to produce artificial 3D cell environments similar to the natural extracellular matrix (ECM) [101][72][102]. The strategy was to introduce photo-crosslinkable groups to the alginate by modifying it with methacrylate groups (Figure 3.1). In the presence of a suitable photoinitiator, the functionalised alginate can be crosslinked upon the absorption of two-photons. A common approach to modify alginate is to form an amide bond between the carboxylic group of the alginate and an amine group of a small molecule (Figure 3.1) which requires a coupling agent to induce the reaction.

The first coupling reagents to be synthesised were carbodiimides in order to activate the carboxylic acid [103] that were widely used to form peptide bonds [104]. Some drawbacks such as side reactions or complicated purification steps, promoted the development of efficient alternatives such as 2-Chloro-4,6-dimethoxy-1,3,5-triazine (CDMT). Reactions using CDMT as the coupling agent have been found to occur rapidly and essentially quantitatively in a one-pot, one-step procedure [105][106]. The choice of coupling reagent is critical and depends on the different reactants.

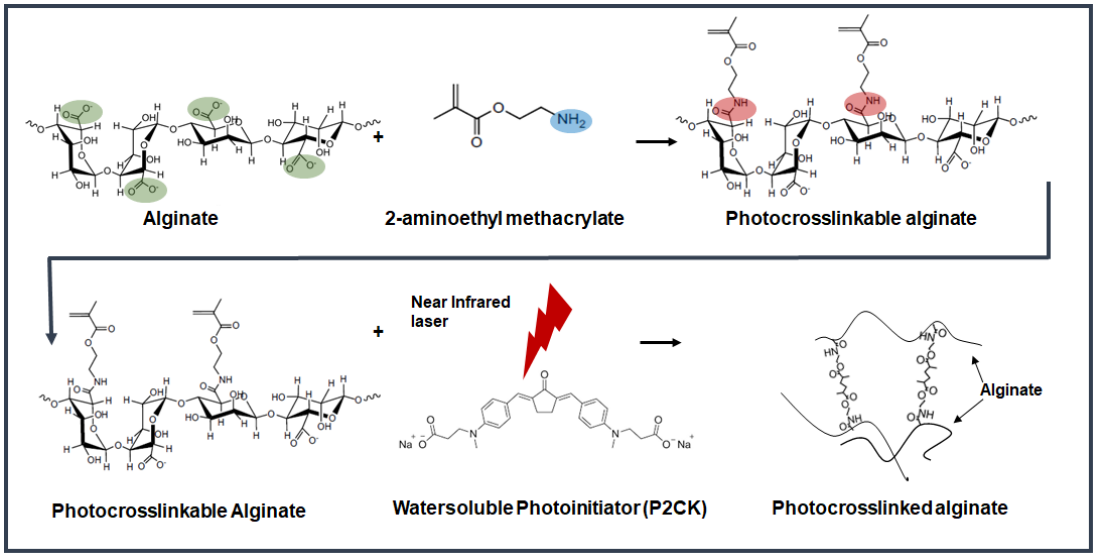


Fig. 3.1 Schematic of the chemical modification of alginate to facilitate two-photon polymerization (2PP). Alginate is chemically functionalized with 2-aminoethyl methacrylate (AEMA) to make it photo-crosslinkable. A carboxylic acid group (green) of a saccharide unit in alginate can form an amide bond (red) with the amino group of AEMA (blue). 2PP is enabled by mixing the photo-crosslinkable alginate with the water-soluble 2PP optimized photoinitiator P2CK [107].

3.2 Experimental Methods

3.2.1 Synthesis of methacrylated alginate

In this work, two different chemistries were tested to determine the most efficient way to synthesize methacrylated alginate. Each saccharide unit in the alginate polymer can theoretically provide a carboxylic acid group (COOH) for reaction as marked in green in Figure 3.1 and react with and amide group (Figure 3.1, blue) via forming an amide bond (Figure 3.1, red). An amidation protocol adopted from Vegas *et al.* [108] using the coupling agent 2-chloro-4,6-dimethoxy-1,3,5-triazine (CDMT) and a protocol adopted from Jeon *et al.* [100] using a carbodiimide based coupling agent were evaluated to attach 2-aminoethyl methacrylate (AEMA) to alginate.

3.2.1.1 Alginate amidation using 2-chloro-4,6-dimethoxy-1,3,5-triazine (CDMT)

Ultrapure very low viscosity sodium alginate with a L-guluronate content of 60 % (Pronova UPVLVG from NovaMatrix) was reacted with 2-aminoethyl methacrylate (AEMA, Sigma), in the presence of CDMT (Sigma) and the base N-methylmorpholine (NMM, Sigma). The quantities of the chemicals were adapted from Vegas *et al.* for a theoretical modification degree of 50 % [108] as follows: 200 mg of alginate was dissolved as a 2 %w/v alginate solution in a 3:2 water:acetonitrile mixture. The amount of available COOH groups for reaction can be calculated based on the molecular weight of the individual sugar units in alginate ($M_{W,G}$ = 193.131 g/mol; $M_{W,M}$ = 194.139 g/mol). Accordingly, 200 mg of alginate equal 1.04 mmol of COOH available for reaction defined here as one equivalent (eq.). One eq. of AEMA (170.9 mg) was then added along with 0.5 eq. of CDMT (90 mg) and 1 eq. of NMM (112 μL). Higher theoretical methacrylation degrees can be obtained by increasing the molar equivalents by the desired percentage used for AEMA, CDMT and NMM relative to alginate. This mixture was then stirred overnight (∼14-16 hours) at 55 °C. Acetonitrile was removed using a rotary evaporator and the resulting product was dissolved in double distilled H_2O (ddH_2O) which was then filtered through a cyano modified silica gel (Silicycle) to remove insoluble precipitate. The filtered alginate solution was purified in a dialysis tube (MWCO = 10 kDa) for ∼24 hours and freeze-dried to yield white powder.

3.2.1.2 Alginate amidation using carbodiimide chemsitry

UPVLVG alginate (see chapter 3.2.1.1) was dissolved as a 1 %w/v in a 50 mM 2-morpholino-ethanesulfonic acid (MES) buffer solution (pH = 6.5) containing 0.5 M NaCl (200 mg = 1 eq. = 1.04 mmol of COOH available for reaction). The quantities of the chemicals were adapted from Jeon *et al.* for a theoretical modification degree of 50 % [100]. The carboxylic acid groups of the alginate were activated by adding N-hydroxy-succinimide (NHS, 55 mg; Sigma) and 1-ethyl-3-(3-dimethylaminopropyl)-

carbodiimide hydrochloride (EDC, 183 mg; Sigma). After 5 min, 79.6 mg of AEMA (Sigma) was added to the mixture with a molar ratio of 1:2:1 for NHS:EDC:AEMA. The mixture was then stirred for 24 hours at room temperature. In order to prepare alginates with varying theoretical methacrylation degrees, the amount of AEMA was changed whilst keeping the molar ratio of all other chemicals constant. The next day, the product was precipitated by adding an excess of acetone which was subsequently removed using a rotary evaporator. The resulting product was then dissolved as 1 %w/v solution in ddH_2O. The alginate solution was purified in a dialysis tube (MWCO = 10 kDa) for ∼24 hours and freeze-dried to yield a white.

3.2.2 ^{1}H NMR characterization

^{1}H NMR spectra were obtained with a Bruker 400 MHz NMR spectrometer. All compounds were dissolved in deuterated water (D_2O). Spectra of the individual small molecules 2-aminoethyl methacrylate (AEMA), L-alanine-benzyl ester hydrochloride (ABEH), Irgacure 2959, UPVLVG alginate and methacrylated alginate were recorded. All spectra were analysed using the software MestReNova (version 6.0.2.) and normalised to the deuterated water (D_2O) peak at 4.79 ppm [109]. In order to determine the actual methacrylation of alginate and the methacrylation efficiency, the spectra of alginate-AEMA mixed with 0.05 %w/v Irgacure 2959 were recorded before and after UV irradiation (λ = 365 nm) for 20 minutes. The ratio of the integrals for the proton peaks of the photoinitiator and the methylene protons of the methacrylate were calculated. The methacrylation efficiency is here defined as the ratio of the actual methacrylation to the theoretical methacrylation:

$$Methacrylation\ efficiency = \frac{Actual\ methacrylation}{Theoretical\ methacrylation}$$

3.2.3 Gel permeation chromatography

Relative molecular weights and polydispersities of the alginate polymers were determined for the alginate with the theoretical methacrylation degrees of 75 % and 50 % using gel permeation chromatography (GPC). The instrument was equipped with a Waters 1515 Isocratic HPLC pump, a Waters 2414 refractive index detector (40 °C), a Waters 2707 autosampler, a PSS PFG guard column and two PFG-linear-XL columns (8 x 300 mm, 7 micron) in series (at 40 °C). The calibration curve was obtained by using poly(ethylene glycol) (PEG) standards. The eluent used was 100 mM $NaNO_3$ with a flow rate of 1 mL min^{-1}.

3.2.4 Two-photon polymerization of methacrylated alginate

The photoresist was composed of 2 %w/v methacrylated alginate dissolved in ddH_2O and adjusted to a neutral pH = 7-8 to increase the solubility of alginate. The photoinitiator P2CK [107] was then added to the mixture using a comparatively high concentration of 1 %w/v as reported in literature to determine if the novel photoresist can be processed using 2PP.

3.3 Results and Discussion

3.3.1 Synthesis and characterization of methacrylated alginate

^{1}H NMR was used to evaluate if the synthesis of methacrylated alginate was successful and to determine the purity of the product. The attachment of 2-aminoethyl methacrylate (AEMA) to alginate was demonstrated by means of ^{1}H NMR spectra collected for pure AEMA, unmodified alginate and methacrylated alginate (Alg-AEMA) as shown in Figure 3.2. The methyl and methylene proton peaks at δ1.9 ppm, δ5.7 ppm and δ6.2 ppm, respectively (Figure 3.2A a) and b)) were here distinct for AEMA and used to confirm the attachment of AEMA to alginate in Figure 3.2C. Spectra of pure alginate

(Figure 3.2B) in direct comparison to Alg-AEMA resemble the distinct peak spectrum of alginate accompanied by the sharp methacrylate peaks of AEMA. The ability of those functional groups to crosslink upon UV irradiation is discussed in the following chapter 3.3.3.

In this work, two different chemistries were tested to form a peptide bond between AEMA's amino group and the alginate's carboxyl groups (see chapter 3.2.1). Two different protocols were tested, one of which is based on a more traditional carbodiimide chemistry [100] and another one using CDMT as the coupling agent [108]. The CDMT based protocol resulted in a considerate amount of unreacted AEMA (a' and b') as well as AEMA attached to alginate in the final purified product (Figure 3.3). Despite of several repeats of the synthesis, this remained to be a consistent result. The alternative protocol for alginate methacrylation using AEMA was therefore applied to produce functionalised alginate [100].

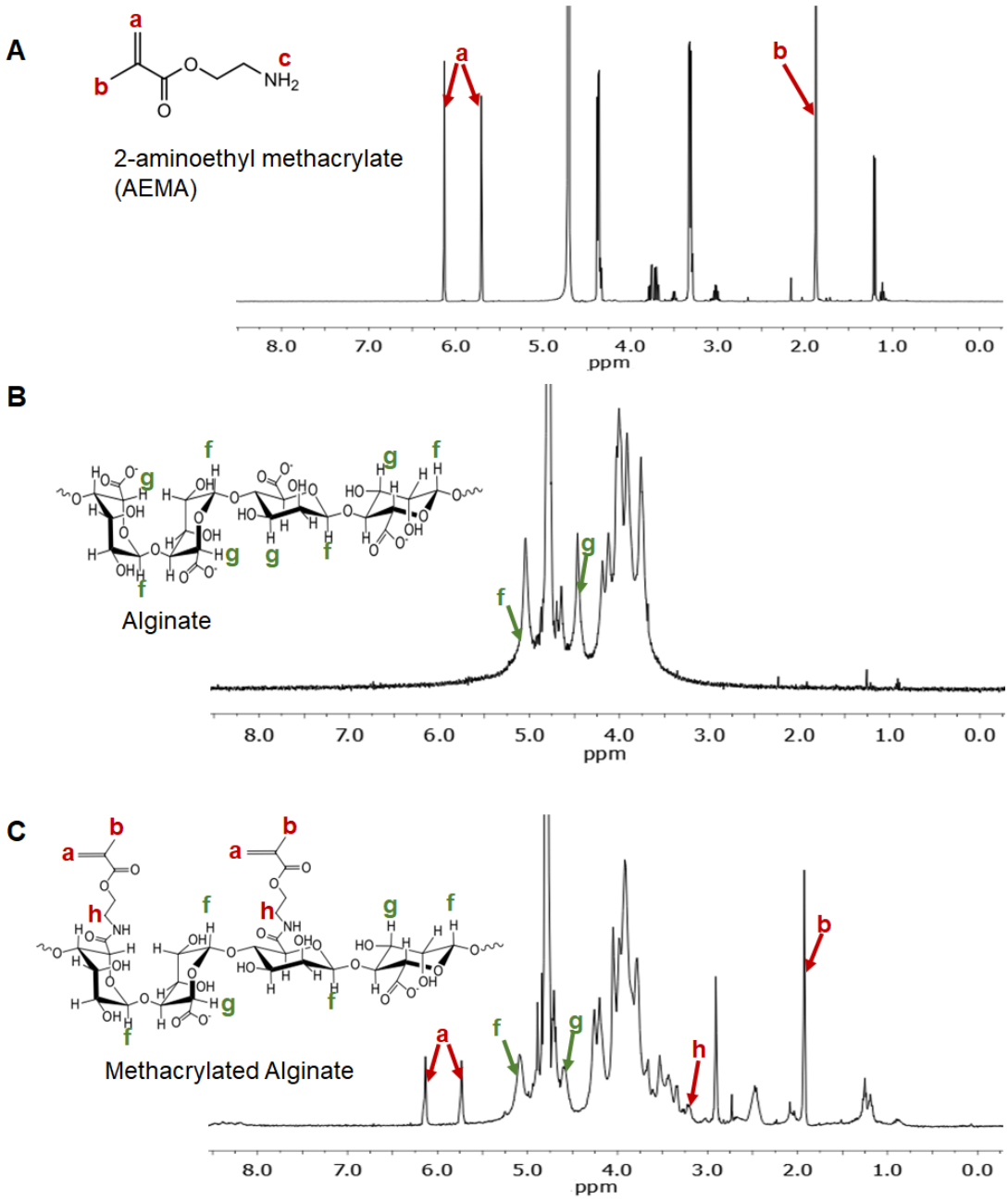


Fig. 3.2 ^{1}H NMR spectra of A) AEMA, B) alginate and C) methacrylated alginate in comparison. Distinct proton peaks used to identify each molecule are highlighted respectively.

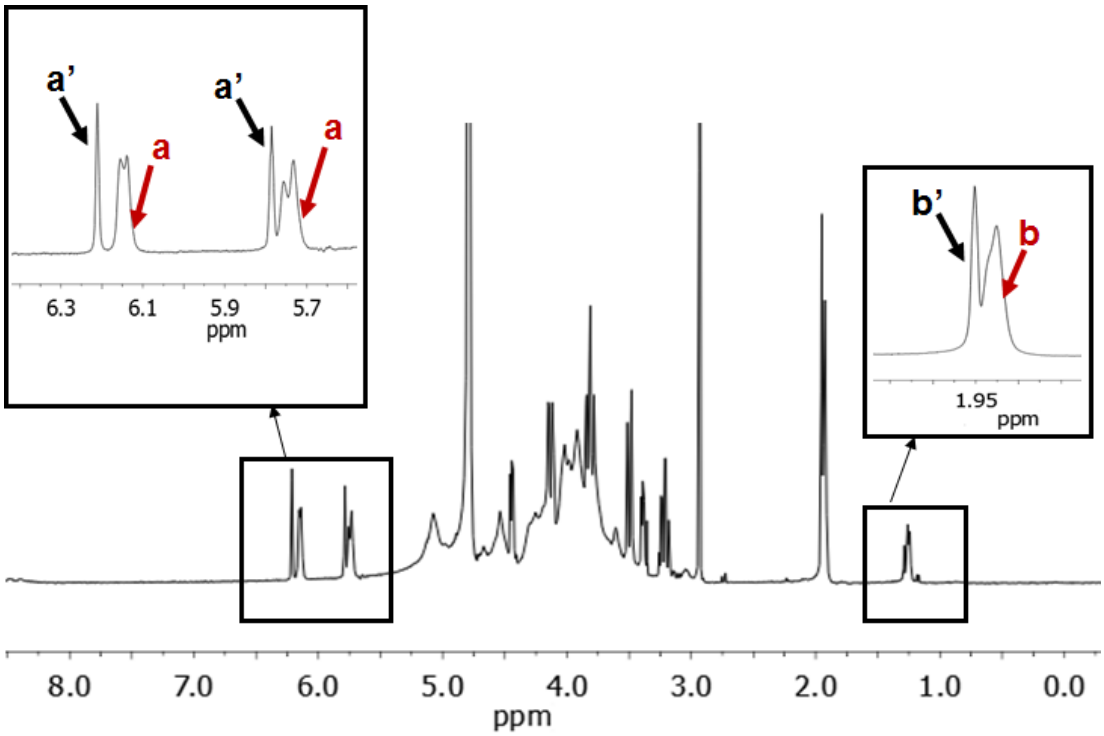


Fig. 3.3 ^{1}H NMR spectra in D_2O of methacrylated alginate obtained by using 2-chloro-4,6-dimethoxy-1,3,5-triazine (CDMT) as a coupling agent instead of carbodiimide chemistry. The final product showed impurities of unreacted AEMA (a' and b') represented by second peak for each methylene and methyl proton peak.

3.3.2 Photo-crosslinked alginate and the capability for additional modifications

The ability of methacrylated alginate to photo-crosslink in the presence of a suitable photoinitiator was verified by means of ^{1}H NMR spectra comparing samples of the UV initiator Irgacure 2959, methacrylated alginate mixed with Irgacure 2959 before (Figure 3.4B) and after UV irradiation for 20 minutes (Figure 3.4C). The integrals of the proton peaks for methylene and methyl groups reduce to values between 0 to 8% of their original intensity compared to the integrals before UV irradiation for all tested samples after 20 min UV irradiation (Figure 3.4C a) and b)). This reduction of the methylene peaks confirms that the double bonds must have reacted by crosslinking with each other.

Secondary modifications of the methacrylated alginate were demonstrated using the same amidation reaction by synthesising one compound after the other applying the same protocol as described in chapter 3.2.1. Multiple modifications allow to tailor the hydrogel properties for particular applications. The attachment of a molecule featuring functional groups could be demonstrated. These additional functional groups have shown bacteria-attachment-resistant properties [110]. The addition of such molecules for example, could promote an alginate based hydrogel with reduced contamination risk of bacteria. The successful attachment of AEMA as well as L-alanine benzyl ester is demonstrated in the ^{1}H NMR spectra in Figure 3.5B. L-alanine benzyl ester was chosen because it featured an amine group and reassembled the functional groups of the monomer benzyl methacrylate which was shown to reduce bacterial attachment when incorporated in polymer surfaces [110]. The subsequent photo-polymerization upon UV irradiation in the presence of Irgacure 2959 (Figure 3.5C) shows that additional modifications are feasible without compromising alginate's photo-reactivity. It has to be noted that this example was performed using the amidation reaction described in chapter 3.2.1.1 that displayed unreacted AEMA in the final product as well.

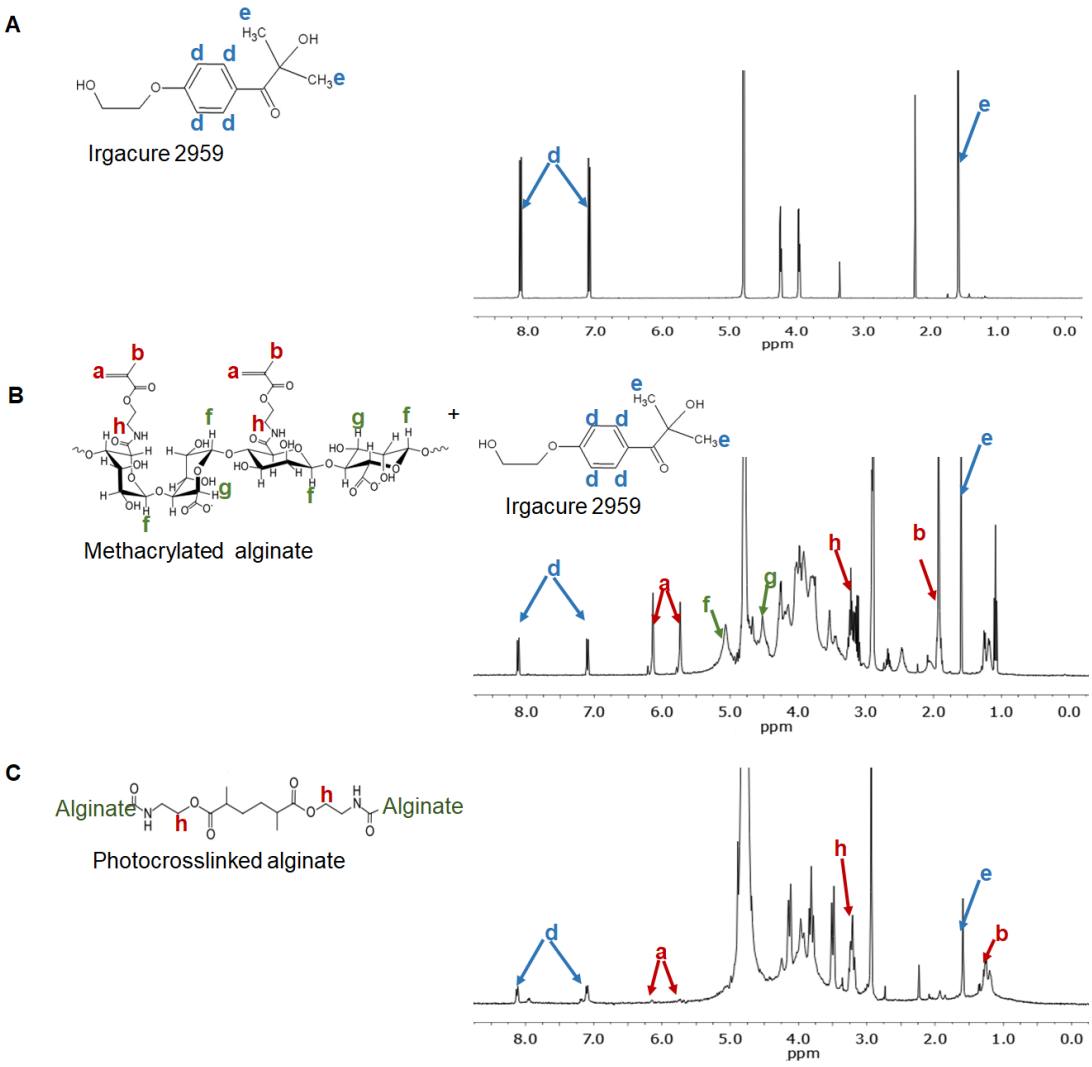


Fig. 3.4 ^{1}H NMR spectra in D_2O of A) Irgacure 2959, B) methacrylated alginate before and C) after UV irradiation for 20 min. The disappearance of the distinct methylene proton peaks a) after UV irradiation proves that the methylene groups reacted with each other.

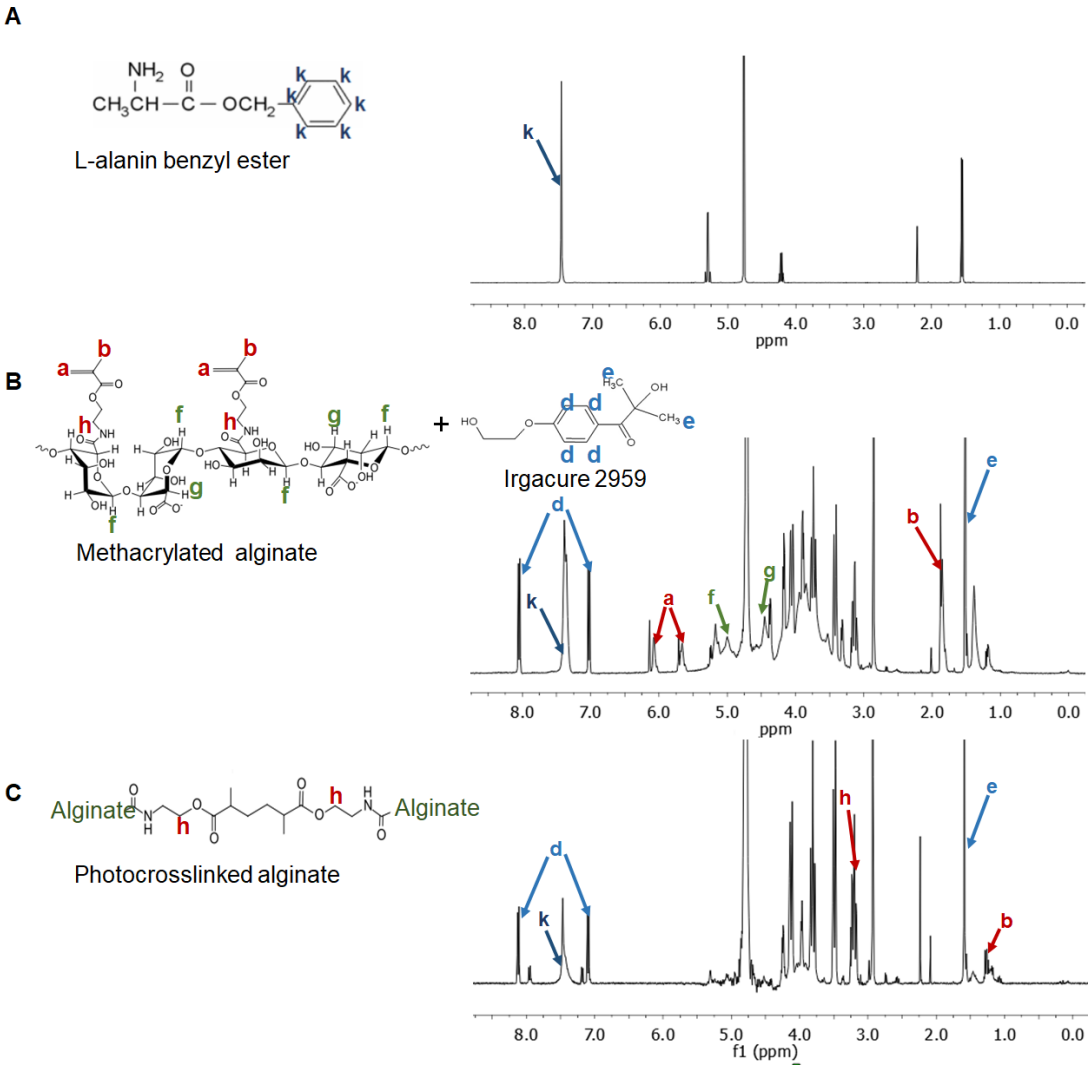


Fig. 3.5 ^{1}H NMR spectra in D_2O of A) L-alanine benzyl ester, B) alginate modified with 2-amino-ethyl methacrylate and L-alanine benzyl ester mixed with photoinitiator before and C)after UV irradiation for 20 minutes.

3.3.3 Determining the degree of functionalisation of methacrylated alginate

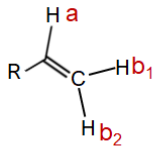
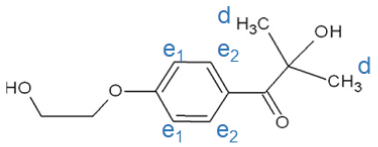
^{1}H NMR was used to determine the degree of substitution which is referred to as the actual methacrylation in the following. In theory, one option to calculate the degree of substitution would be to integrate distinct carbohydrate peaks from the alginate and derive the amount of attached AEMA by comparing their relative intensities to each other. Large and complex molecules such as alginate however, feature a lot of broad and overlapping peaks (Figure 3.2B) which makes the assignment of single peaks challenging. Moreover, the spectra of such complex molecules tend to slightly vary between different samples. The most distinct peaks for alginate (Figure 3.2B f) and g)) also overlapped with the proton peak of its solvent D_2O at δ4.79. Irgacure2959 was therefore used as a reference molecule to derive the amount of AEMA attached to alginate more accurately [100]. The proton peaks of Irgacure2959 at δ1.6, δ7.1 and δ8.1 (Figure 3.4B d) and e)) were used as a reference to determine the actual methacrylation summarized in Table 3.2.

Each sample of methacrylated alginate was mixed with 0.05 %w/v of Irgacure 2959 and dissolved in 700 μL of D_2O (n_{I2959} = 1.56*10^{-6} mol). By integrating the peaks for the photoinitiator relative to the methylene and methyl peaks of AEMA (Table 3.1), the ratio of Irgacure 2959 to AEMA can be determined. Knowing the exact amount of alginate in each NMR sample mixture (m = 7mg) and hence, its amount of carboxyl groups available for the reaction (0.036 mmol), it is possible to calculate the actual degree of methacrylation based on the AEMA to carboxyl group ratio:

$$Actual\ methacrylation = \frac{n_{AEMA}}{n_{COOH,Alg}} * 100$$

with n_{AEMA} = the amount of AEMA attached to the alginate and $n_{COOH,Alg}$ = the amount of COOH in alginate available for reaction.

Table 3.1 Integration of methylene and Irgacure 2959 peaks in ^{1}H NMR spectra collected for methacrylated alginate mixed with a known amount of the photoinitiator Irgacure2959, which served as a reference to determine the actual methacrylation of 25 %, 50 % and 75 % theoretical methacrylation of alginate.

	 Methacrylate group				 Irgacure 2959			
Theor. Methacrylation [%]	Proton	δ [ppm]	Integration area	Int(n)	Proton	δ [ppm]	Integration area	Int(n)
25	a	1.9	6.7	3H	d	1.6	3.14	6H
	b_1	5.7	2.23	1H	e_1	7.1	1	2H
	b_2	6.2	2.23	1H	e_2	8.1	1	2H
50	a	1.9	9.94	3H	d	1.6	3.23	6H
	b_1	5.7	3.65	1H	e_1	7.1	1	2H
	b_2	6.2	3.64	1H	e_2	8.1	1	2H
75	a	1.9	13.56	3H	d	1.6	3.28	6H
	b_1	5.7	4.72	1H	e_1	7.1	1	2H
	b_2	6.2	4.72	1H	e_2	8.1	1	2H

The actual methacrylation and the derived methacrylation efficiencies for three different theoretical methacrylations of 25 %, 50 % and 75 % are summarized in Table 3.2. The methacrylation efficiency is determined as the ratio of the actual methacrylation to the theoretical methacrylation of alginate (Chapter 3.2.2).

Table 3.2 Actual methacrylation and methacrylation efficiency calculated from the integral ratio of Iegacure 2959 protons and the methacrylate protons.

Theoretical Methacrylation [%]	Actual Methacrylation [%]	Methacrylation efficiency [%]
25	18.4	73.6
50	30.2	60.4
75	40.4	53.9

3.3.4 Gel permeation chromatography

A relative change in the molecular weight of 50 % and 75 % theoretically methacrylated alginate was demonstrated in comparison to the unmodified alginate. The absolute molecular weights could not be determined due to the nature of the experimental set-up. The standard polymer poly(ethylene glycol) (PEG) used for calibration significantly differs in size and structure from alginate so that the values obtained for the number-average molar mass (M_n) could only be evaluated qualitatively. The dispersity Đ , describing the distribution of the molecular mass in a given polymer sample, increases from 1.7 for unmodified alginate up to 2.0 for 75 % theoretically methacrylated alginate. These values of Đ for sodium alginate are in good agreement with the literature [111]. The retention time for 50 % theoretically methacrylated alginate-AEMA was longer relative to the unmodified alginate (Figure 3.6). The retention time depends on the hydrodynamic volume of the polymer which is affected by the polymer size with larger polymers experiencing smaller retention times. Accordingly, the 75 % alginate-AEMA showed an even shorter retention time which indicates a hydrodynamic volume (and hence larger M_n) compared to lower methacrylation degrees. In combination with

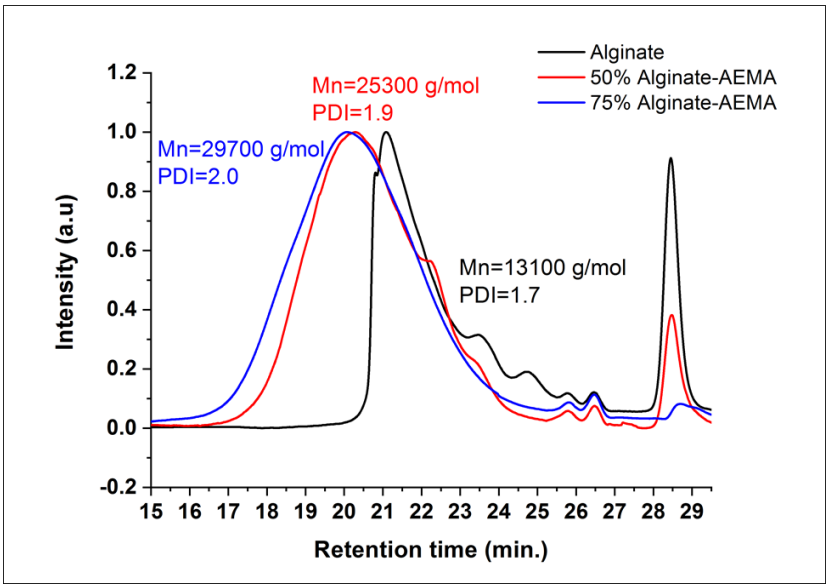


Fig. 3.6 Gel permeation chromatography(GPC) of pure alginate and methacrylated alginate with a theoretical methacrylation degree of 50 % and 75 % (Table 3.2).

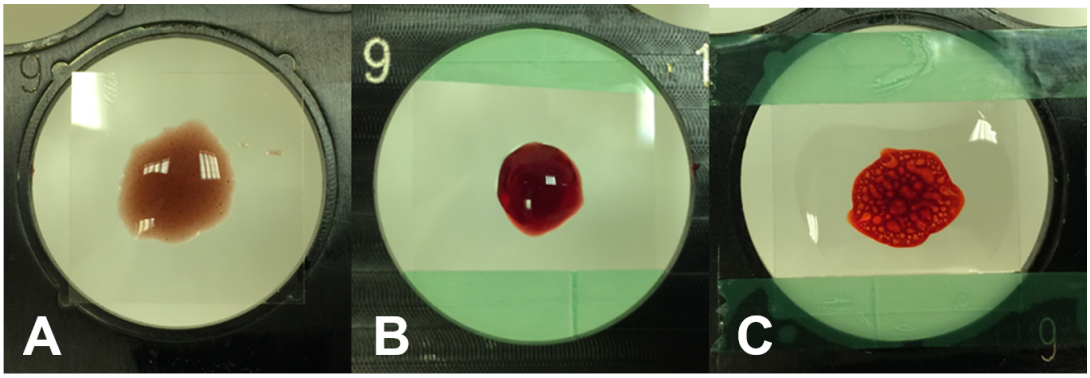
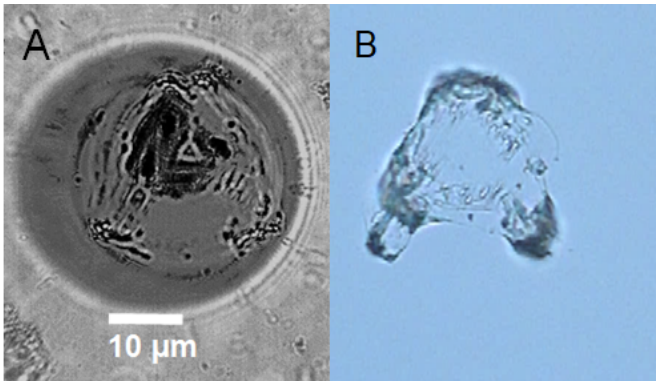


Fig. 3.7 Photoresist composed of methacrylated alginate, water-soluble 2PP optimized photoinitiator P2CK and water. A) Photoresist droplet with precipitated P2CK which lead to poor 2PP; B) Photoresist with fully dissolved P2CK because of neutral to slightly basic pH that facilitates better photoinitiator solubility and enables good 2PP; C) Photoresist droplet that dried out within 45 min when not sealed in a closed chamber.

the ^{1}H NMR spectra above, the relative shifts of the molecular weights prove that the alginate has been successfully modified with control of the degree of substitution.

3.3.5 Two-photon polymerization of methacrylated alginate

The first 2PP experiments discussed in this chapter serve as a proof of principle that a photoresist composed of methacrylated alginate mixed with P2CK can be efficiently polymerized using 2PP. The photoinitiator P2CK features a deep brown-red colour and discolours a photoresist solution by employing only little amounts such as 0.5 %w/v as shown in Figure 3.7B. When dissolving the methacrylated alginate in ddH_2O and adding P2CK, the photoinitiator can precipitate from the solution as shown in Figure 3.7A. The 2PP of such a photoresist is highly inefficient allowing polymerization only in combination with extensive heat formation causing observable micro-explosions during the printing process (Figure 3.8A). This is due to the fact that the photoinitiator can not participate in the reaction if it is not dissolved as the monomer. This problem could be addressed by adjusting the slightly acidic pH of the solution to a neutral to slightly basic pH between pH = 7-8 (Figure 3.7 B). A challenge all water based photoresists share is that they dry out over time (Figure 3.7C), limiting the time within the polymerization



.

Fig. 3.8 2PP of 2 % methacrylated alginate with 0.5 w% of the photoinitiator P2CK that precipitated in solution. A) Image recorded from life camera integrated into the *nanoscribe* system during 2PP, 63x magnification. B) Bright-field images of polymerized structures attached to glass substrate after removal of non-polymerized material.

can be performed. This is especially important for 2PP due to the small volumes used that dry rapidly. Thus, minimizing printing times by using photoresists with highly efficient 2PP kinetics is particularly pressing to avoid sample dehydration. Depending on the complexity and dimensions of the microstructure of interest, additional sample modifications such as enclosing the photoresist in a closed chamber, may be applied to reduce water evaporation (see chapter 5).

In Figure 3.9, an example structure of 2PP alginate hydrogel is presented that accurately renders the CAD design (Figure 3.9 A). In comparison to Figure 3.8, the letter 'A' could be printed and was imaged using bright-field microscopy. Building on this initial results, methacrylated alginate could represent a promising alternative to currently used biomaterials for the 2PP of hydrogels.

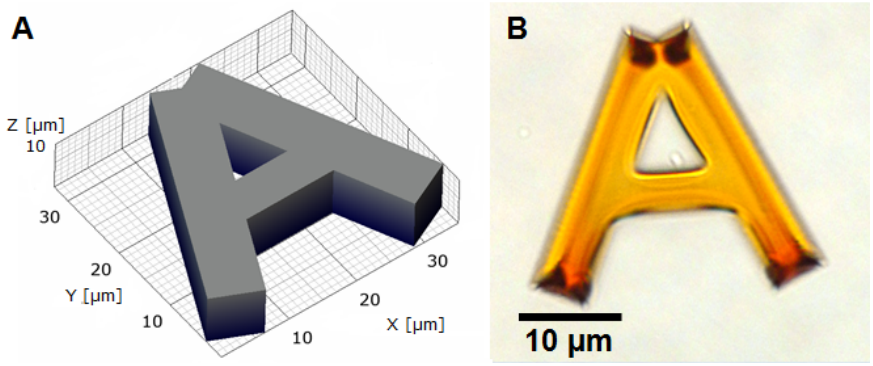


Fig. 3.9 Example structure of successfully two-photon polymerized alginate hydrogel. A) CAD design of the letter 'A'. B) Bright-field microscope image of 2PP alginate hydrogel accurately rendering the CAD design.

3.4 Conclusions

- This work introduces a novel photoresist for 2PP of hydrogels composed of methacrylated alginate, water and the photoinitiator P2CK.
- Two different chemistries were evaluated to obtain methacrylated alginate by means of attaching AEMA molecules to alginate via peptide bond formation. The here described carbodiimide based chemistry resulted in a more pure product compared to the use of the coupling agent CDMT.
- Additional functional groups could be attached to the methacrylated alginate without compromising its photo-sensitivity. Additional modifications could allow to modulate the hydrogel properties according to the application.
- On the basis of ^{1}H NMR spectra and GPC, the modification of alginate could be verified and the actual degree of functionalisation could be determined by using the commercial photoinitiator *Irgacure 2959* as a reference.
- A 2PP hydrogel structure could be fabricated on the basis of the alginate photoresist that accurately rendered the shape of the CAD design in form of the letter 'A'.

Chapter 4

Two-photon polymerization of alginate hydrogels

4.1 Introduction

This work is building on the development of a new 2PP photoresist based on methacrylated alginate, water and P2CK introduced in chapter 3. This chapter introduces a set of experimental methods to elucidate the 2PP kinetics and properties of alginate hydrogels by studying indicators directly related to the polymerization kinetics. These indirect assessments allow to draw conclusions about the 2PP kinetics and the formed polymer network.

2PP kinetics are generally challenging to study due to microscopic reaction volumes and usually fast reaction times [61]. A common strategy is to apply ultraviolet (UV) polymerization to polymerize a similar photoresist as used for 2PP and study its polymerization kinetics or hydrogel properties instead [112][67][85]. Viscoelastic properties using rheology and the swellability determining weight increase of 'swollen' gels are for example, commonly applied techniques to study the properties of UV polymerized hydrogels and are often presumed to be similar for 2PP hydrogels for simplification [113][62]. UV polymerization and 2PP however, differ substantially in the reaction volume. UV

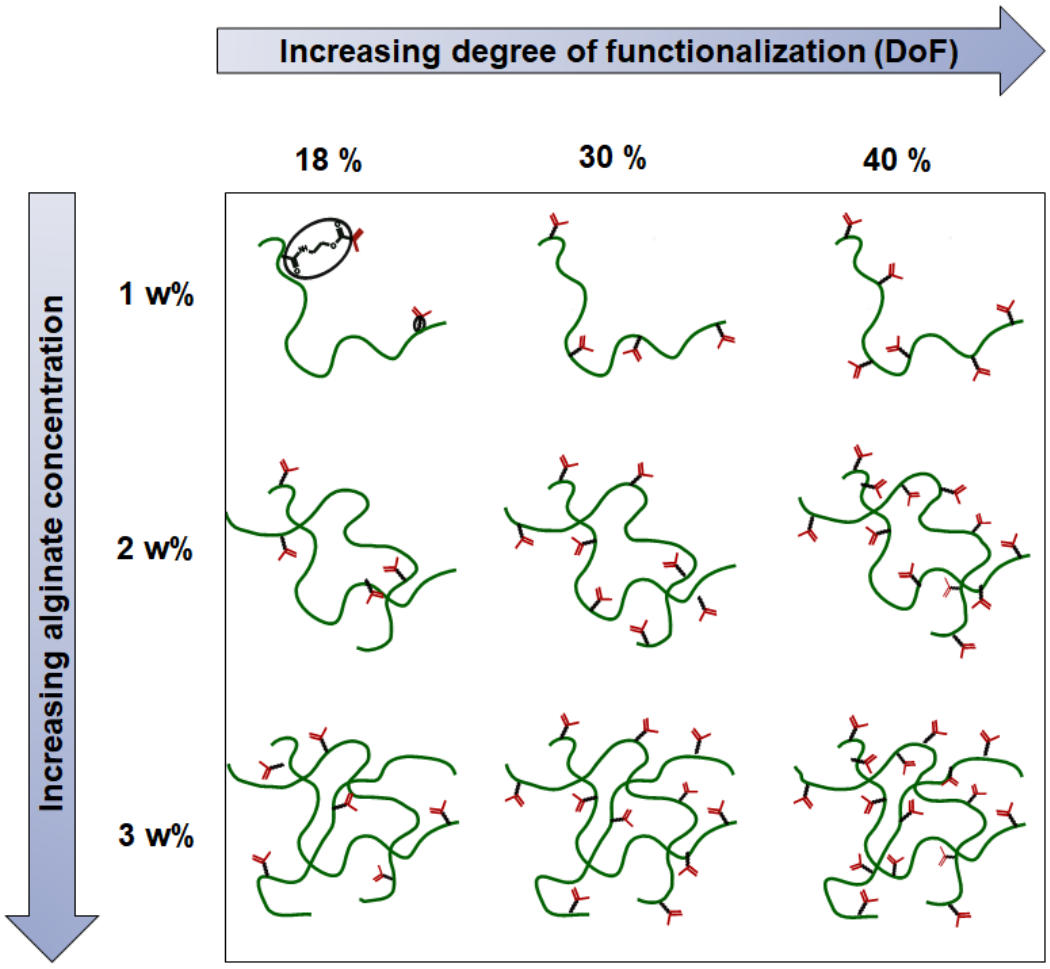


Fig. 4.1 Schematic of increasing Degrees of Functionalisation (DoF) of alginate against increasing alginate concentrations.

polymerization is occurring throughout the entire volume of the irradiation whereas 2PP only occurs very localized at the focal point of the laser. This has to be taken into account considering oxygen quenching, diffusion dependent reaction steps and the amount of reactive molecules present in a very small volume. The resulting crosslinked polymer network will therefore be very different comparing UV polymerized and 2PP hydrogels. Another major difference is often the photoinitiator used for UV and 2PP photoresists which has to be sensitive to the particular light source applied, namely UV or near infrared (NIR) light. Cytocompatibility tests with UV polymerized hydrogels instead of 2PP are not conclusive because the photoinitiator is often the most toxic element. It is therefore, not valid to assume the same cytocompatibility when changing

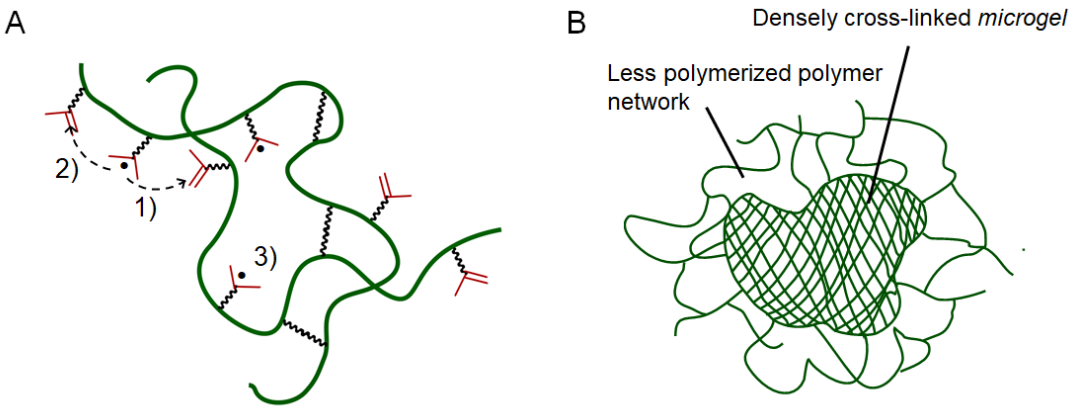


Fig. 4.2 Schematic of possible crosslinking mechanisms of methacrylated alginate. A) The radical end of a polymer chain can attack another alginate molecule 1). The radical end of a polymer chain can react with one of its own pendant double bonds 2). In a densely crosslinked network, a few of the radicals will be trapped and not be available for reaction 3). B) Microgels can form when the radicals are mainly reacting with double bonds of the same molecule promoting loop formation and densely crosslinked microgels.

the photoinitiator, even in an otherwise identical photoresist. On the basis of a number of indirect measurements described in detail throughout the chapter, this research systematically studies two main factors influencing the 2PP kinetics. Factor one is the degree of functionalization (DoF), i.e. the number of methacrylate groups attached to alginate, and factor two is the alginate concentration (Figure 4.1).

Factor 1: functional groups. Large biopolymers such as BSA (MW = 66 kDa) and methacrylated alginate (MW $\leq$ 75 kDa) with multiple functional groups distributed throughout the monomer exhibit more complex polymerization kinetics than linear free radical chain reaction introduced in Chapter 3.1. The fundamental reaction steps including initiation, propagation and termination also apply for crosslinking polymerization systems as methacrylated alginate. The monomer multifunctionality however, leads to significant differences in the network formation kinetics. The methacrylated alginate studied here in particular, is a very large molecule with crosslinking functional groups widespread throughout the molecule. After radical formation during the initiation step,

one of the available double bonds of the alginate reacts and will be incorporated into the polymer chain whereupon several unreacted double bonds remain on the same alginate molecule (Figure 4.2). Crosslinking of macromolecules with several vinyl groups has been studied since the early 20th century already [114]. Thereafter, characteristic crosslinking properties were often observed distinguishing between intramolecular and intermolecular crosslinking that was described for molecules featuring several double bonds [115]. Accordingly, the radical end of the polymer can react in mainly two distinct ways promoting different network formations:

1. **Intermolecular crosslinking:**

   Attacking a double bond from another molecule connecting a network out of individual alginate molecules (Figure 4.2 A.1))

2. **Intramolecular crosslinking:**

   Reacting with the pendant double bonds on the same molecule forming loop formation which could promote more densely crosslinked polymer networks in a small area referred to as microgel formation (Figure 4.2 A.2), Figure 4.2 B)

The formation of microgels, schematically illustrated in Figure 4.2 B), would result in network inhomogeneity and could lead to reduced mechanical strength of the polymer network when compared with a homogeneous network [53].
The number of functional groups on the alginate is crucial because it determines the maximum amount of crosslinks possible and influences the polymerization kinetics. Especially the initiation and propagation will be affected since they are driven by the amount of reactive species, namely the vinyl groups, available.

Factor 2: concentration. Generally, crosslinking systems feature degrees of conversion considerably below 100 % due to steric effects causing a reduction in the mobility of radicals and functional groups during the polymerization. A certain amount of radicals and photoinitiator molecules is therefore likely to be trapped within the network (Figure 4.2A, 3)) [53]. The alginate concentration is crucial because it affects the mobility of the molecules in solution and the viscosity which affects all diffusion sensitive steps, particularly the termination step [116].

One objective was to identify the optimal photoresist composition and the optimal laser energy dose for efficient 2PP of hydrogels. The formation of radicals and subsequent polymerization were controlled and assessed with the energy dose adjusted using both, the laser power and laser scan velocity. Another objective was to study the effect of increasing alginate concentrations and number of functional groups on the polymerization kinetics and hydrogel properties to inform the development of future photoresist compositions for 2PP of hydrogels. The viscosity of micro-volumes of photoresist was measured with a novel high-throughput method [92], and correlated with polymerization threshold powers. Cryogenic SEM was used to visualize the hydrated 3D structures with sub-micron resolution.

4.2 Experimental methods

4.2.1 Two-photon polymerization

4.2.1.1 Polymerization- and damage- threshold power and dynamic power range

The polymerization and damage threshold powers P_{th} and D_{th} of photoresists serve here as an indirect measure for the affect of varying photoresist compositions on the polymerization kinetics. The polymerization threshold P_{th} was defined as the laser power (LP) when polymerized material could be observed, often in the form of macroscopic clusters rather than fully polymerized structures due to poor mechanical stability and shrinkage at threshold energies. The damage threshold D_{th} was defined as the minimum LP causing visible effects of extensive heat formation during the 2PP process leading to micro-explosions that become evident in damaged 'cube' structures. P_{th} and D_{th} were determined for three different degrees of functionalisation for alginate with methacrylate groups (18%, 30% and 40%) as well as three varying monomer concentrations (1-3% w/v in ddH_2O), as shown in Figure 4.1. The photoresist was mixed with the corresponding weight percent of methacrylated alginate and 3 mol% of P2CK relative to the amount of double bonds present in the alginate (Chapter 1.3.2). A cube with the dimensions 4μm x 4μm x 3μm served as the test structure to assess the threshold behavior. Starting at a LP of 4 mW and with 2 mW increments up to 40 mW, the maximum LP that could be achieved with the commercial 2PP set-up (Photonic professional, nanoscribe) used. To ensure the correct assignment of the LP used, each cube was printed with a text below stating the percentage of the maximum LP applied (10% to 100% laser power with 5% increments). Scan speeds were varied from 7.5 mm/s up to 30 mm/s with 2.5 mm/s increments as shown in Figure 4.5. For clarity, only 10 mm/s, 20mm/s and 30 mm/s are presented in the graphs since there was little difference between 2.5 mm/s increments. Due to spatial fluctuations of sample inhomogeneities, the values were statistically obtained from three repeats. All prints

were imaged with a confocal laser scanning microscope to visualise the autofluorescent two-photon fabricated structures and assess the polymerization- as well as the damage threshold of each photoresist.

The dynamic power range (DPR) represents the polymerization window which can be derived from the threshold values P_{th} and D_{th} and is defined as:

$$DPR = \frac{D_{th}}{P_{th}} \tag{4.1}$$

Higher DPR values are desirable translating to a wider processing window (Chapter 4.2.1.2) which ensures more reproducible results by buffering natural fluctuations in photoresist compositions [117][118].

4.2.1.2 Processing window

The processing window is here defined as the range of laser power and laser scan speed combinations that enable the microfabrication of stable 3D microstructures for a given photoresist. The processing window lies within the polymerization- and damage threshold determined for a photoresist (Chapter 4.2.1.1) but is commonly smaller because the powers close to the threshold values often do not yield a complete 3D structure. To determine the polymerization window of the novel photoresist, an array of a 3D microstructure with different laser powers and laser scan speeds were printed. The structure quality was assessed visually using a bright field microscope by classifying the quality into four categories and translated into a colour code:

1. No sufficient polymerization (white)
2. No complete structure (yellow)
3. Complete structure (green)
4. Overexposure (red)

Thereby, a processing window provides a clearly arranged overview of optimal laser powers and scan speeds for a given photoresist which can be used for evaluation of photoresist performance [107].

4.2.1.3 Deformation ratio of 2PP alginate hydrogels

The deformation ratio D of the hydrogels served as an indirect measure for the relative crosslink density of the hydrogel structures. This approach is based on the assumption that higher crosslink densities lead to hydrogel structures with higher structural integrity. Hydrogel structures with high structural integrity on the other hand, resemble the CAD design more closely because the polymerized structure suffers less from any deformation after development.

Hydrogel cubes (50 μm^3) were used to determine the deformation ratio of different photoresist compositions. The hatching and slicing distances (Slicing distance = 0.2 μm, Hatching distance = 0.1 μm) for all cubes as well as the LP and SS were kept the same in order to solely compare the degree of deformation in relation to the photoresist composition. The 3D hydrogel structures were assessed using confocal laser scanning microscopy visualizing the 3D shape of hydrated hydrogels. For quantitative analysis, the perimeter of the bottom (part of the structure that is attached to the glass substrate) (P_b) and the top of the structure (P_t) were measured using the ImageJ (FIJI) software and applied to calculate the deformation ratio D that is defined as:

$$D = \frac{P_t - P_b}{P_t} \times 100 \tag{4.2}$$

4.2.1.4 Minimal linewidth

The minimal linewidth achievable for a given photoresist depends on a lot of factors starting with the 2PP set-up such as the laser and the optics involved. In this work, the commercial nanoscribe system was used for all experiments limiting any changes

to the laser radiation. These are fixed to commonly used laser parameters applied for 2PP based on a pulsed femto-second laser (pulse duration $\approx$ 100 fs) with a repetition rate of 80 MHz and a center wavelength λ = 780 nm. In order to enable small feature sizes, mainly high-numerical aperture (NA) objectives are used to focus the light as much as possible, thus minimizing the focal volume of the laser beam that causes the excitation of the photoinitiator. The linewidth experiments were performed using the highest resolution objective available in the laboratory, the plan-apochromat objective (63x, NA = 1.4, Zeiss).

The photoresist including the photoinitiator also play a major role as the polymerization reaction itself dictates the polymerized volume determined by the polymerization steps discussed in chapter 3.1. Due to the polymerization characteristics of a photoresist, linewidths smaller than the diffraction limit of the light source used are possible. A polymerized structure can only be observed after development if the threshold value of radicals were initiated to polymerize the photoresist. As discussed in chapter 4.2.1.1, structures are often incomplete at the polymerization thresholds because the laser intensity was only sufficient at the focal point of the laser but not the periphery so that not the entire volume irradiated by the laser beam will be polymerized. This results in loosely polymerized resist adjacent to the focal point of the laser which can get washed away in the development step. Figure 4.3 illustrates this phenomenon by means of a Gaussian profile representing the light intensity in the central disk of a diffraction pattern created by a circular aperture. This example depicts a polymerization threshold at 75% of the intensity [119]. The corresponding linewidth of the polymerized structure is illustrated as the area above the threshold.

Minimal linewidths were determined by printing ladders with a fixed scan speed (500 μm/s) but increasing laser powers with each ladder step (Figure 4.4). Varying concentrations of Alg-MA30 with 3 mol% of P2CK in water were tested. The linewidth was then measured using the ImageJ software for scanning electron micrographs of the ladders and averaged for two repeats each.

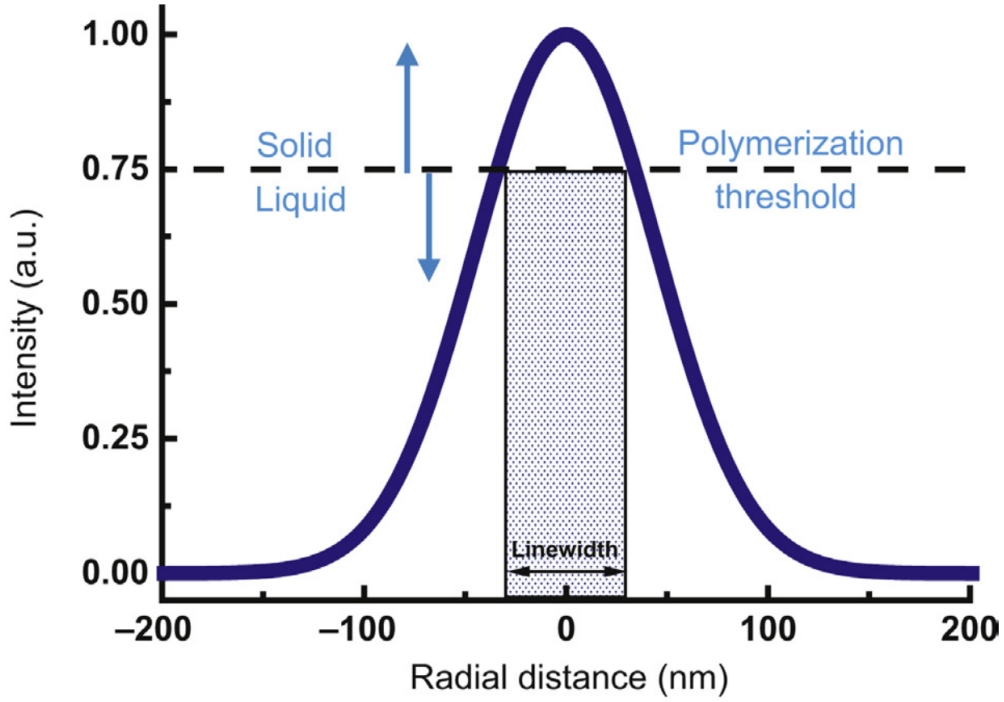


Fig. 4.3 Gaussian profile representing the light intensity in the central disk of a diffraction pattern created by a circular aperture. The polymerization threshold is located at 75% of the intensity.The corresponding linewidth of the polymerized structure is illustrated as the area above the threshold (dotted rectangle). Figure adapted from Miguel *et al.* [119].

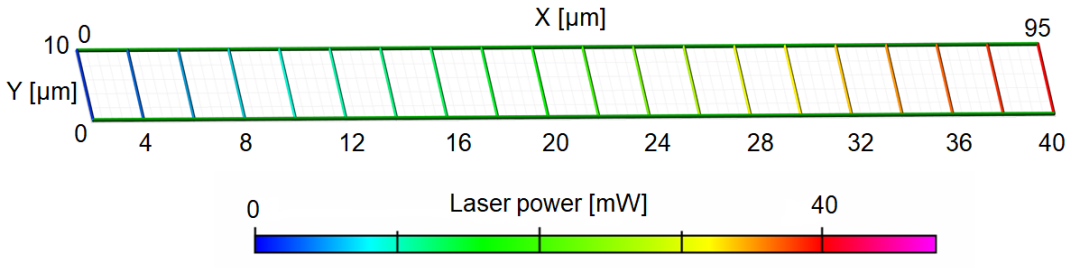


Fig. 4.4 Laser path simulation of ladder structure to determine the minimal linewidth in relation to the laser power applied.

4.3 Results and discussion

4.3.1 2PP of methacrylated alginate hydrogels

In this section, optimal printing parameters were identified that enabled efficient 2PP of hydrogel structures featuring high structural integrities. Additional experiments were performed to probe the 2PP kinetics on the basis of varying degrees of functionalisation (DoF) of alginate as well as different alginate concentrations as listed below:

- Polymerization and damage threshold powers P_{th} and D_{th} and the dynamic power range (DPR) were determined.
- Photoresist viscosities were measured for different photoresist compositions.
- Processing windows were established indicating optimal laser powers and laser scan speeds to print hydrogels with high structural integrity for a given photoresist.
- Minimal line widths were identified to determine minimum feature sizes possible for alginate hydrogels using 2PP.
- The deformation of 3D hydrogel structures was examined in relation to the DoF of alginate versus the alginate concentration on the structural integrity.

4.3.1.1 Viscosities of methacrylated alginate

The viscosities were measured with a novel high-throughput viscometer utilizing a liquid handler which enabled reproducible measurements of micro-volumes [92]. The average values and their standard deviations are summarized in Table 4.1. The results for all three measurements are depicted in Table A.1 (Appendix 1). The viscosities of the methacrylated alginate samples increased by 65% to 80% when increasing the concentration from 1% w/v to 2% w/v. From 2% w/v to 3% w/v, a viscosity increase by 85% to 95% was observed.

All polymerization steps are diffusion dependent, which in turn depends on the viscosity

of the photoresist. Therefore, the large differences in viscosity between the different alginate concentrations need to be considered for the investigation of the 2PP kinetics of methacrylated alginate in the following Chapter 4.3.1.2.

Table 4.1 Viscosities of various alginate concentrations and DoF of alginate with methacrylate groups.

	Viscositiy [mPa·s] at 25°C		
Concentrations	**Alg-MA18**	**Alg-MA30**	**Alg-MA40**
1% w/v	**5.79** (±0.15)	**6.48** (±0.23)	**6.83** (±0.16)
2% w/v	**10.50** (±0.05)	**10.64** (±0.05)	**11.82** (±0.20)
3% w/v	**16.50** (±0.12)	**20.74** (±0.14)	**21.93** (±0.14)

4.3.1.2 Polymerization- and damage- thresholds

As described in chapter 4.2.1.1, the polymerization- and damage threshold powers, P_{th} and D_{th}, can be determined through an energy dose array as illustrated in Figure 4.5 meaning an array of increasing laser powers against increasing laser scan speeds. This method is fast and effective and allows to screen many photoresists to compare their polymerization characteristics with each other [77] Figure 4.5A and B show the CAD file for such an array. A cube with the dimensions 4μm x 4μm x 3μm served as the test structure to assess the threshold behavior. To ensure the correct assignment of the LP used, each cube was printed with a text below stating the percentage of the maximum LP applied (10% to 100% LP with 5% increments). Figure 4.5C illustrates a fluorescent image of such an array with close-ups of the four different classifications that the cube structures were categorised as.

Figure 4.6 compares the the P_{th} and the D_{th} plotted against increasing alginate concentrations of three different writing speeds for 10 mm/s, 20 mm/s and 30 mm/s, respectively. Photoresists composed of Alg-MA18, Alg-MA30 and Alg-MA40 were compared directly with each other. Three different concentrations were tested for each

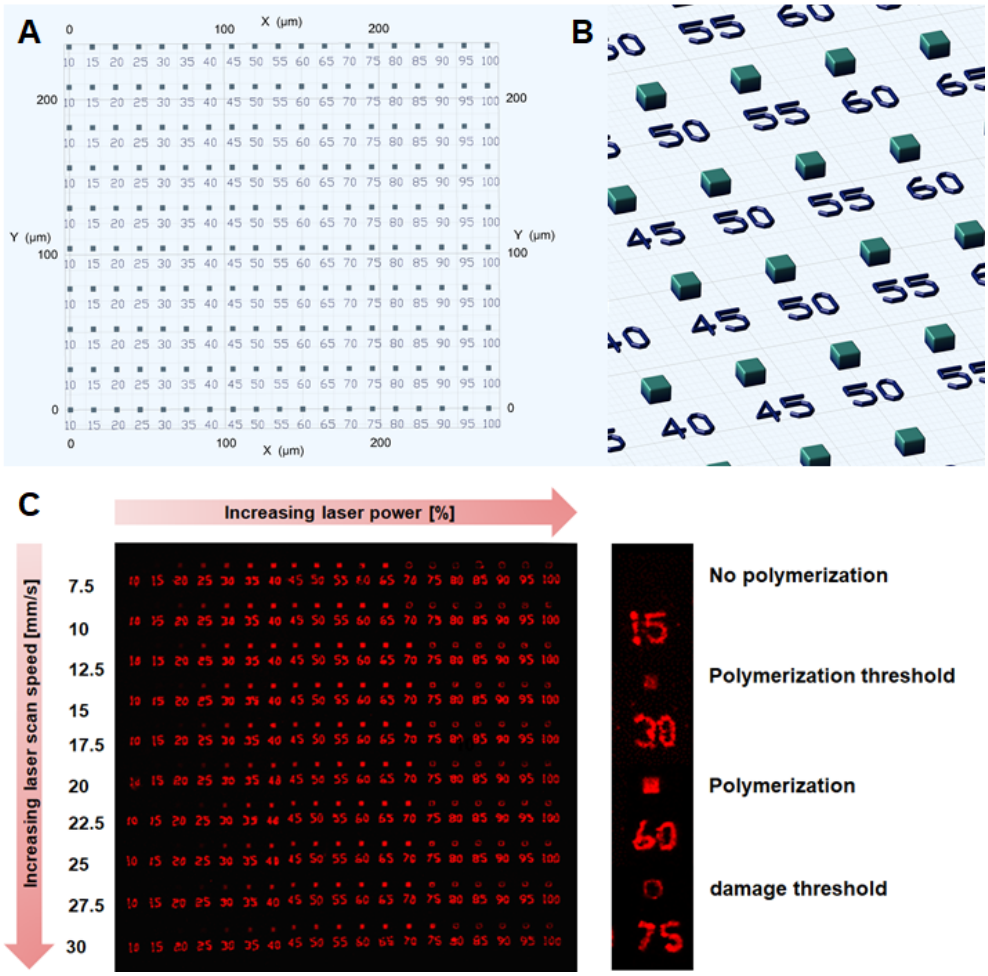


Fig. 4.5 Method of determining polymerization- and damage- threshold powers for a photoresist. A) Top view of CAD design for energy dose array. B) Enlarged 3D view of CAD design of individual structures of energy dose array. C) Confocal image of polymerization and damage thresholds in relation to the laser power and laser scan speed.

DoF of alginate.

Increasing laser speeds generally raised the P_{th} and the D_{th} of all samples. The threshold values increased by 1 to 3 mW for each scan speed step of 10 mm/s between 10 mm/s and 30 mm/s. The exposure time is inversely proportional to the laser scan speed which means that the higher the scan speed the lower the exposure time which in turn reduces the energy dose per area. Hence, higher laser powers were required to reach the threshold of the minimum energy dose and to initiate polymerization when applying higher can speeds.

Overall, Alg-MA40 based photoresists exhibited the lowest P_{th} and the highest D_{th} values resulting in the largest dynamic power ranges for all tested methacrylation degrees (Figure 4.7). With increasing alginate concentrations both P_{th} and D_{th}, decreased for Alg-MA40. This effect of lowered threshold values due to increased concentrations was less pronounced for Alg-MA30 and was not observed for Alg-MA18. The mobility of the alginate molecules in a more concentrated, more viscous, photoresist (Table 1.1) may impede the propagation of free radicals and subsequently reduce the number of crosslinks formed per photon. This would reduce the polymerization efficiency reflected in the P_{th}. The higher density of functional groups present in Alg-MA40 however, provided more double bonds that were already in proximity to the radical so that efficient crosslinking would still possible despite being sterically hindered.

Mueller and co-workers showed experimentally that oxygen quenching is the dominant termination reaction in 2PP [61] which is strongly diffusion dependent. High viscosity resists could therefore, slow the termination reaction down by means of oxygen quenching which could explain the lower polymerization threshold powers P_{th} for Alg-MA40 and Alg-MA30 with increasing alginate concentrations. The oxygen quenching competes with the initiation of radicals that are generated during the illumination. With increasing viscosities, the retarded oxygen diffusion may favour the initiation of more radicals, thereby reducing the polymerization threshold power. The observed polymerization reaction is always an interaction of all reaction steps, that are broken down into

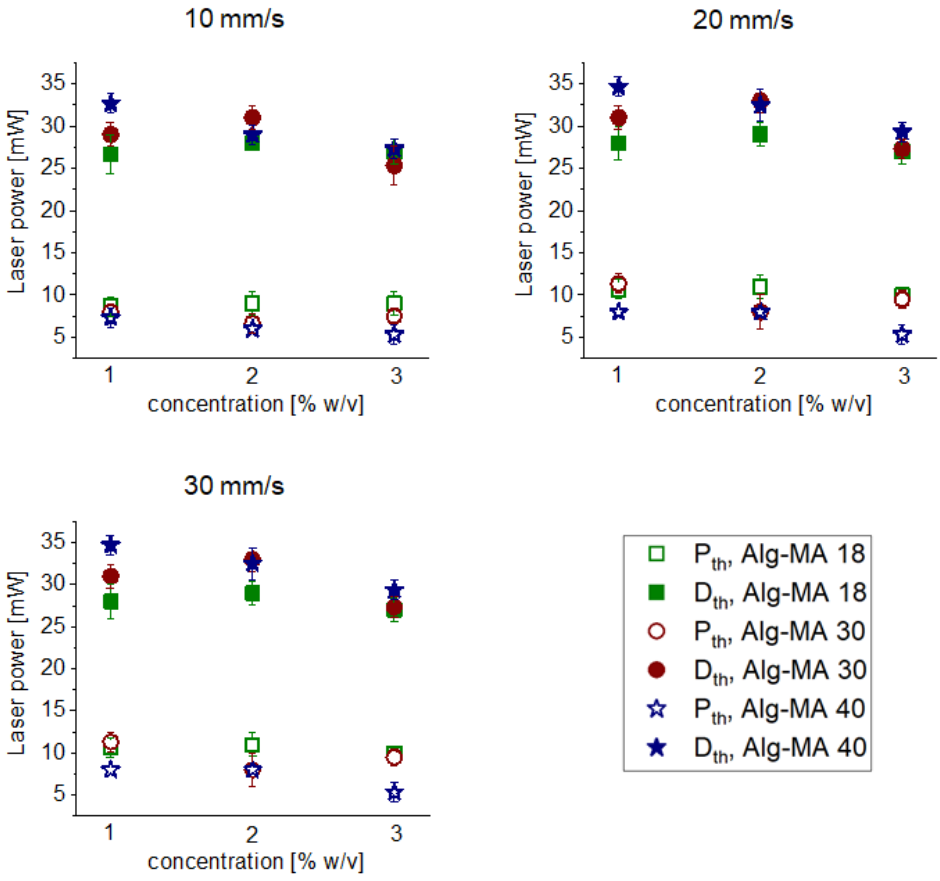


Fig. 4.6 Polymerization- and damage- threshold powers for varying degrees of functionalisation (DoF) of methacrylated alginate as a function of different alginate concentrations for different laser scan speeds: A)10 mm/s B) 20 mm/s and C) 30 mm/s. The data points represent the mean ± standard deviation (n = 3).

simplified initiation, propagation and termination reaction.

The results presented in Figure 4.6 indicate that increasing DoF's decrease the P_{th} and raised the D_{th} values generally. Lower P_{th}s could be explained by more reactive groups available for reaction, therefore promoting more crosslinking events and requiring less energy to initiate the reaction. Concurrently, higher DoFs possibly promote crosslinking reactions that defer unwanted reactions such as photo-ionization that could be responsible for the damage, observable as extensive heat formation and subsequent micro-explosions [60].

It has to be noted that the results presented in this work served as a preliminary insight of how the DoF and the alginate concentration as well as the associated viscosity affect the polymerization kinetics. For conclusive results, these experiments have to be performed on a statistical basis with multiple more repeats. Additional experiments that investigate the influence of viscosity without changing the alginate concentration could elucidate the influence of these factors further as the here discussed results can not distinct between the effect of the increased concentration and the viscosity.

4.3.1.3 Dynamic power range

The dynamic power range (DPR) is directly derived from the ratio of D_{th} to P_{th} and represents the range of laser powers in which polymerization can be observed. It is generally favourable for a photoresist to feature a high dynamic power range ensuring reproducibility by buffering natural fluctuations in photoresist compositions [118]. This is especially the case for biopolymers which show more variations in monomer structure, size and amount of functional groups than synthetic polymers. A wide dynamic power range can therefore, buffer natural inconsistencies and ensure good printing quality. The laser scan speed does not significantly affect the dynamic power range (Figure 4.7), confirming that both P_{th} and D_{th} increased by a comparable average value as discussed above. Alg-MA18 was relatively unaffected by the alginate concentration whereas the

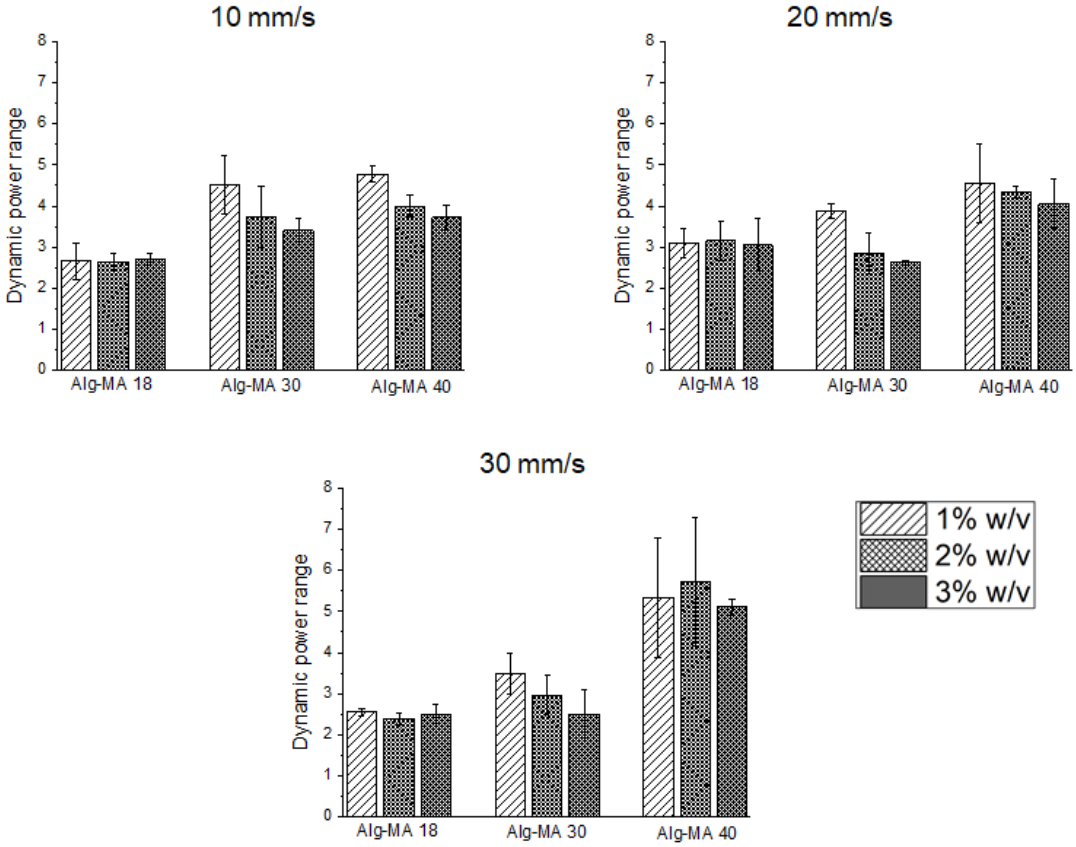


Fig. 4.7 Dynamic power ranges (DPR) for varying degrees of functionalization of methacrylated alginate and different concentrations for differnet laser scan speeds: A) 10 mm/s B) 20 mm/s and C) 30 mm/s. The data points represent the mean ± standard deviation (n = 3).

Alg-MA30 and Alg-MA 40 resulted in smaller dynamic power ranges with increasing alginate concentrations (Figure 4.7).

4.3.1.4 Processing window for alginate hydrogels

The 2PP processing window for novel photoresists was realised by printing arrays of 3D hydrogel structures. This can be effectively represented in processing window diagrams as shown in Figure 4.8. By means of bright-field microscopy, different categories of structure quality were established (Chapter 4.2.1.2). A wide range of possible combinations that facilitate robust 3D structures (Figure 4.8, green) are desirable.

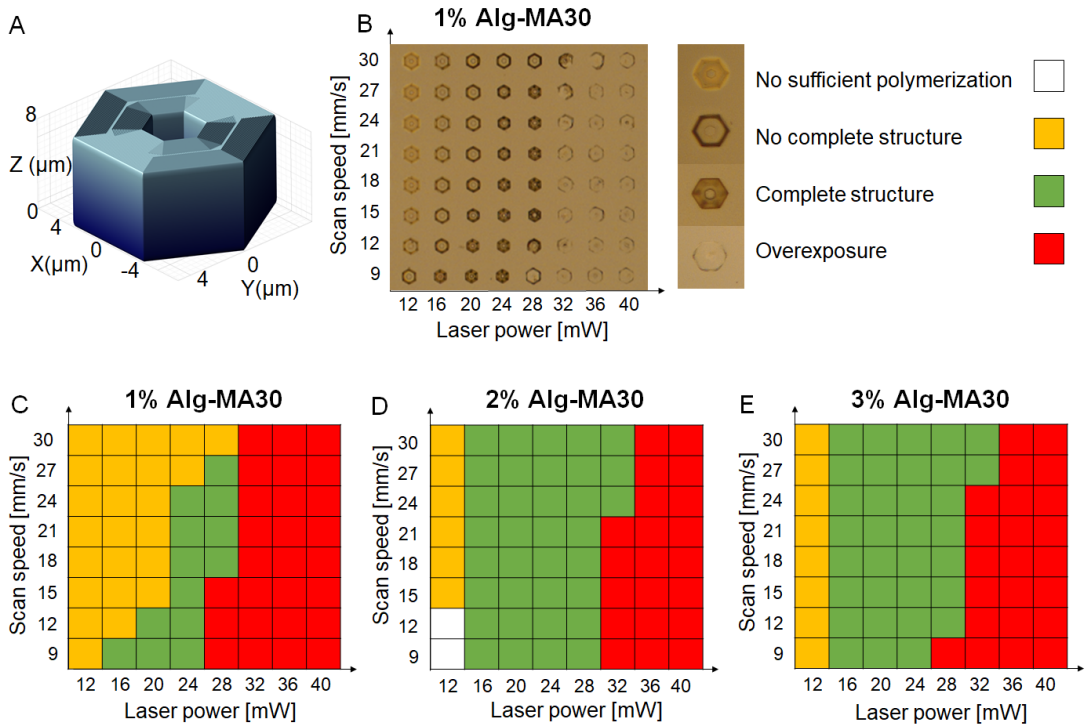


Fig. 4.8 Processing windows for three different concentrations of Alg-MA30. A) CAD design of individual 3D structure. B) Bright-field image of energy dose array of 1% w/v Alg-MA30 with colour code applied to classify structure quality. C)-E) Processing windows for photoresists composed of Alg-MA30 for 1% w/v to 3% w/v.

The processing windows for three alginate concentrations were determined (1% w/v, 2% w/v and 3% w/v in water) for Alg-MA30 by printing a 3D hexagon or cylinder structure with an opening in the middle as depicted in Figure 4.8A and Figure A.1, respectively. Figure A.1 in Appendix 1 shows the bright field images of the processing windows for 1% w/v and 3% w/v Alg-MA30. The hatching and slicing distance were kept the same in all cases (H = 0.1 μm and S = 0.2 μm). 1% w/v of Alg-MA30 resulted in a significantly smaller processing range (Figure 4.8C). Overexposure, shown in red, could be observed starting from 28 mW and even using the highest scanning speeds of 30 mm/s structures suffered from deformation due to heating and explosions using 32 mW. 1% w/v of Alg-MA30 showed the poorest microfabrication results with a comparably small processing window and only low laser scan speeds. 2% w/v and 3% w/v of Alg-MA30 however (Figure 4.8D,E), show much wider processing windows allowing to reproducibly microfabricate robust hydrogel structures at 30 mm/s. When using 2% w/v Alg-MA for example, powers between 16 mW and 32 mW can be applied at a scan speed of 30 mm/s. By applying a power somewhere in between, e.g. 24 mW, a good quality structure can be assured circumventing any photoresist inhomogeneities. The very similar processing windows for 2% w/v and 3% w/v of Alg-MA30 suggested that 2% w/v was sufficient to obtain robust hydrogel structures at fast laser scan speeds. An interesting phenomenon could be observed when applying high laser dosages to polymerize the alginate photoresist. Without causing any observable micro-explosions during the printing process, the alginate hydrogels appeared perforated after the development as opposed to smooth hydrogel structures when lower energy doses were applied. Figure 4.9 shows SEM images of a 3D structure of the letter 'A' which were fabricated at a fixed laser power of 20 mW with increasing scan speeds starting from 6 mm/s up to 14 mm/s with 2 mm/s increments. From left to right, a substantial improvement in structure integrity could be observed. At 6 mm/s, the photoresist was overexposed which resulted in a collapsed structure that appeared almost melted by extensive heat formation during the polymerization process. At 8 mm/s, the 3D hydrogel structure ap-

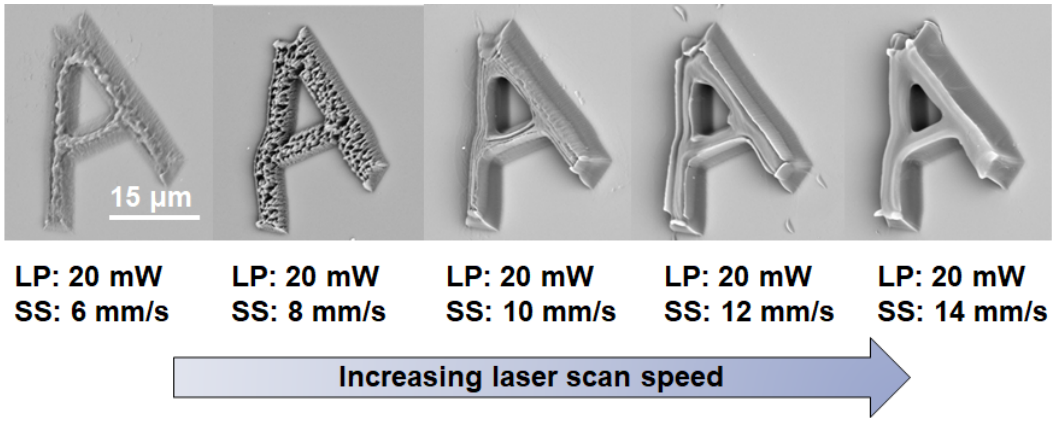


Fig. 4.9 SEM images of 2PP alginate hydrogels in the form of the letter 'A'. The structures were printed with increasing scan speeds from left to right showing improved homogeneity of the hydrogel microstructures with higher scan speeds.

peared highly porous appearance indicating an inconsistent polymerization throughout the photoresist. One possible explanation for this observation could be microgel formation discussed in the introduction of this chapter, depicted in Figure 4.2B. This would suggest that high laser dosages could favour inhomogeneous network formation with densely crosslinked areas within a less crosslinked network. The loosely crosslinked hydrogel areas are often simply washed away in the development process due to mechanical instability. Figure 4.14 for example, demonstrated how less crosslinked areas do not withstand the drying process and coating with a conductive layer necessary for SEM. When the scan speed was further increased, the hydrogels did not appear to be perforated and the structure quality improved with each scan speed increase with a 3D hydrogel structure that accurately rendered the 3D design of the letter 'A'.

4.3.1.5 Minimal linewidth

The minimal linewidth was here primarily determined to evaluate minimal feature sizes that could be achieved for 2PP of alginate hydrogels. Differences in the minimal linewidth for the varying concentrations of Alg-MA30 could additionally provide insight into the polymerization kinetics. Wider linewidths obtained at fixed laser parameters could translate to a more efficient polymerization reaction which is reflected in a larger

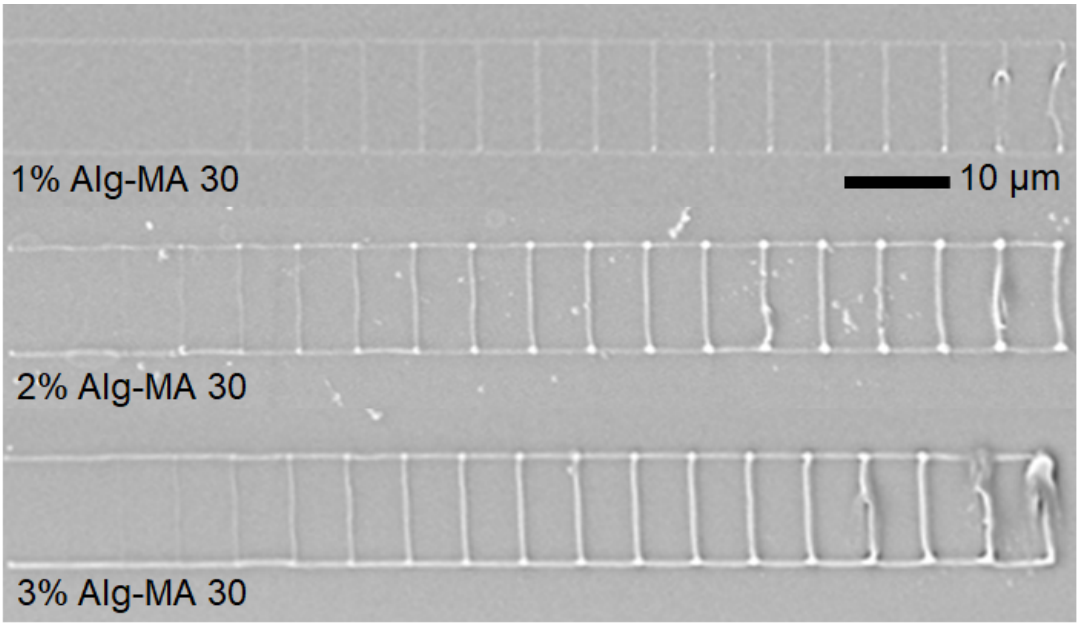


Fig. 4.10 Scanning electron micrographs of ladders printed with increasing laser powers (△LP = 2 mW) for each ladder step from left to right. Laser scan speed was kept constant at 1 mm/s.

polymerized volume. Given that the photoinitiator concentration was the same for all photoresist compositions, the polymerization of larger volumes suggests more efficient polymerization because the same number of photons absorbed lead to more crosslinking events. SEM images of 2PP ladder structures for Alg-MA 30 1% to 3% are shown in Figure 4.10. The distances were measured for each ladder step using the ImgageJ (FIJI) software and averaged. The error bars represent the average of three different measurements of each ladder step. The distances in nanometer are presented against the laser power in Figure 4.11. It has to be noted that these results were based on only one ladder printed for each photoresist composition. With increasing alginate concentrations, the polymerization threshold was at lower laser powers with 8 mW for 2% w/v and 3% w/v Alg-MA30 and 10 mW for 1% w/v which was conform with the trend of polymerization thresholds for different alginate concentrations (Figure 4.6). The minimal linewidth for all concentrations was measured for 2% Alg-MA30 with 175 nm at 8 mW. The linewidth was generally wider for higher concentrations of alginate in the photoresist. At 10 mW for example, the minimum linewidth for 1% w/v Alg-MA30 was

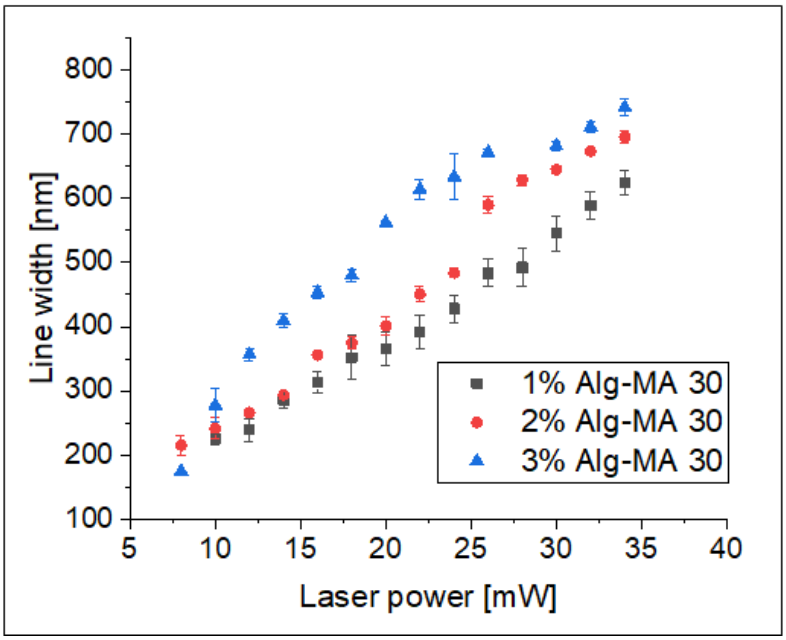


Fig. 4.11 Line width of varying concentrations of Alg-MA 30 as a function of the laser power. The data points represent the mean ± standard deviation (n = 2).

225 nm, for 2% w/v the linewidth is 241 nm and for 3% 278 nm. The difference between the linewidths for different alginate concentrations becomes more distinct with higher laser powers (Figure 4.11). Similar experiments have been performed by Wei *et al.* investigating the effect of increasing concentrations of BSA and varying photoinitiator (Rose bengal) concentrations on the linewidth. They found that the linewidth increased with higher BSA concentrations for all tested photoinitiator concentrations [80]. Their results showed a similar range for the linewidths with a minimum of 126 nm shown for 30 wt % BSA with 8.5 mM rose bengal as the photoinitiator. These combined results demonstrate the high resolution that can be accomplished.

It has to be noted that the linewidths determined here were dehydrated in order to perform SEM and would have undergone some shrinkage due to the loss of water. The hydrated linewidths may therefore be wider than the linewidths identified in this work.

4.3.1.6 2PP voxel shape affect the 3D hydrogel structure

Many experiments have shown that a voxel has the shape of a spinning ellipsoid with a larger axial length h than diameter d as depicted in Figure 2.2 [90][120]. The ratio h/d is referred to as the aspect ratio α. The voxel size depends amongst others on the numerical aperture (NA) of the objective applied to focus the laser. Most experiments discussed in this work utilized a 63x objective (Zeiss, NA = 1.4). An interesting structural effect could be observed applying a 25x objective (Zeiss, NA = 0.8) for the same *gwl*.file (see Chapter 2.1.1= as used for the 63x objective (Figure 4.12). Using the 63x objective a structure that resembled the design files was achieved (Figure 4.12 C)) whereas the 25x objective produced highly uniform and highly stable micro cones shown in Figure 4.12A and B. The cones featured more pronounced tips for structures printed with higher laser powers (Figure 4.12A). The tip of the micro-cone measured a diameter of about 110 nm showing the ability to print reproducible and stable hydrogel structures with features below the minimum linewidth when printing single lines. These results could be best explained by considering the change in the appearance of a single voxel as shown in Figure 2.2 because a 3D structure fabricated using 2PP is ultimately formed by many such voxels. Sun and co-workers have shown that the use of lower NA objectives resulted in voxels with higher aspect ratios with slimmer but taller voxel shapes [90]. These experimental findings of voxel formation were here applied to simulate 3D models using the software *describe*. Figure 4.13 illustrates the side view of a single micro-pillar structure composed of many voxels. Figure 4.13A represents the shape simulated for a less pronounced ellipsoid shape using a high NA objective whereas Figure 4.13B and C show the simulations for the same structures formed out of higher aspect ratio voxels as they would be expected for lower NA objectives. These simulations demonstrated how higher aspect ratio voxels would cause the shapes observed in Figure 4.12 that were taller and featured sharper tips than the anticipated design file.

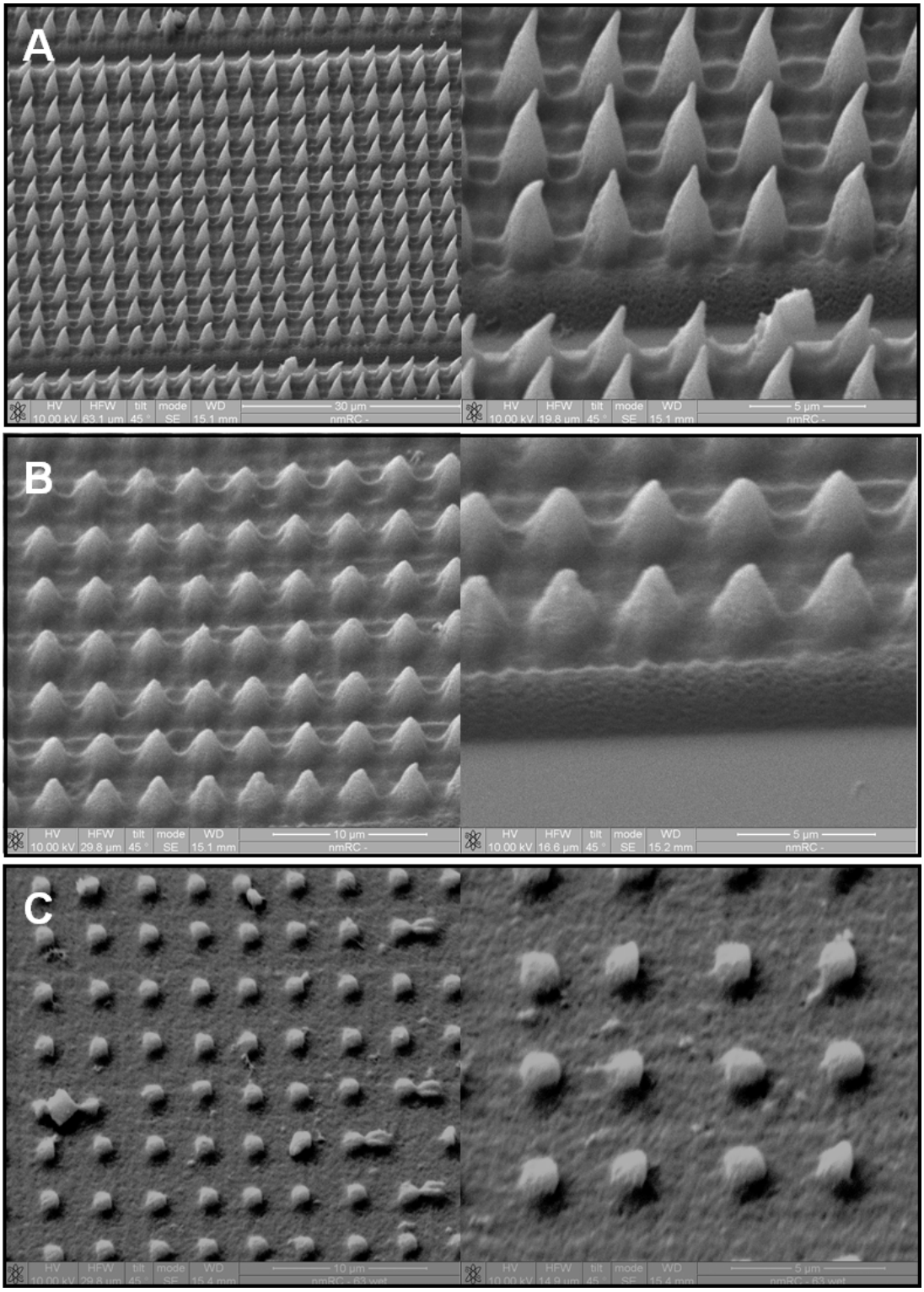


Fig. 4.12 SEM images of microstructures printed with different objectives. A) 25x objective with LP = 34 mW, B) 25x objective with LP = 24 mW, C) 63x objective LP = 24 mW.

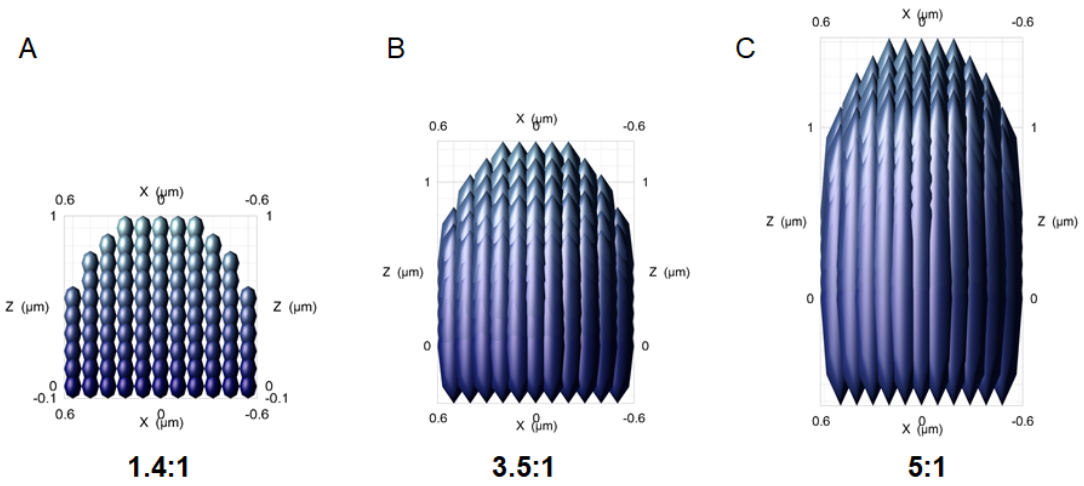


Fig. 4.13 Varying aspect ratios of voxel forming 3D structure. A) Simulation for 63x objective with smallest voxel aspect ratio, B) Simulation for 25x objective with medium voxel aspect ratio, C) Simulation for 25x objective with highest voxel aspect ratio.

This phenomenon could be exploited by identifying the exact voxel size for a given objective and parameters applied to mathematically model a desired shape using lower NA objective, thereby achieving very high resolution whilst reducing the overall printing time.

4.3.1.7 Cryo-SEM of hydrated alginate hydrogels

Hydrogels consist of polymer networks including a substantial amount of water as part of their structure. Therefore, they can be vulnerable due to poor mechanical strength, especially when dehydrated. This has to be considered for analysis. Particularly, imaging hydrogel microstructures can be very challenging and lead to artefacts since many methods do not allow the visualisation of hydrated 3D structures. Figure 4.14 A) and B) for example, show the CAD design of the word 'ALGINATE' and a bright-field image of a hydrogel structure accurately rendering the design of 2% w/v Alg-MA30, respectively. Figure 4.14C illustrates the same structure dried out and imaged with a scanning electron microscope, underlining the nature of a hydrogel that can loose its integrity when dehydrated depending on the crosslink density. Each letter was printed



Fig. 4.14 Bright-field and SEM image of 2PP alginate hydrogel of 'ALGINATE'.

with a stronger outer wall by scanning the laser with a smaller hatching distance of 0.1μm compared to 0.3μm on the inner part of the structure. Smaller hatching distances translate to bigger distances between the individual laser paths. This example shows that only the outer wall was robust enough to endure the drying process and high vacuum conditions required for SEM.

More complex imaging methods such as Cryo-SEM could circumvent this problem by enabling three-dimensional high resolution images of hydrated hydrogel structures. Cryo-SEM is here demonstrated as a valuable imaging technique on the basis of a hydrated alginate hydrogel featuring micro-pillars (Figure 4.15). These microstructures were imaged dried out compared to its hydrated state applying conventional SEM and Cryo-SEM, respectively (Figure 4.15B and C). All structures were fabricated using the same photoresist based on 2% w/v methacrylated alginate in water with 2 mol% of P2CK and the same printing parameters (LP = 28 mW, SS = 20 mm/s). The dried structures were partially distorted, especially the micro-pillars in the middle of the structure collapsed. This could be due to way the laser scans through the sample to

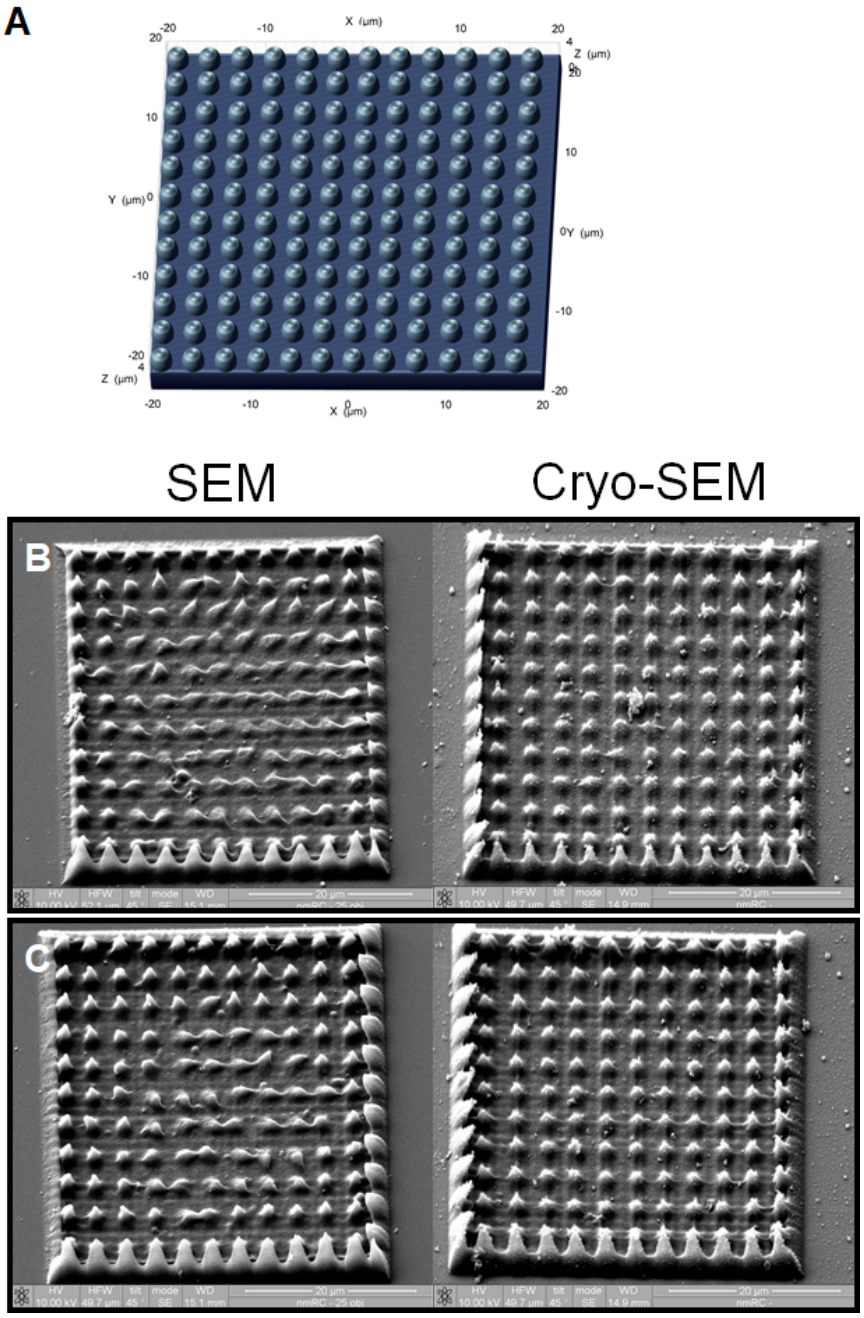


Fig. 4.15 Comparison of dry and hydrated 2PP alginate hydrogels using Cryo-SEM. A) CAD design file of 2PP microstructure. B) and C) Two independent experiments comparing a 2PP structure analysed using conventional SEM in comparison to Cryo-SEM.

polymerize a structure. The laser has to decelerate close to an edge and accelerate again turning back. This would lead to higher energy doses at the edge of the structures resulting in more crosslinked areas compared to the centre of the structure. The Cryo-SEM images however, did feature upright micro-pillars since their structure was fully hydrated and then frozen.

4.3.1.8 Raman spectroscopy to determine the degree of conversion of hydrogels

Raman spectra were recorded to assess if a hydrogel system such as 2PP methacrylated alginate could be analysed for the degree of conversion (DoC) using Raman spectroscopy (Figure 4.16). A 100% monomer solution such as PETA [121] allowed to determine the DoC by comparing the C=C and C=O bands before and after polymerization. The Raman scattering cross section of methacrylated alginate appeared to be so low however, that the diagnostic C=C and C=O bands could not be resolved in the spectra of the photoresist or the 2PP alginate hydrogels. In Figure 4.16 the spectra are shown for pure methacrylated alginate with the highest degree of methacrylate groups presented in this work (Alg-MA 40), the spectra for the photoinitiator P2CK and for the 2PP alginate hydrogel structure. Only for the pure methacrylated alginate, the C=C and C=O bands could be detected implying that the signal was too weak to be resolved.

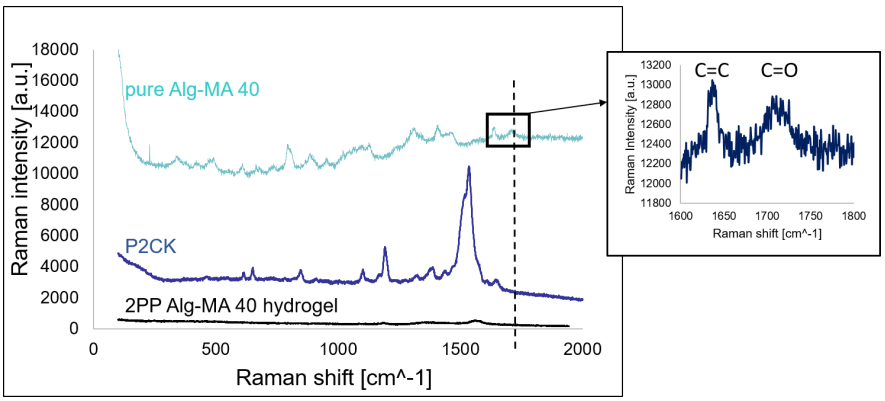


Fig. 4.16 Raman spectra obtained for alginate hydrogel, methacrylated alginate and P2CK.

4.3.1.9 Deformation ratio of 2PP alginate hyrdogels

The swelling ratio is traditionally defined as the fractional increase in the weight of the hydrogel due to water absorption [122]. It would be very challenging if not impossible to determine the weight of these microstructures attached to a glass substrate accurately. The deformation of fully hydrated structures were determined and referred to as the deformation ratio instead of swelling ratio to avoid confusion with the common interpretation of the term. The deformation ratio served as an indirect way to estimate the relative crosslink density of the various photoresist compositions. This method was here applied to investigate how the monomer concentration and the DoF of alginate with methacrylate groups influence the crosslink density.

For quantitative analysis, the perimeters of the bottom which represents the part of the structure that is attached to the glass substrate (P_b) and the top of the structure (P_t) were measured on the basis of the confocal images shown in Figure 4.17. The deformation ratio was then calculated according to equation 2 (Chapter 4.2.1.3). Figure 4.17 shows the confocal images of cubes printed using photoresists with increasing alginate concentrations against increasing DoFs. The photoresist consisting of Alg-MA18 showed insufficient polymerization for 1% w/v and poor mechanical stability for all percentages tested resulting in high deformation ratios. An increase of functional groups on the alginate showed a substantial improvement in mechanical strength, and therefore indicates a more densely crosslinked hydrogel network. The deformation ratios for Alg-MA30 and Alg-MA40 at 3% w/v show comparable structure integrity compared to the latest improvements in using modified gelatin for 2PP.

Hoorick and co-workers for example attached two photo-crosslinkable moieties to the gelatin as opposed to the commonly applied gelMOD with only one moiety [66], yielding more highly functionalized gelatins. More functionalized gelatins produced gelatin hydrogels with improved mechanical strength and no deformation when applying the same laser parameters as for gelMOD in direct comparison [67].

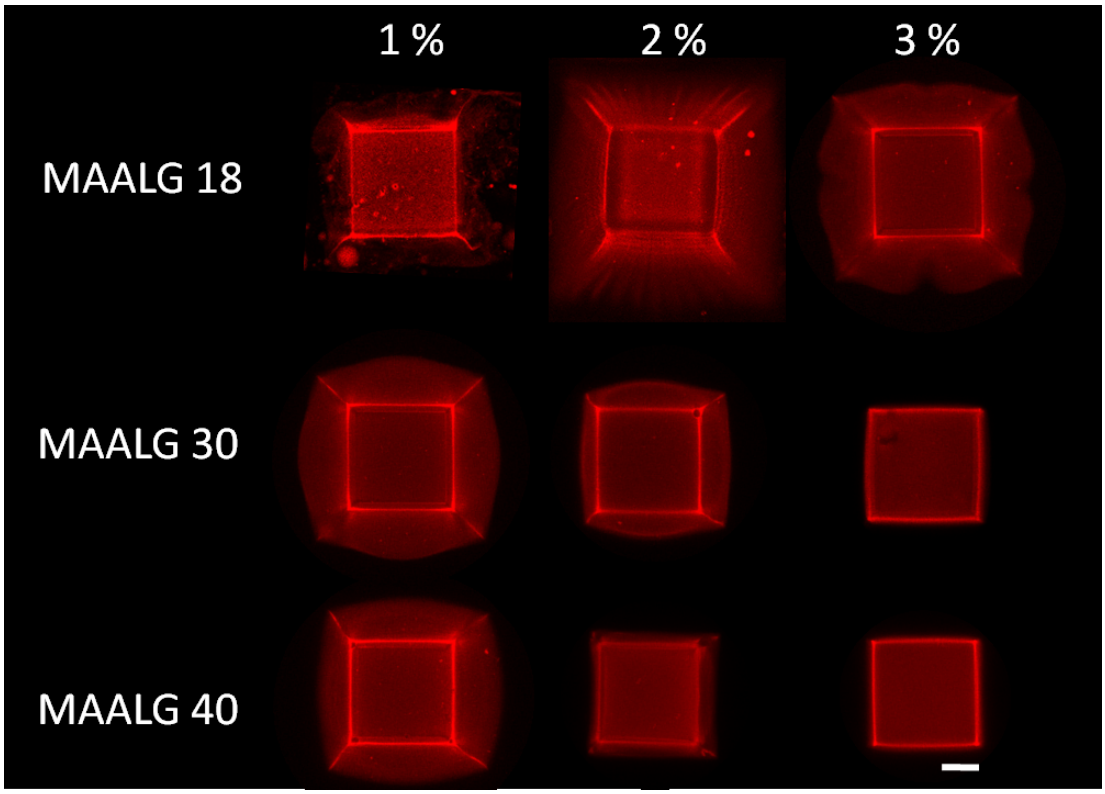


Fig. 4.17 Confocal images of 2PP fabricated alginate hydrogel cubes that were used to indirectly determine the relative crosslink density with regard to the alginate concentration and DoF of alginate with methacrylate groups, scale bar = 10μm.

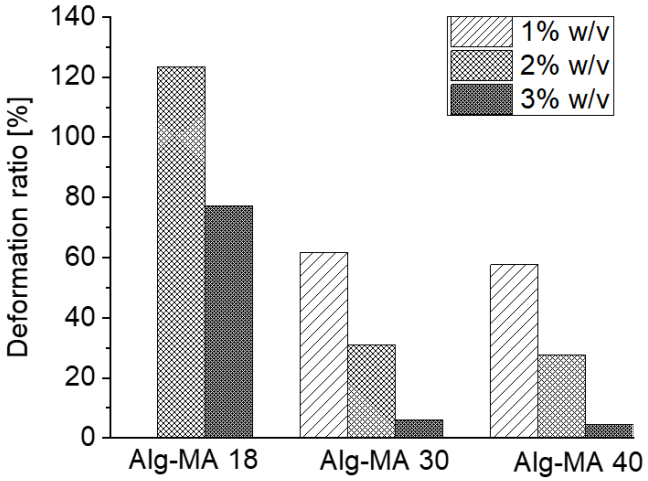


Fig. 4.18 Deformation ratio of 2PP alginate hydrogels fabricated using varying alginate concentrations versus varying degrees of substitution of methacrylated alginate.

This work demonstrates that already 2% w/v of methacrylated alginate for Alg-MA30 allowed the fabrication of stable structures with similar degrees of deformation as commonly used GelMOD [67]. Applying 3% w/v of Alg-MA30 and Alg-MA40 enable the 2PP of 3D hydrogels that accurately render the CAD designs. Figure 4.18 summarizes the calculated deformation ratios based on equation 2 to visualise the quantitative differences in the deformation ratios of the different photoresist compositions. It illustrates that and increase in alginate concentration reduced the deformation ratio significantly. The increase in functional groups showed a big improvement from Alg-MA18 to Alg-MA30. This improvement in structure integrity was only little from Alg-MA30 to Alg-MA40 suggesting that Alg-MA40 does not seem advantageous to achieve a reduction in hydrogel deformation. An increase in alginate concentration however, featured a significant improvement on the mechanical integrity of the hydrogels and could be further exploited by applying even higher alginate concentrations depending on the required hydrogel properties. However, these results are only based on one measurement and should be repeated on a statistical basis to be conclusive. Due to the coupling of the alginate concentration and the viscosity, it can also not be

distinguished which factor if not both lead to increased mechanical integrity of 2PP alginate hydrogels. The viscosity could for example be increased without changing the alginate concentration by adding a controlled amount of Ca^{2+} ions introducing partial crosslinking of the alginate molecules in solution.

4.4 Conclusions

- The combined results discussed in this chapter demonstrate that methacrylated alginate represents an excellent basis for efficient 2PP of 3D hydrogels enabling the microfabrication with sub-micron resolution.

- The viscosities of the methacrylated alginate samples increased significantly with increasing alginate concentration.

- Increasing laser speeds generally raised the polymerization- and damage-thresholds P_{th} and D_{th} for all photoresists. Alg-MA40 based photoresists showed the lowest P_{th} and the highest D_{th} values resulting in the largest dynamic power ranges.

- Concentrations of at least 2% w/v should be used to fabricate stable 3D alginate hydrogel structures. 1% w/v of Alg-MA30 showed the poorest microfabrication results with a comparably small processing window. 2% w/v and 3% w/v Alg-MA30 featured wider processing windows enabling the fabrication of robust hydrogel structures at the highest laser scan speeds used.

- 3D hydrogels composed of Alg-MA18 featured poor mechanical integrity compared to Alg-MA30 and Alg-MA40 that allowed to print 3D hydrogels closely rendering the CAD design. Increasing concentrations of alginate significantly reduced the deformation ratio for all alginate hydrogels.

- Minimal linewidths down to 175 nm were achieved for 2% w/v Alg-MA30. Linewidths were generally wider for higher concentrations of alginate in the photoresist.

- Cryo-SEM was successfully applied to image alginate hydrogels in its hydrated state

Chapter 5

Two-photon polymerized hydrogel structures for applications in cell culture

5.1 Introduction

In this chapter, two-photon fabricated alginate hydrogels were probed for potential cytotoxic effects on bacterial as well as mammalian cells. It was studied if a selected set of micro-topographies affects cell response such as attachment and growth.

Two bacterial species were tested, a representative for a Gram-negative (*Pseudomonas aeruginosa*) and a Gram-positive bacterium (*Staphylococcus aureus*) that are commonly associated with medical device infections and pathogenic biofilms [123][124]. In particular, several micro-topographies were evaluated for their ability to prevent bacterial adhesion.

Mesenchymal stem cells (MSC) have been isolated from numerous different tissues and studied extensively [125]. They can differentiate into various cells of connective tissue lineages, including bone, fat, cartilage and muscle and are recognized for their therapeutic value and use in regenerative medicine [126]. A complex interaction of

chemical and physical cues from the microenvironment of cells enables them 'to decide' which type of cell to differentiate to [127]. Several experiments suggest that the cell shape can independently direct the differentiation of hMSCs [128][129]. Kilian and co-workers for example, demonstrated that cells cultured in rectangles with increasing aspect ratio and in shapes with pentagonal symmetry but with different subcellular curvature, resulted in distinct adipogenesis and osteogenesis differentiation profiles. They concluded that these results must stem from the shape since the overall cell-surface area was kept the same by applying micro-patterned surfaces to control cell shape [129]. Geometric features that increase actomyosin contractility appeared to promote osteogenic differentiation.

Successful experiments of growing MSCs on alginate scaffolds have previously been reported, e.g. for the treatment of myocardial infarction where alginate scaffolds can be used as a protective cell carrier for implanting MSCs into damaged tissue for regeneration [130]. Due to the promising results of using alginate scaffolds with MSC for the treatment of heart diseases, Ceccaldi *et al.* looked into the impact of different alginate compositions and resulting mechanical properties. They concluded that all compositions show good biocompatibility in which alginates containing a higher L-guluronate (G) content are mechanically stronger. They suggest that further studies are necessary to identify optimal porosities for efficient cell loading and determine adequate mechanical properties for implants [130].

This work aimed to demonstrate that 2PP of alginate hydrogel is an efficient microfabrication method to obtain 3D alginate hydrogels of arbitrary shape with submicron features, that e.g. could be exploited to tailor scaffold structures. Cell loading and proliferation could be improved through optimized microscopic designs. Smart features could be applied to influence cell attachment, morphology and differentiation of MSCs in a controlled fashion [126][131][132]. The high resolution printing of alginate hydrogels that can be realised using 2PP even allows to introduce micro-topographies on the scale of bacterial cells that are about 20x smaller than MSCs ($d_{BA} \approx 0.5 - 2\ \mu$m;

$d_{MSC} \approx 20 - 30 \mu m$). Such micro-topographies can be used to reduce bacterial attachment for example. The combined efficiency and high resolution possible using 2PP of alginate hydrogels emphasizes the wide applicability of this new approach.

5.2 Experimental methods

5.2.1 Design rationale of hydrogel microstructures

All structures were designed and printed as described previously (Chapter 2.1.1). The designs for bacterial attachment experiments were adapted from various topographies inspired by topographical features that showed reduced bacterial attachment. The commercialized anti-fouling design called Sharklet® (Sharklet AF^{TM}) was adapted for this work (Figure 5.7). The topography was originally motivated by the skin of a Galapagos shark and shown to reduce bacterial colonization [133][134]. Additionally, topographies of micro-pillars with varying distances between each other were tested which were inspired by previous findings showing that the distance between simple micro-structures can impact the extent of bacterial attachment [135]

One such micro-pillar design, with a wider pillar distance of 8 μm, was also tested for hMSCs (Figure 5.1). De Boer and co-workers developed a high-throughput strategy for testing thousands of randomly generated topographies on a so called 'Topochip' platform based on simple geometrical forms with features in the range of a few to tens of microns [132]. Hence, another microstructure was tested which was inspired by such a 'Topochip' design that showed slower proliferation of hMSCs compared to a flat surface shown in Figure 5.2 (Vasilevich *et al.*, unpublished data). [136][137].

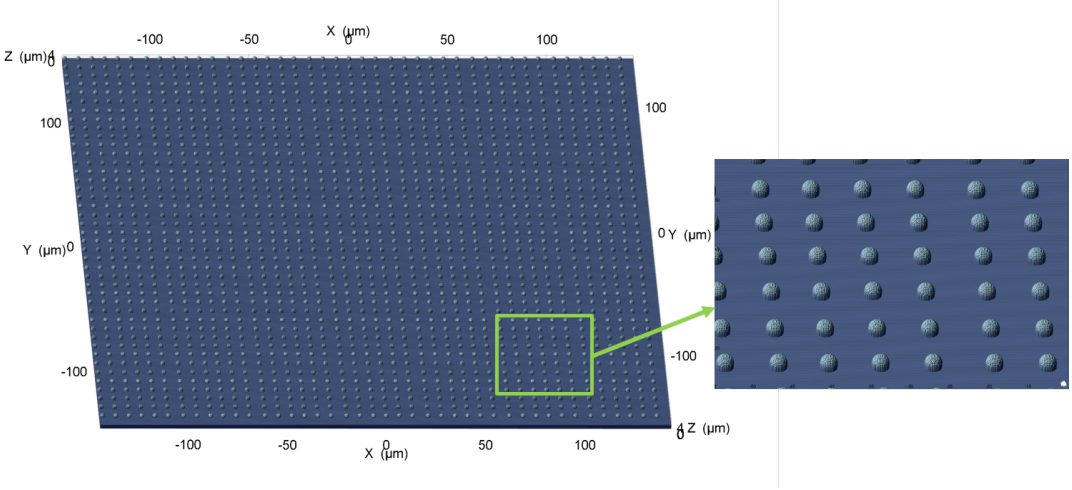


Fig. 5.1 CAD design of microstructured surface (a = 300μm x 300μm) featuring short micro-pillars with 8 μm spacings.

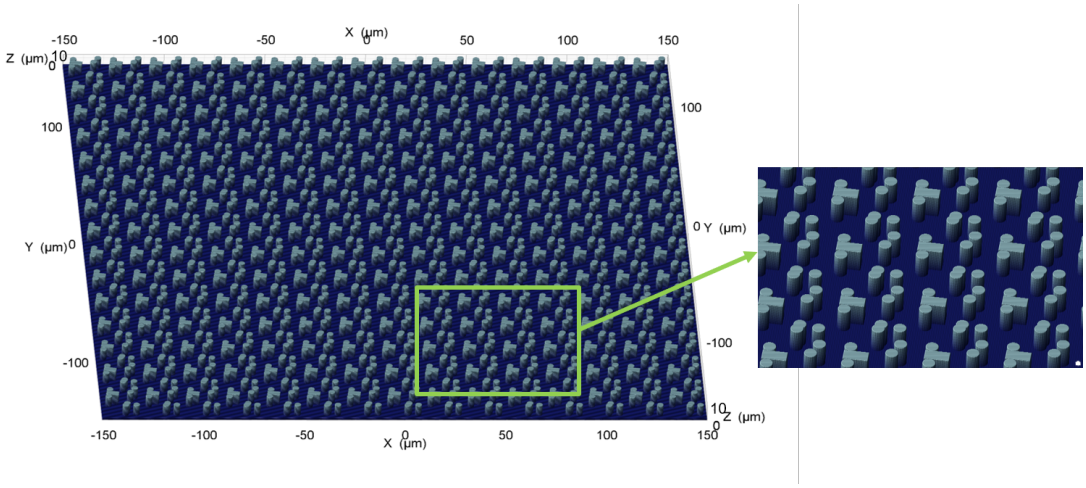


Fig. 5.2 CAD design of microstructured surface (a = 300μm x 300μm), with feature sizes between 3 μm to 10 μm and a height of 10 μm, inspired by Topochip design 1008 (Vasilevich *et al.*, unpublished data).

5.2.2 Confocal image analysis of encapsulated bacteria

Confocal microscopy was used to visualize bacterial growth within 3D microarchitectures using the laser scanning microscope LSM700 (Zeiss). All images were obtained with an oil-immersion objective (Plan-Apochromat 63x, 1.40 N.A. DIC M27) recording the signal of two lasers ($\lambda = 405$ nm, $\lambda = 555$ nm) through two different channels simultaneously in order to enable the distinction between the autofluorescence of the protein microarchitecture caused by the photosensitizer and the fluorescence emitted by the bacterial cells.

5.3 Results and Discussion

5.3.1 Bacterial growth

5.3.1.1 Bacterial growth in the presence of monomers and photoinitiators used for 2PP

Two bacterial species were used in this work as representatives of two different classes, *Pseudomonas aeruginosa* (PAO1) for gram-negative and *Staphylococcus aureus* SH1000 for Gram-positive pathogens that are commonly associated to medical device infections. All monomers and photoinitiators that were part of the photoresist for 2PP of microstructured hydrogels were tested for growth inhibition of the two bacterial species used in this work. The growth curves, illustrated in Figure 5.3, show that none of the monomers inhibited the growth of *P. aeruginosa* or *S.aureus*. Each growth curve represents the average of three replicates with an error bar indicating the standard deviation (SD). The photoinitiators P2CK and rose bengal (RB) reduced the growth to different extents depending on the bacterial species. *S. aureus* only showed a substantially slowed growth for RB whereas *P. aeruginosa* was affected by both, RB and P2CK.

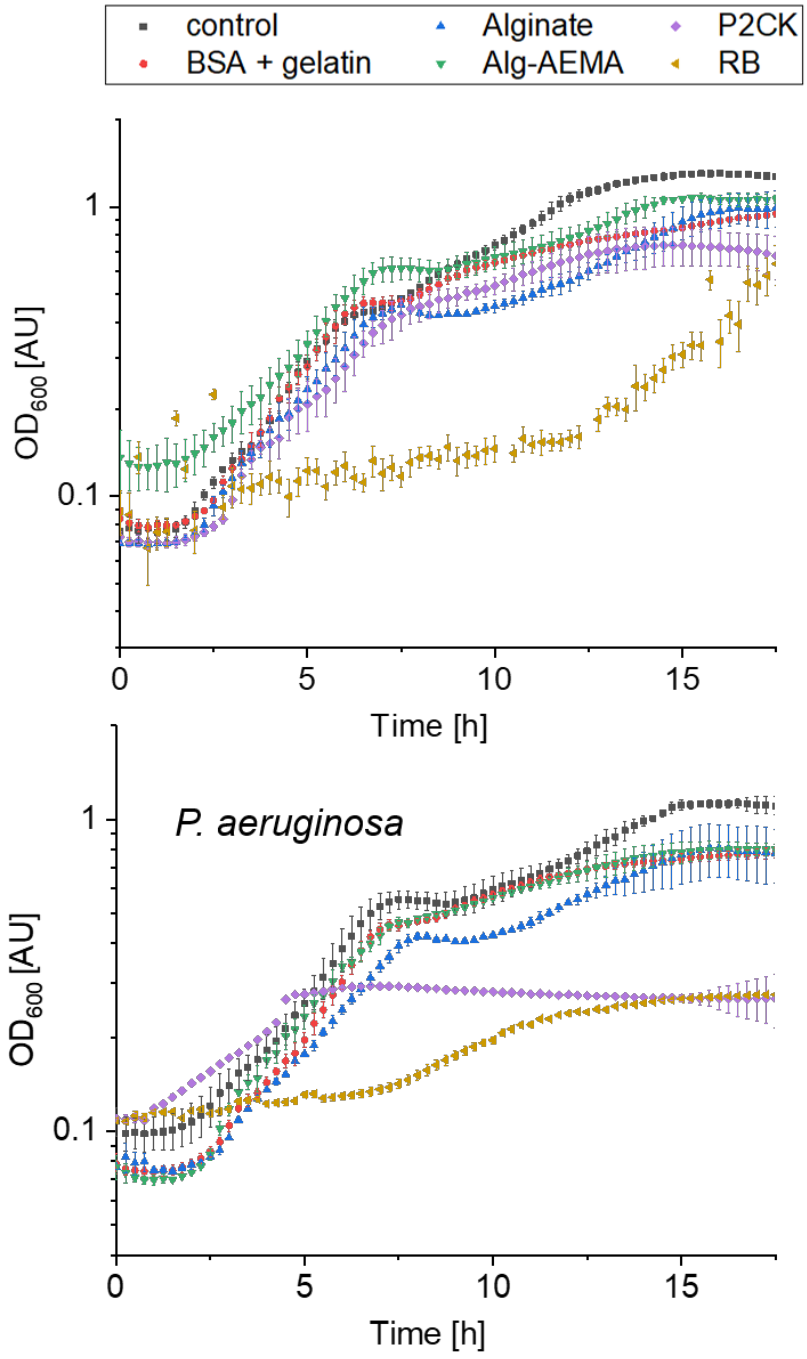


Fig. 5.3 Growth curves for A) *S. aureus* and B) *P. aeruginosa* in LB medium at 37°C for 17.5 hours, respectively. Each curve represents the average of three replicates with error bars indicating the standard deviation (SD) of the replicates.

Bacteria growing in the presence of P2CK initially grew as rapidly as the control (exponential growth phase) with only bacteria but were inhibited after around 5 hours (stationary growth phase). In the presence of RB however, the bacteria are inhibited from the beginning and grew more slowly than the control. Bacterial toxicity of RB was already reported in 1978 in the presence of light which was found to be due to photogenerated singlet excited oxygen [138]. This could explain the retarded bacterial growth for both species at the beginning when the RB mixture was exposed to light which could generate higher concentrations of singlet oxygen in solution. During the experiment, the solutions were shielded from light with only short pulses of light during the absorbance measurements. P2CK has been synthesized for the first time in 2013 [107] with the purpose of improved biocompatibility. To the best of our knowledge, it has not been used in the presence of bacterial cells but is cytocompatible with mammalian cells at concentrations used for 2PP [107]. Our results suggest that P2CK is less toxic to the two bacterial species tested in this work.

For *P. aeruginosa*, colony forming units (CFUs) were additionally determined after 18 hours of growth for dilutions of 10^{-3} and 10^{-4} (for details see Chapter 2.5.3). The results are summarized in Figure 5.4. The CFU supported the results from the growth curves namely that only the photoinitiators reduced the number of live bacterial cells in suspension compared with the control with bacteria only. Interestingly, the number of living cells is about 48% higher in the presence of alginate compared with the control as well as Alg-AEMA and BSA that are in the same range. Most strains of *P. aeruginosa* produce alginate as part of their extracellular matrix, which enables them to produce a mucoid biofilm [139]. *P. aeruginosa* carries many genes involved in the biosynthesis and enzymatic degradation of alginate which could potentially explain the increased number of viable bacteria observed during growth in the presence of alginate [140]. These results remain preliminary however and would need to be repeated to obtain statistical results. Additional studies investigating the change in growth behaviour and

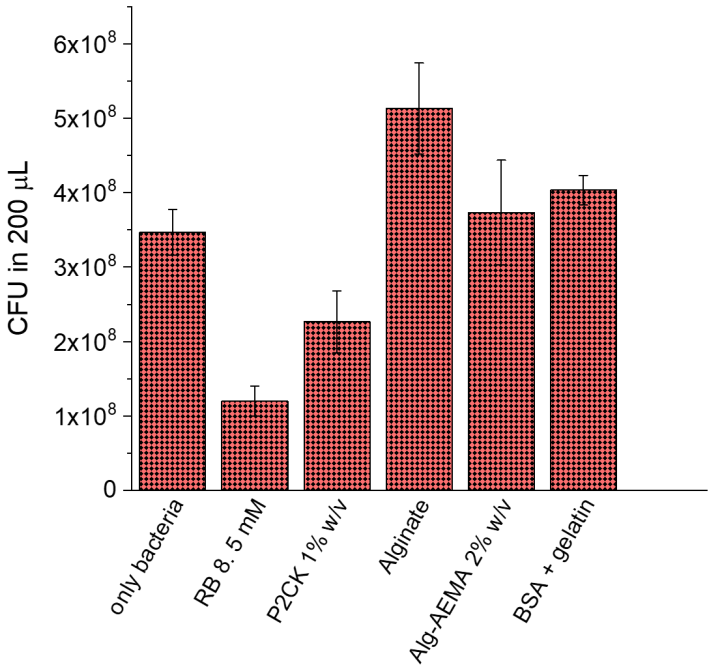


Fig. 5.4 Colony forming units (CFU) for *P. aeruginosa* in 200 μL LB medium. A volume of 10 μL for all three replicates of each condition (Figure 5.3) was pipetted on agar plates and incubated overnight at 37°C. The error bars represent the standard deviation (SD) of three replicates.

CFU count in relation to the concentration of the tested chemicals could help clarify their toxicity on the bacterial cells.

5.3.1.2 Microstructured hydrogels affect bacterial attachment

Staphylococcus aureus

The effect of alginate was investigated featuring micro-cones of 1μm and 3μm spacing (Chapter 1.3.1.5) in comparison with a flat alginate hydrogel surface. The number of cells attached to the surface after 14 hours of incubation in LB medium was determined using SEM. Representative micrographs from overall three biological repeats are shown in Figure 5.5. The bacterial CFU counts of the biological repeats are summarized in Figure 5.6. Surfaces with 1μm distance between the micro-cones resulted in 2.5 times up to 8 times more bacteria attached to the surface compared to the flat surface. Surfaces

with 3μm spacings showed about 1.3 times up to almost 3 times more bacteria relative to flat surfaces. The increased number of bacterial cells attached to microstructured surfaces could be due to the cells being protected from shear forces caused by a gentle but continuous shaking (30 rpm) of the medium during the incubation. Since the pillar spacing was wide enough to accommodate *S. aureus* cells (d$\approx$ 1 μm), they could have acted as a shelter for the bacteria and hence, allowed for more cells to attach.

Our findings agreed with related work investigating similar microstructures [135][141]. Valle and co-workers for example, used direct laser interference patterning (DLIP) to modify polystyrene surface topography at the micron scale with similar pillar structures that varied in spacing and showed that gaps between 1μm and 5μm enhance the attachment of *S. aureus* whereas sub-micrometer patterns reduced the attachment. It is proposed that surface features on the scale of individual bacterial cells could allow them to maximise the bacteria-surface contact area which would enhance cell attachment. Whitehead *et al.* investigated the effect of surface roughness on bacterial attachment and showed experimentally that bacterial attachments only start to be prevented for topographical features at the scale of single cells and becomes more prominent for nano scaled features smaller than bacterial cells [141]. These findings were explained on the basis of cell-substrate interactions suggesting that the cell is more likely to retain to the surface if the space between topographical features fits at least one cell which ultimately increases the binding energy.

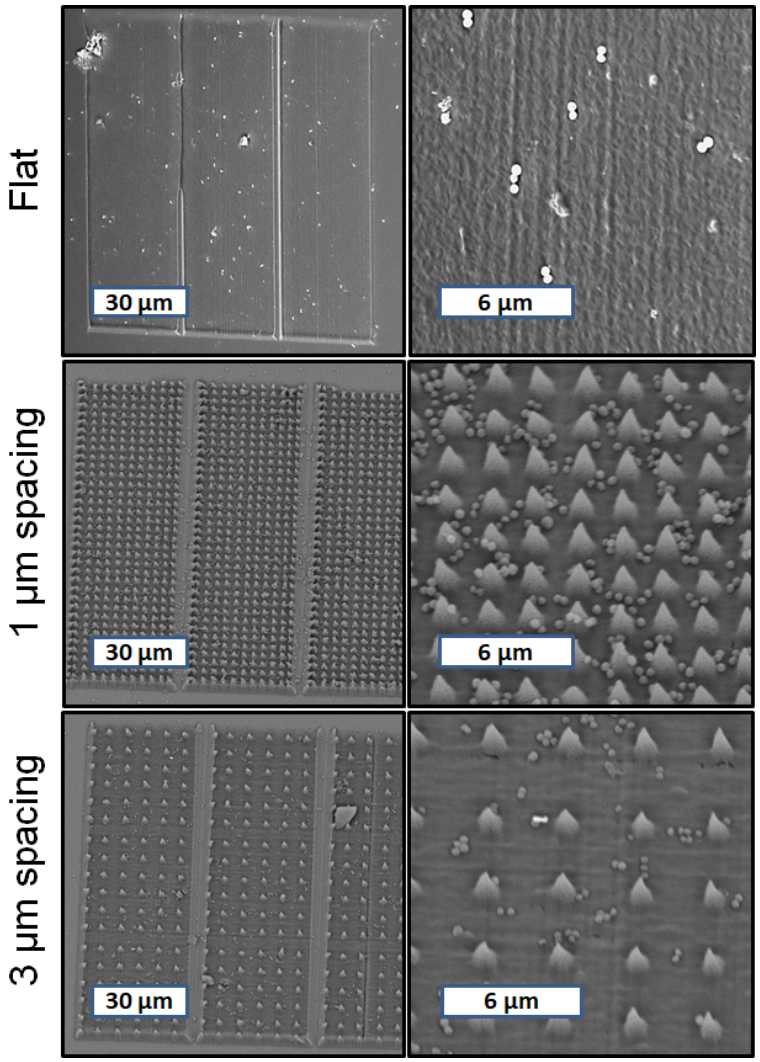


Fig. 5.5 Representative scanning electron micrographs of *S. aureus* growing on microstructured alginate hydrogels with short pillars and variable spacing of 1 μm and 3 μm compared with a flat surface.

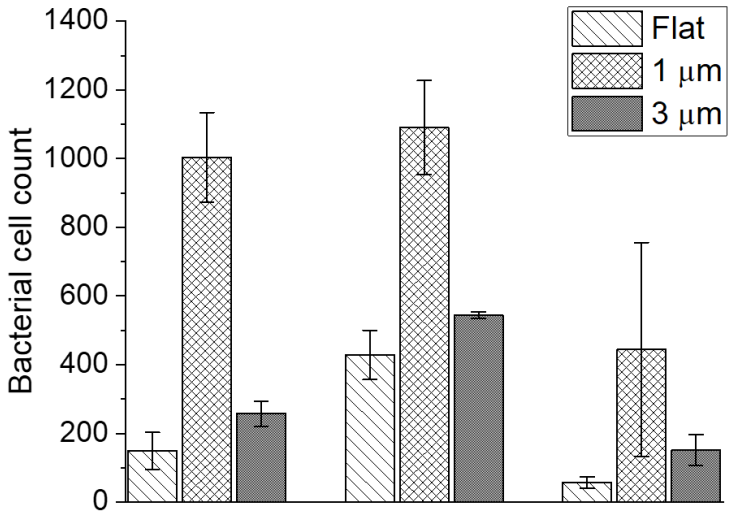


Fig. 5.6 Bacterial total cell count of *S. aureus* growing on microstructured alginate hydrogels with short pillars and variable spacings. The total number of cells was determined using image analysis of SEM micrographs. The error bars represent the standard deviation of three surfaces.

Pseudomonas aeruginosa

P. aeruginosa was cultured on a more extended set of surfaces than *S. aureus* as discussed above. In addition to short micro-pillars with 1μm and 3μm spacings, the sharklet® design as well as micro-pillars without any spacing were tested (Figure 5.7). Complementary to cell counts determined from SEM micrographs, we used confocal image analysis to quantify the number of cells attached to the surfaces by monitoring the fluorescence signal emitted from the protein markers expressed by the the bacteria. Fluorescence microscopy was here used in addition due to the lower contrast between the surface and the rod shaped *P. aeruginosa* cells using SEM. Furthermore, confocal images only record alive cells because the fluorescent protein was expressed by the bacterial cells. Dead cells were therefore not considered in the bacterial cell count. Figure 5.8 shows representative images of two biological replicates and Figure 5.9 summarizes the bacterial cell counts. The second repeat generally featured fewer cells

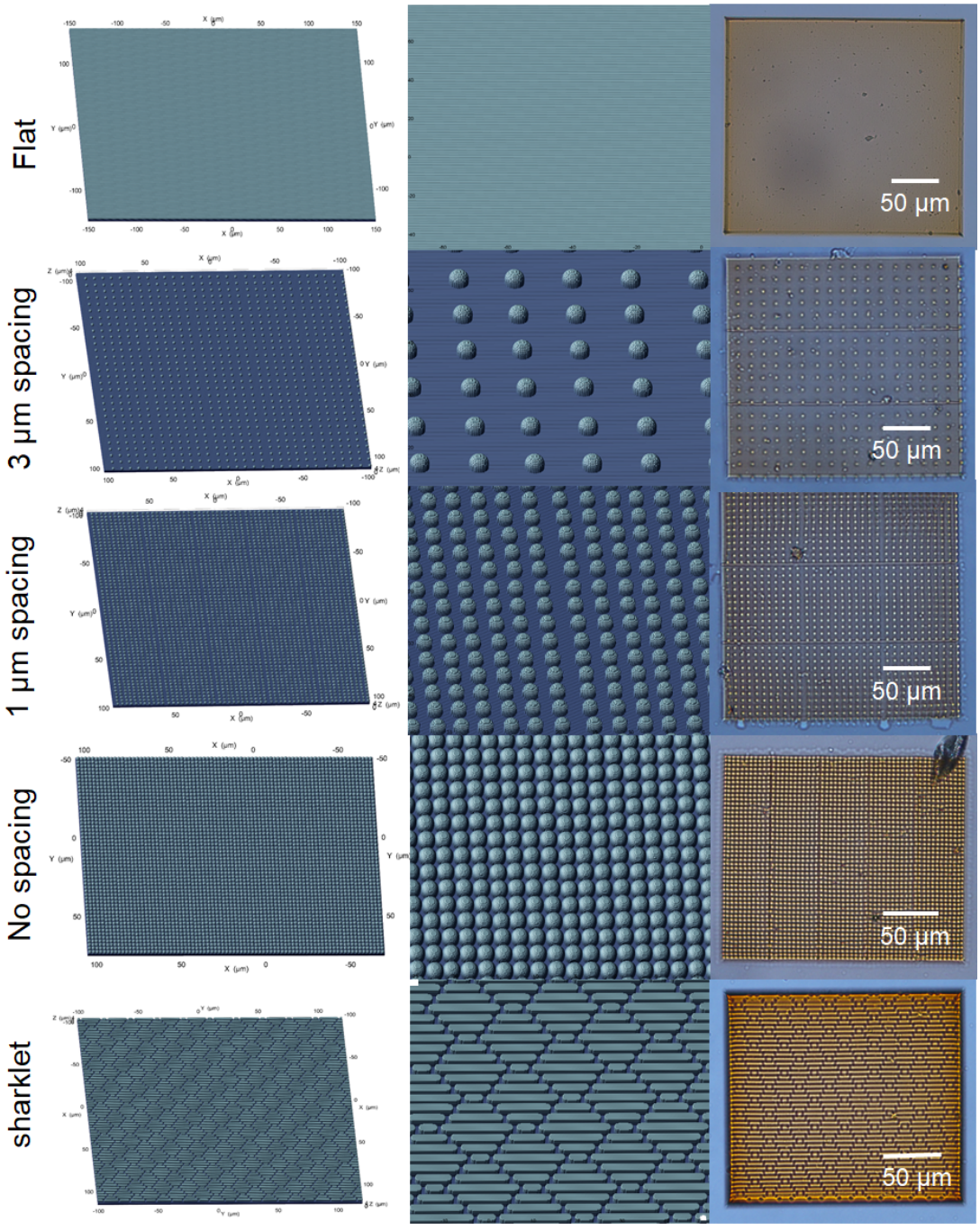


Fig. 5.7 CAD files of topography designs (left, middle) and bright-field images of 2PP alginate hydrogels resembling the CAD designs (right).

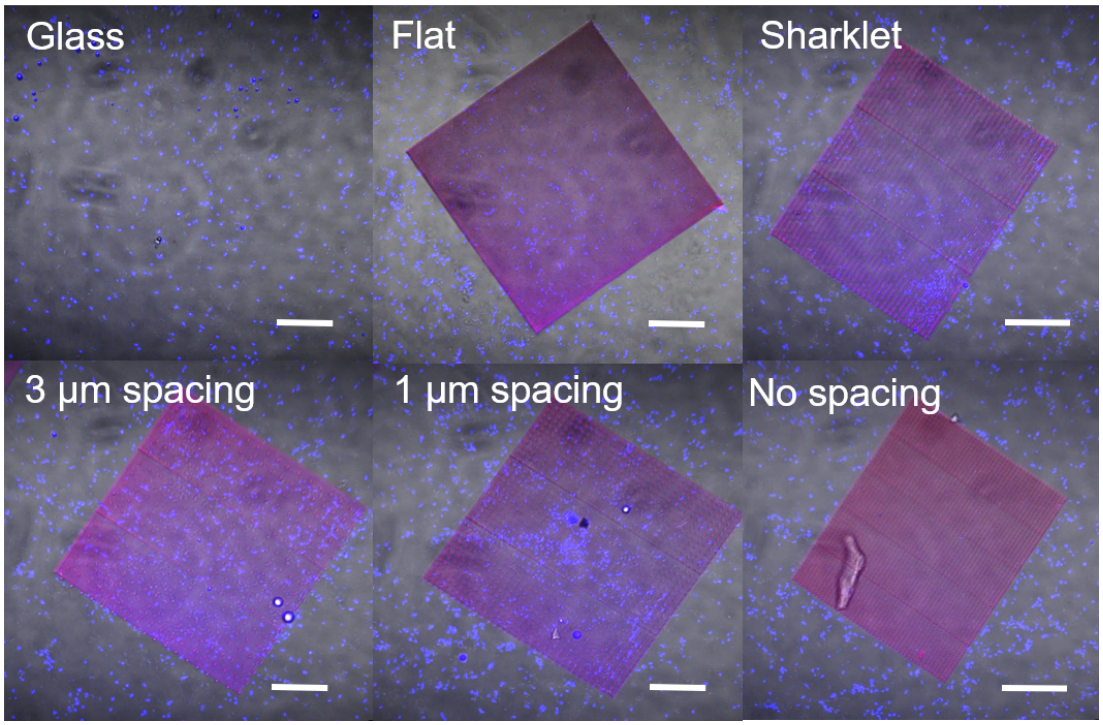


Fig. 5.8 Representative fluorescence images of *P. aeruginosa* expressing the fluorescent dye *mTurquoise2* (blue) growing on microstructured alginate hydrogels. Four different designs were tested and compared with flat surfaces. Scale bars = 50 μm

but showed similar relative numbers of cells attached to the individual surfaces. Both repeats resulted in a highly reduced number of bacterial cells attached to surfaces with micro-pillars with no spacings in between compared to all other surfaces including only glass. Short micro-pillars with 1μm and 3μm spacings featured more cells than the flat structures as well as only glass which was also observed for *S. aureus* discussed above. The adopted sharklet® design showed differing results for both repeats: in the first repeat, a higher number of cells attached to the surface in comparison to the flat structure and the glass. In the second repeat however, only few cells attached to the sharklet® surface. Overall, the spacings between the micro-pillars resulted in the most distinct differences in the number of cells attached to the surfaces. Whilst 1μm and 3μm spacings promoted increased attachment in comparison to the flat and the glass surface, pillars with no spacing reduced cell attachment (Figure 5.9). These results are only preliminary and can merely indicate trends of how the bacterial cells behave on

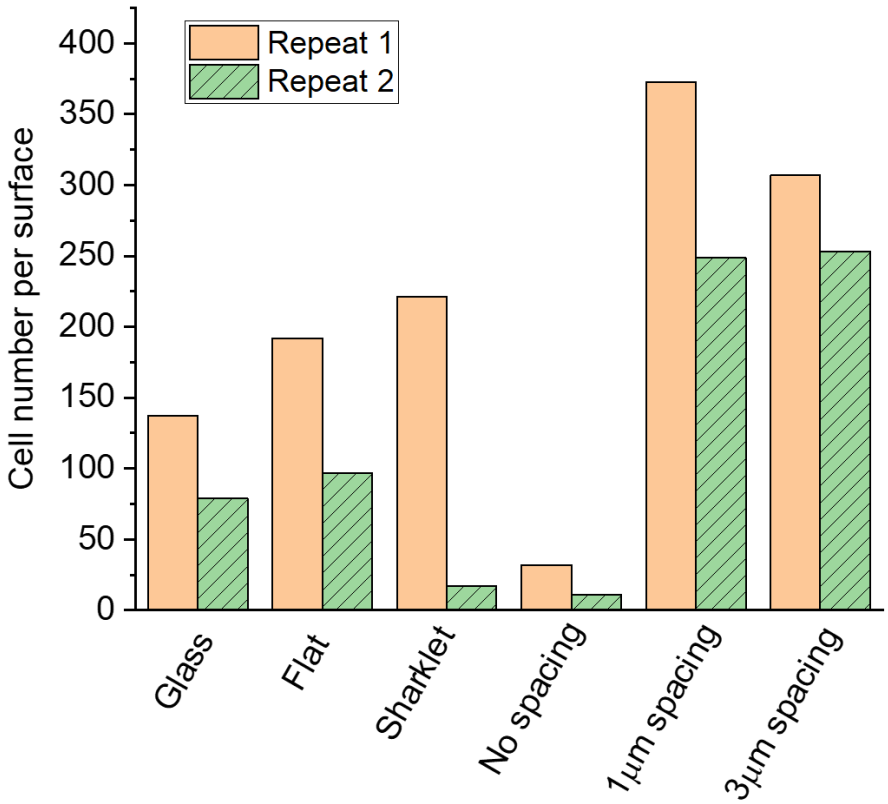


Fig. 5.9 Bacterial cell number attached to the different surfaces determined using image analysis of fluorescence micrographs. The experiment was performed for two biological samples for each surface. All samples were incubated for ≈ 16 hours at 37°C in LB medium.

microstructured hydrogels. In order to exclude any chemical effects (e.g. inpurities) and variations in 2PP hydrogel compositions, theses experiments have to be repeated multiple times in order to analyse the attachment behaviour statistically. Particularly, the sharklet® design was inconclusive as it featured good attachment in the first sample whilst hardly any bacteria attached to it in the second sample. This work shows that 2PP alginate hydrogels can be efficiently fabricated with sub-micrometer resolution and is cytocompatible. To unlock its true potential for applications in cell culture, statistical topography analysis could be performed using cheaper and faster techniques to identify effective topographies. These hit topographies could then be exploited for 2PP alginate hydrogels.

The first repeat was also analysed by means of SEM, meaning that after confocal images were acquired, the bacterial cells were fixed and dehydrated as described in chapter 2.2.2.2 and subsequently imaged using SEM. The images are summarized in Figure 5.11 with an overview and a close-up of each surface including only glass. Due to a low contrast obtained between some of the surfaces and individual bacterial cells as well as cells that appeared disrupted, the bacterial cell count shown in Figure 5.11 represents a rough estimate of cells attached to the surface rather than exact numbers. Due to this complications of using SEM to determine the number of attached cells, we applied only confocal image analysis was used for the second repeat of *P. aeruginosa* growing on various alginate surfaces. Compared to the confocal image analysis, the cell counts were higher for most of the surfaces which can be explained by considering that all cells that were attached to the surfaces were being counted using SEM image analysis. Confocal image analysis however, only captured living bacterial cells that expressed the fluorescent marker *mturquoise2*.

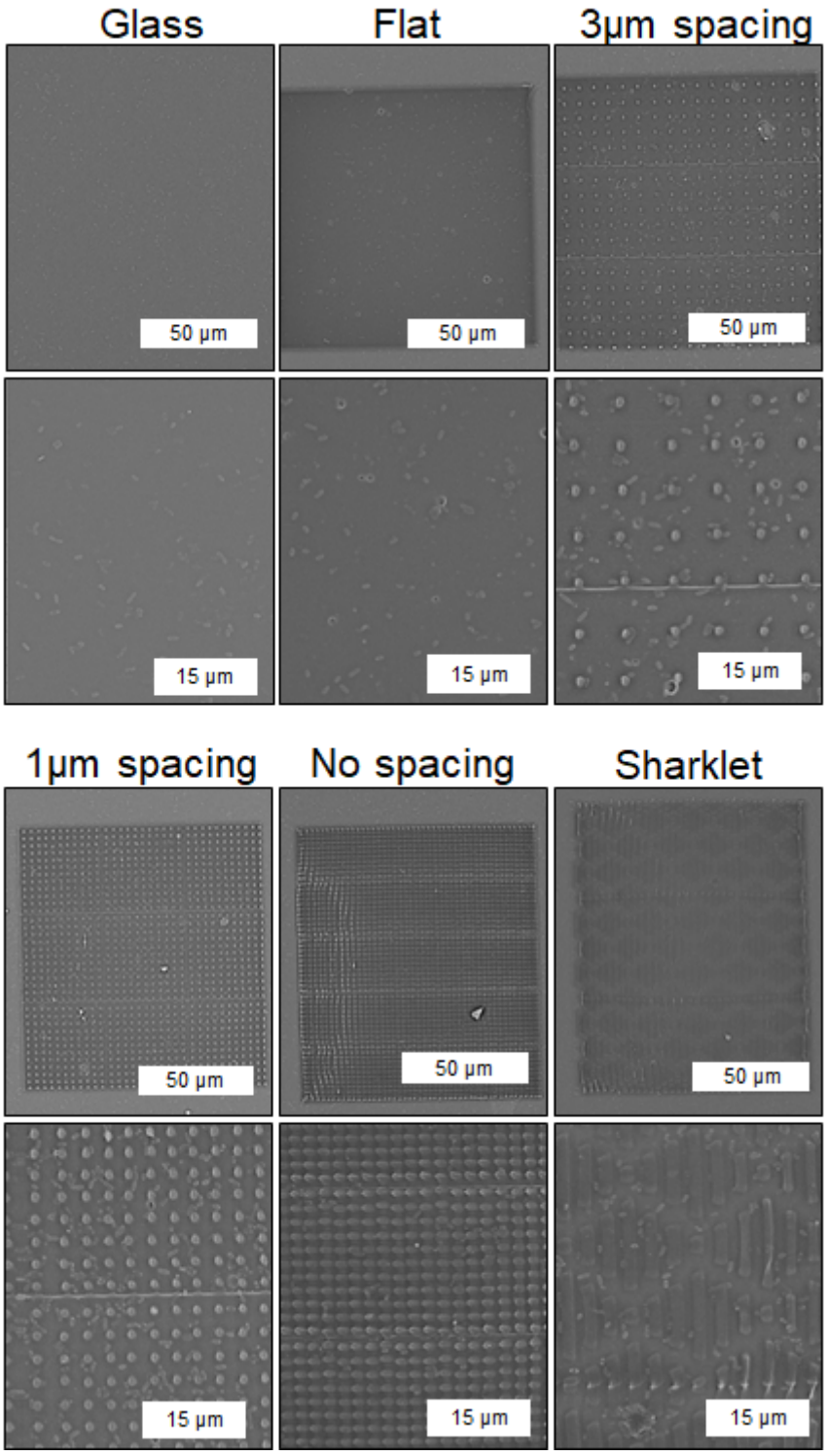


Fig. 5.10 SEM micrographs of *P. aeruginosa* growing on microstructured alginate hydrogels. An overview of the entire surface (Top row) and a close-up are shown for each topography (bottom row).

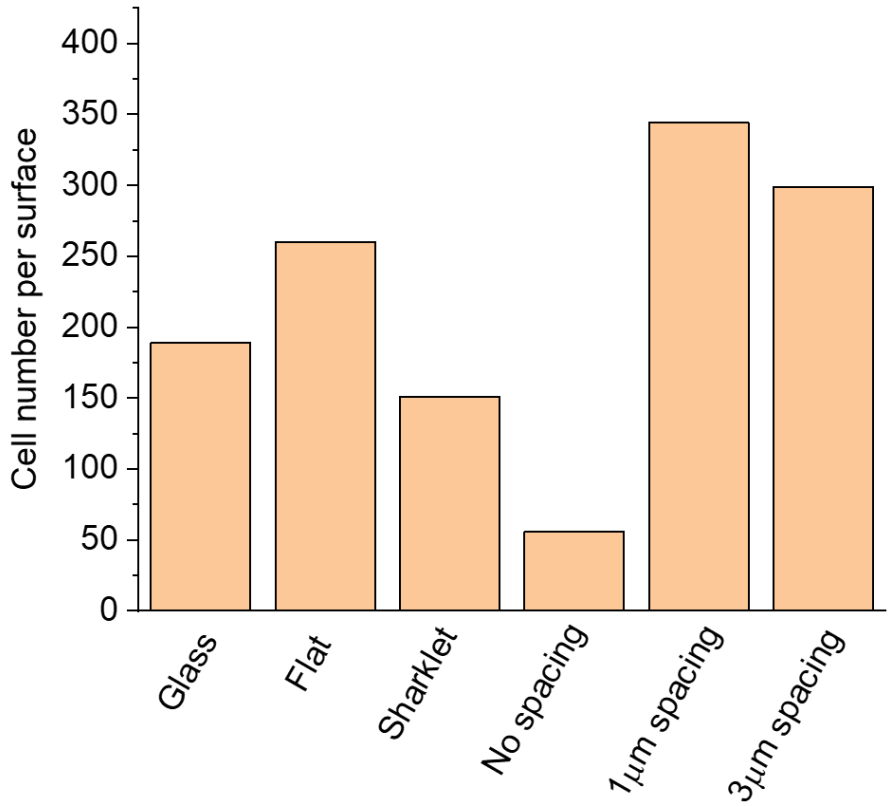


Fig. 5.11 Bacterial cell count of *P. aeruginosa* attached to microstructured alginate hydrogels based on SEM micrographs.

5.3.1.3 Encapsulating bacteria in BSA/gelatin based hydrogel microstructures

In this section, the aim was to demonstrate the ability to print in the presence of living cells and encapsulate the cells within hydrogel microstructures in which they remain viable overnight when cultured in growth medium. Common polymers as well as biological tissue show negligible linear absorption in the near-Infrared (NIR) range [64][65], allowing the laser to penetrate the photoresist as well as living cells without damaging them. The transparency of tissue to NIR light enables the microfabrication in the presence of living cells. The encapsulation of living bacterial cells could be shown growing within a 3D hydrogel microstructure using the commercial system nanoscribe which builds on previous experiments of Connell *et al.* using a customized 2PP set-up to encapsulate bacteria in hydrogel structures [83].

The initial considerations to culture bacteria in 2PP microstructures were to ensure enduring architectures that concurrently allow for the diffusion of nutrients and solutes in and out of the microstructure. All images depicted in Figure 5.12 were recorded after incubating the encapsulated bacteria overnight in TSB medium at 37°C. The autofluorescence of the microstructure itself could be overcome by using two different laser wavelengths (λ = 405 nm and λ = 555 nm) to allow the resolution of the fluorescent signals emitted by the bacterial cells and the microstructure. Compared to the fluorescent protein *mcherry* expressed by the bacteria, the absorption of rose bengal covers a broad wavelength range between 460 nm to 600 nm. Figure 5.12 D) shows the signal recorded through only one channel (channel 1 = red) whereas Figure 5.12 E) illustrates an overlap of the two channels (channel 1 = red and channel 2 = green). The bacteria could only be observed through channel 1 which enabled the distinction between bacteria and microstructure. Figure 5.12 A) and B) show the successful encapsulation of bacteria in a series of barrel structures. It appears that two out of the six visible structures had a defect and lost the captured bacteria during the procedure. In the cross-section view of

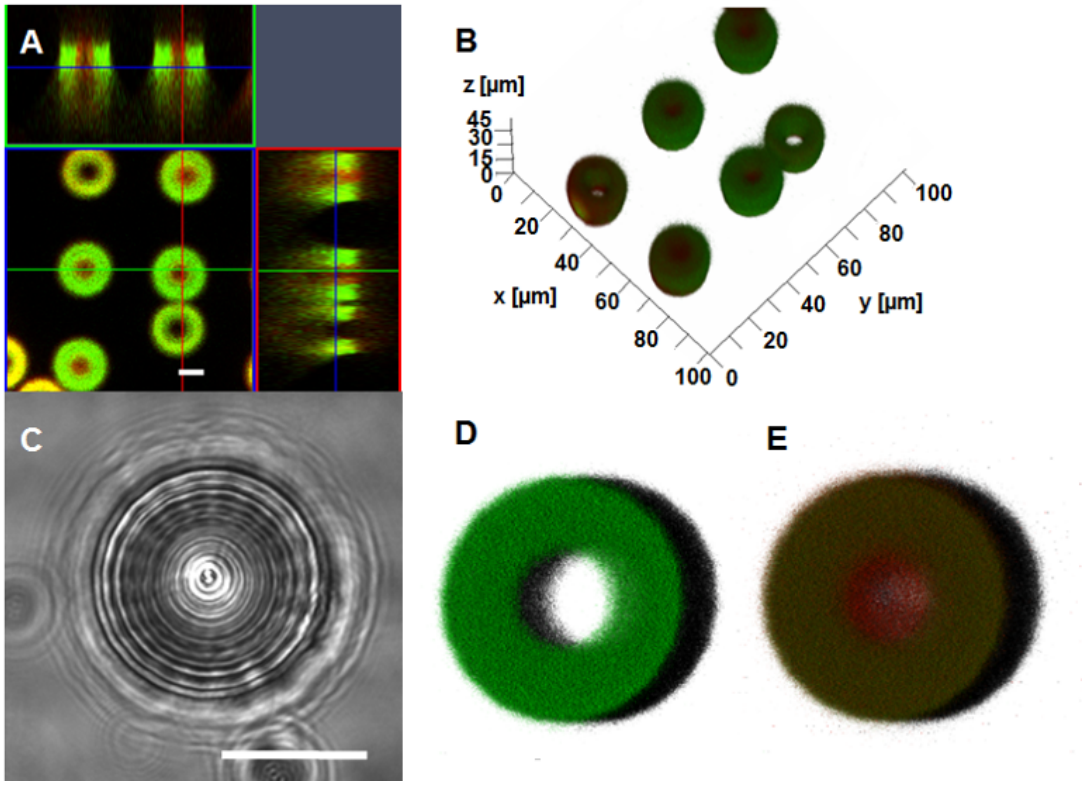


Fig. 5.12 Confocal fluorescence images *Pseudomonas aeruginosa* cultured in hydrogel microarchitectures. All images were taken after after 18 hours incubation at 37°C in TSB media. The fluorescent protein mcherry could be detected in Channel 1 (shown in red). Due to the broad absorption of the photosensitizer rose bengal (460 nm to 600 nm), the structures were visible through both channels (shown in red and green). (A) Cross-section of series of barrel structures showing both channels. (B) 3D projection of z-stack of series of barrel structures showing both channels (C) Bright-field image of intact microstructure (top view). (D) Close-up of intact microstructure showing only channel 1. (E) Close-up of intact microstructure showing both channels. All scale bars=10μm.

the 3D projection in Figure 5.12A), the bacterial colonies seem to be equally distributed throughout the entire volume of the complete microstructures.

5.3.2 Mammalian cell culture

In this work, the biocompatibility of 2PP alginate hydrogels was investigated and the capability to influence the attachment and morphology of human MSCs growing on microstructured alginate hydrogels.

Using topographical features as a tool to influence the adherence and growth of cells is a rapidly spreading approach [142]. A lot of research has demonstrated clear effects of micro- and nano scaled geometrical features on a variety of mammalian cells [143][144]. The underlying structure-function relationships however, remain poorly understood. Advances in microfabrication techniques allow for more efficient and cheaper production of micro-/nano-structured surfaces and facilitate the investigation of their potential to guide cells or induce differentiation and proliferation [131][132][126][145].

To study how microstructured alginate hydrogels affect hMSCs, the short micro-pillar surfaces tested for bacterial experiments were adapted to an 8 μm spacing (Figure 5.1) which was in the range of feature spacings that influenced osteogenic differentiation in a 'Topochip' screening the most [132].

Topochips are chips with thousands of different topographies that were designed on the basis of mathematical algorithms to produce nonbiased and random surface features [146]. Hulshof and co-workers for example, applied such topochips to screen a large library of randomly-selected micro-patterns for their ability to induce osteogenic differentiation of bone marrow-derived MSC's [132]. By screening for the enzyme alkaline phosphatase (ALP) distribution, which served as a biological marker for osteogenic differentiation, they found that feature spacings in the range of approximately 10 μm resulted in a higher amount of APL whereas larger and smaller spacings did not show increased APL.

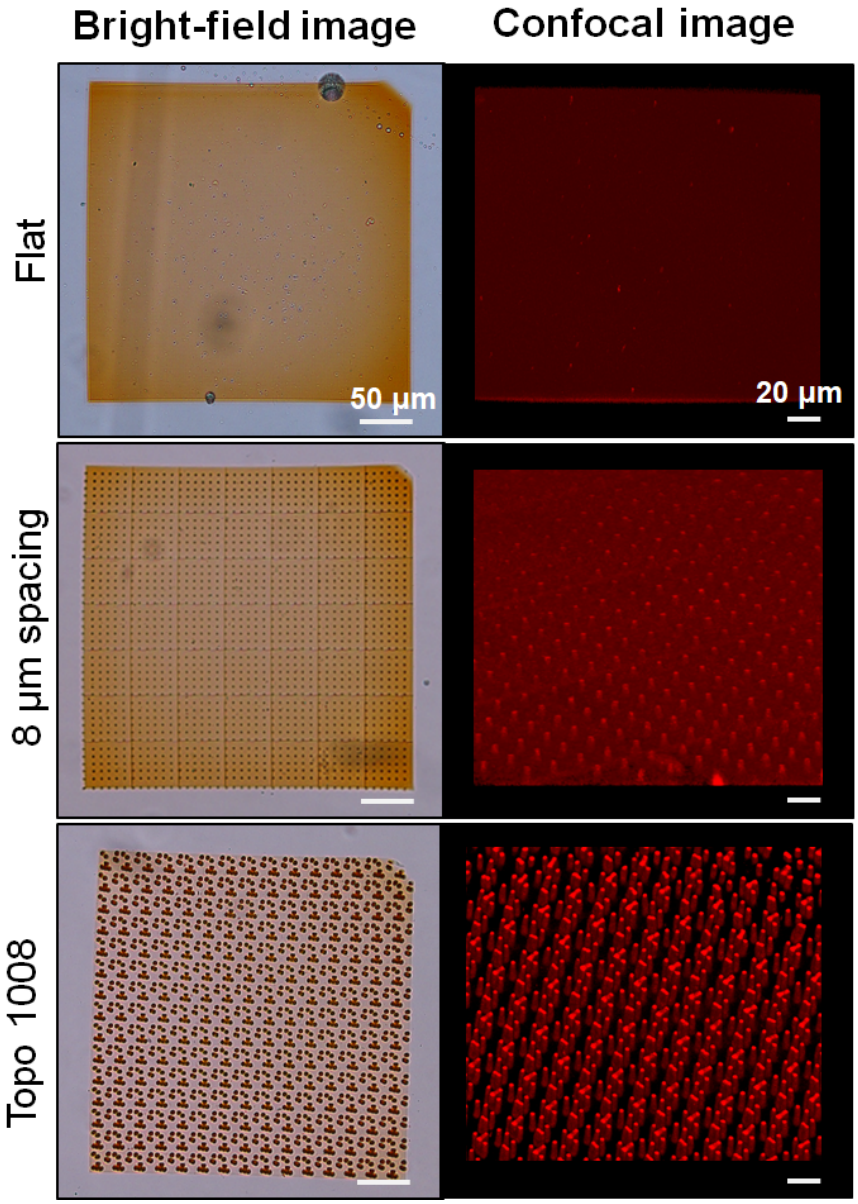


Fig. 5.13 Bright-field (left) and fluorescence images (right) of microstructured alginate hydrogels with various topographies; scale bar left = 50 μm, scale bar right = 20 μm, scale bar right.

An additional CAD file was here designed according to a Topochip design illustrated in Figure 5.2 that was shown to slow down the proliferation of hMSCs in comparison to a flat surface (Vasilevich *et al.*, unpublished data). Using a photoresist consisting of 2% w/v methacrylated alginate and 3 mM P2CK in ddH_2O, alginate hydrogels were fabricated rendering the exact shape of the CAD designs illustrated in Figure 5.1 and Figure 5.2. Figure 5.13 summarizes the printed structures imaged using bright-field microscopy as well as a 3D reconstruction of confocal fluorescence images. Overall, three different topographies were printed on one glass substrate with an area of 300μm x 300μm each. In addition to the short-micro-pillars and the Topounit 1008, a flat alginate hydrogel structure was printed as a control to be compared to microstructured surfaces.

A crucial prerequisite of two-photon fabricated alginate hydrogels for applications in cell culture is that the structures are cytocompatible and concurrently promote attachment to the surfaces. In order to test viability of cells growing on alginate hydrogels, hMSCs were live/dead stained after being cultured for 48 hours on microstructured alginate hydrogels. Different topographies were tested to investigate their influence on the attachment and morphology of hMSCs. This viability test was performed for two biological replicates which showed that the 2PP alginate hydrogels were not toxic for the cells with only very few cells died compared to the cells that were alive and attached to the surface. Figure 5.14 shows the bright field image with the living cells (green) and dead cells (red) for each topography and for both repeats. Most of the dead cells appeared to be on the flat structure which could be due to the cluster of cells that formed more distinctly on flat alginate hydrogels. The cell number per surface was determined by means of image analysis and was more challenging to determine for cell clusters since individual cells could not be identified accurately. The cell numbers summarized in Figure 5.15 therefore, represented only relative cell numbers per surface.

Figure 5.16 shows surface close-ups for one sample and the spreading of the living cells on the alginate surfaces. The flat structure promoted a very distinct aggregation of

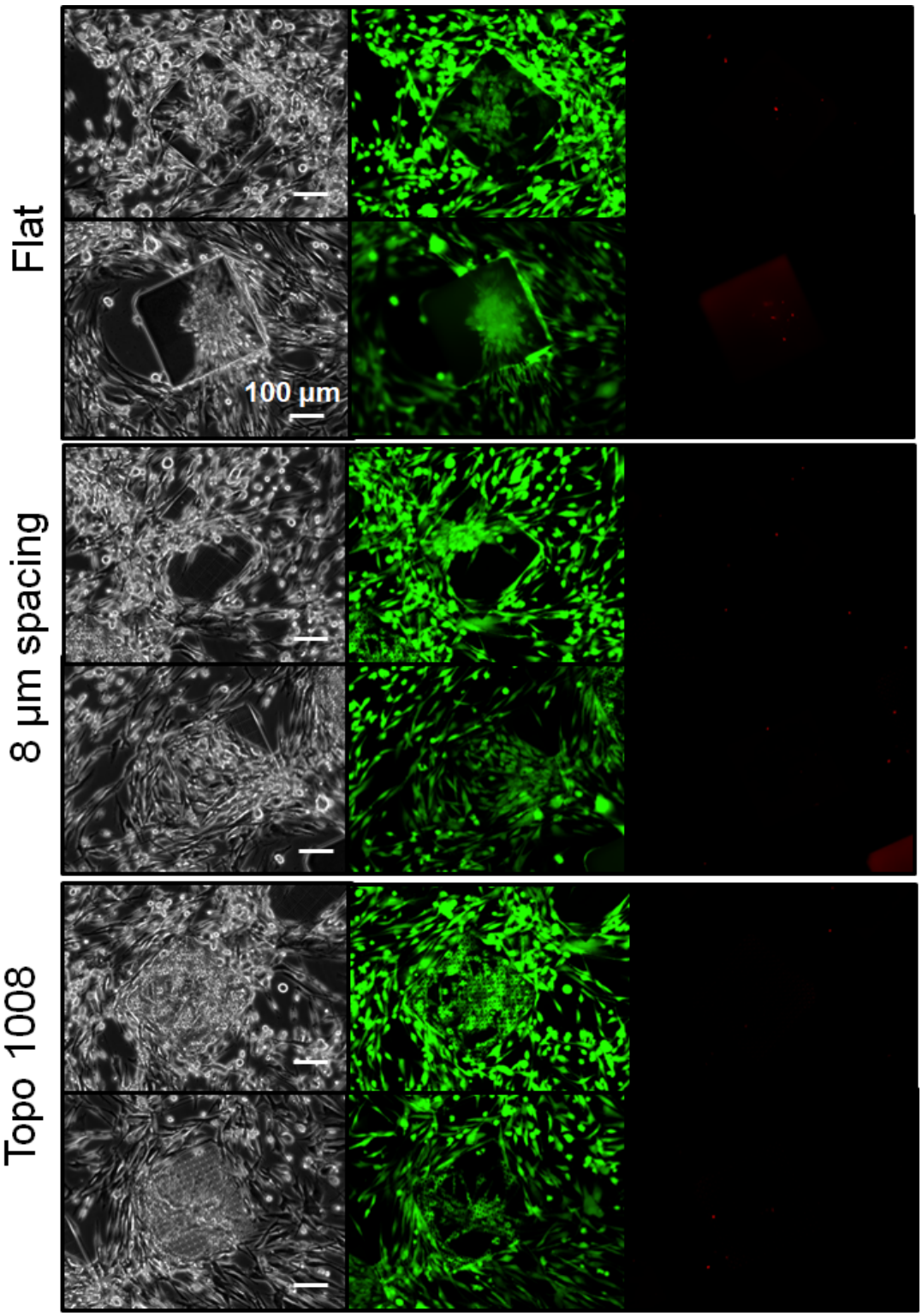


Fig. 5.14 Confocal micrographs of live/dead stained of hMSCs grown for 48 hours on microstructured alginate hydrogels. Two repeats per surface are shown with a bright-field images on the left, the live stained cells in the middle (green) and dead cells on the left (red), scale bar = 100 μm.

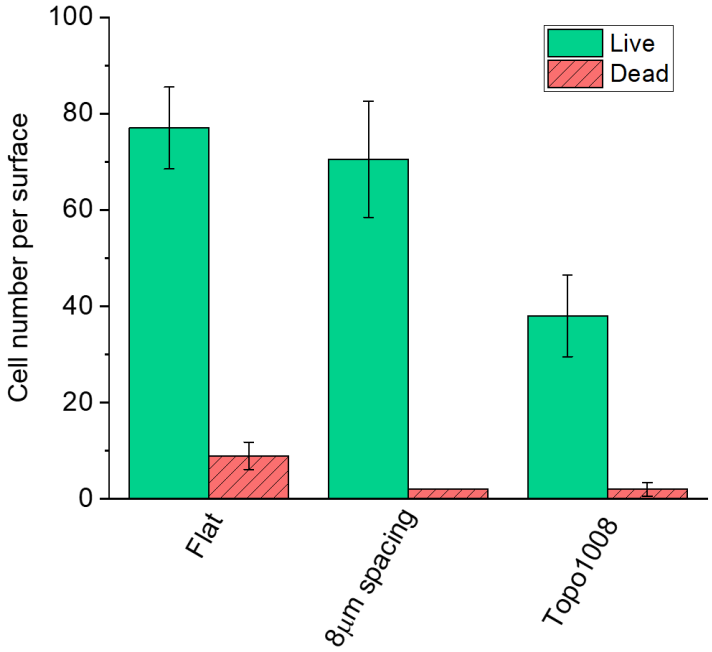


Fig. 5.15 Cell number per surface determined for live/dead stained cells. Error bars represent the standard deviation for two biological repeats.

cells. Partial cluster formation could also be observed for the 8 μm spaced micro-pillars whereas Topo1008 resulted in cells that were more evenly spread out throughout the hydrogel surface (Figure 5.16). The morphology of individual cells growing on the different micro-topographies were further examined using SEM. Figure 5.17 shows representative images for all of the three surfaces as well as cells growing on the glass coverslip. Figure 5.17 includes overview images showing the entire surface on the left and additional magnified images on the right to resolve the cell morphologies in greater detail. Interestingly, more cells appeared spherical on flat alginate hydrogels rather than spread out which indicates less adherent cells [125]. The surfaces with micro-pillars as well as Topo1008 resulted in cells that were spreading similarly to cells that just grew on the glass substrate. Morphological clues relating to particular topographies could not be observed due to too few cells on all samples and would require statistical analysis of several repeats. Further experiments need to be performed to probe these preliminary results. Studying a systematic selection of topographical features and spacings could allow to determine the effect of such structures on the attachment and morphology.

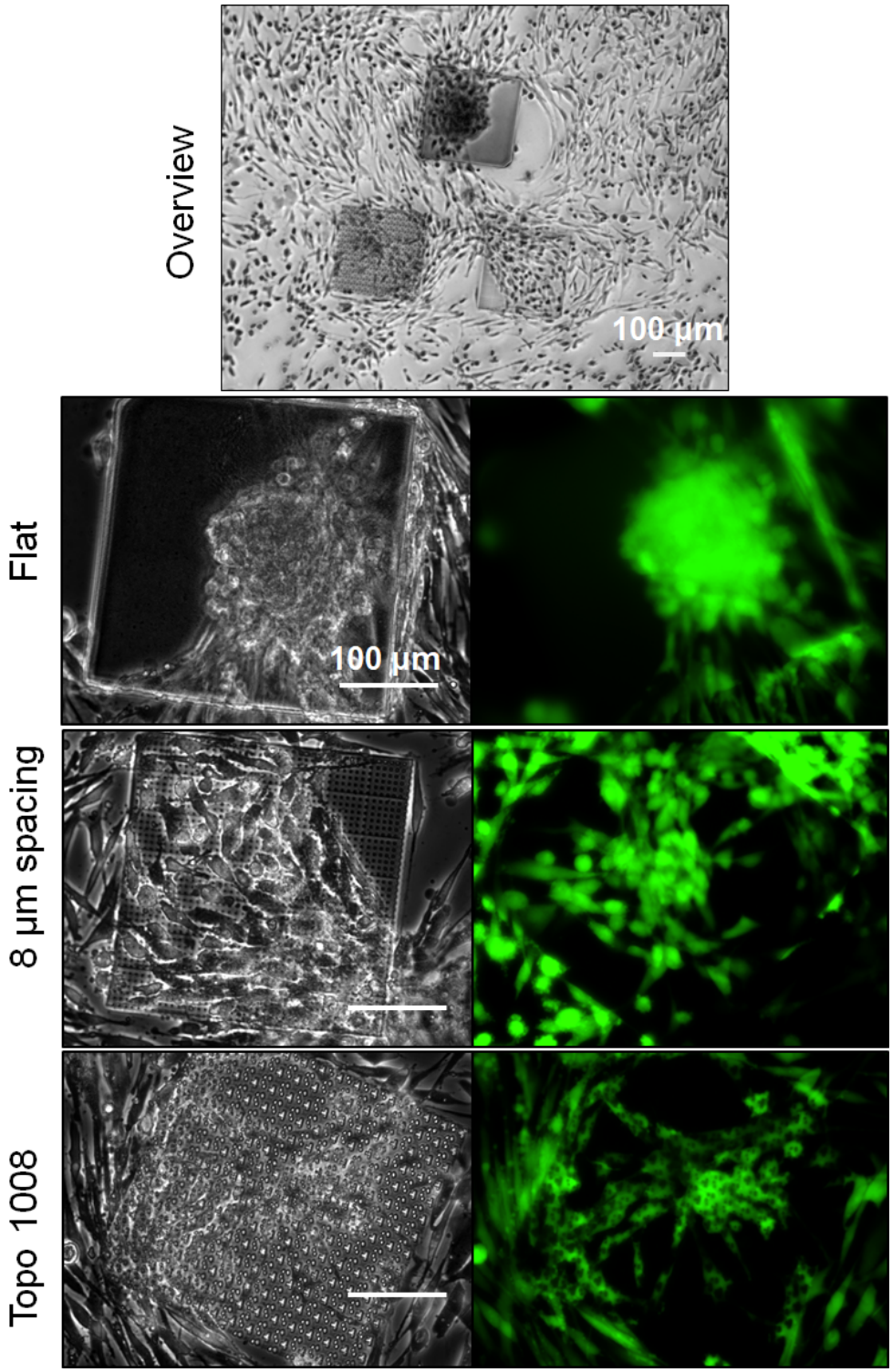


Fig. 5.16 Close-up images of confocal micrograpghs of live stained hMSCs for one representative of each topography that were grown for 48 hours on microstructured alginate hydrogels, scale bar = 100 μm.

Many researchers applied 'blind' high-throughput methods for screening a large set of topographies very quickly, thereby identifying topographies with the desired effect on cells. Poellmann and co-workers for example, used a combinatorial, micro-patterned array of posts with varied shape, width and spacing using polyacrylamide hydrogels and showed that these topographies directed the cell morphology [126]. They found that square patterns were the most influential in their studies and that cells spread on top of the posts for gaps smaller than 10 μm but positioned themselves in a more three-dimensional environment between gaps greater or equal to 10 μm [126]. Abagnale *et al.* demonstrated that varying surface patterns affected the differentiation of MSC's towards specific lineages [131]. Simple geometrical patterns randomly arranged as in 'Topochips' represent another example for a systematic approach to determine topographies that could direct cell behaviour such as growth and differentiation in a high-throughput fashion. To date, there is only a limited understanding of underlying structure activity relationships of topographical patterns and their impact on cell growth. A combined approach of applying high-throughput methods in a first step could help identify relevant topographies which could then be translated into smart hydrogel systems in a second step. Such 2PP alginate hydrogels incorporating micro-patterns would be applied for example, to guide cells or promote particular cell responses.

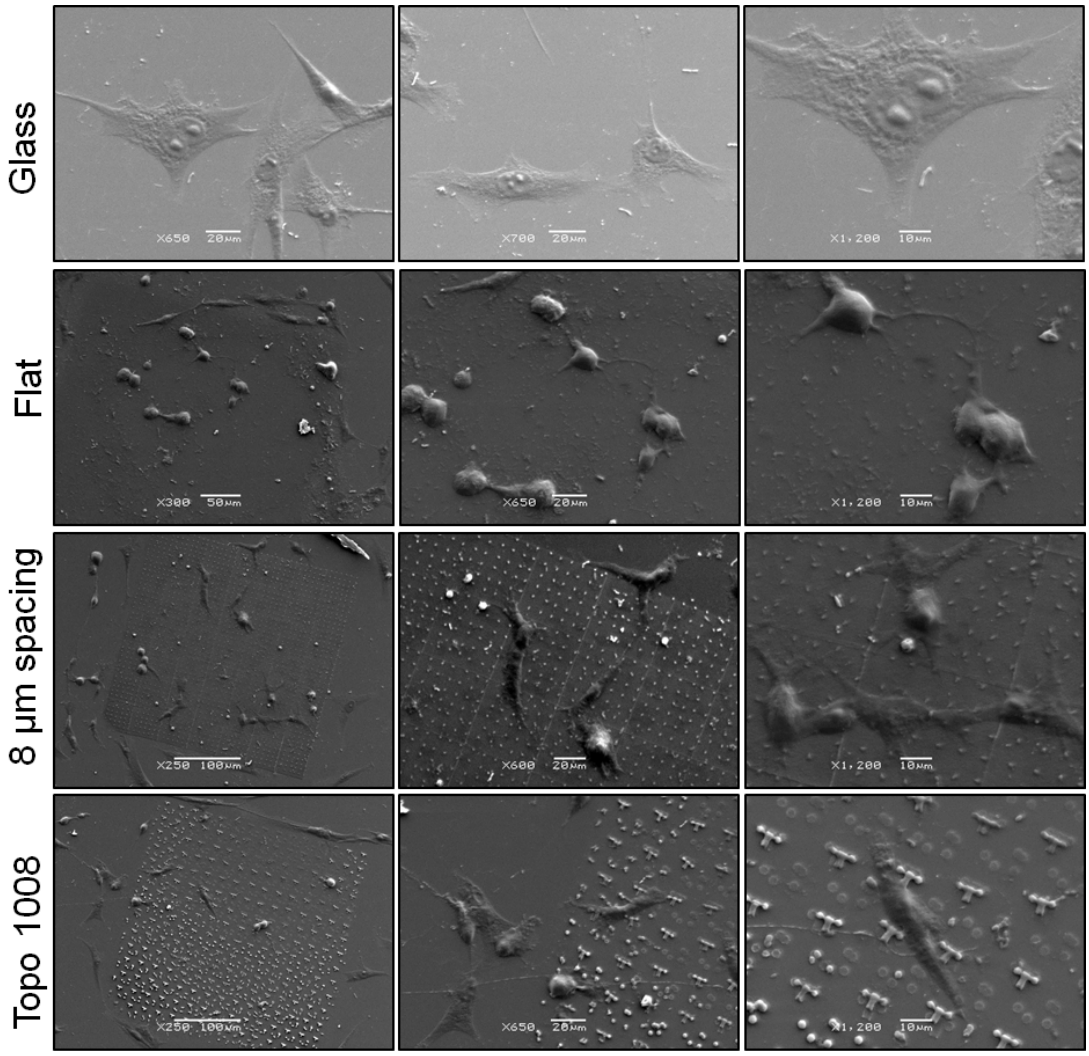


Fig. 5.17 SEM images of hMSCs growing on microstructured alginate hydrogels. Representative images are shown with an overview (left) depicting the entire surface as well as adjacent glass. Two magnifications are shown each (right) to show the individual cells in greater detail.

5.4 Conclusions

- The results presented in this work demonstrate good biocompatibility of two-photon fabricated alginate hydrogel structures for representatives for bacterial species as well as mammalian cells.

- Even non-polymerized photoresist, composed of methacrylated alginate and P2CK was cytocompatible with living bacterial cells which would enable to print in the presence of the cells

- Distinct variations in the number of bacteria attaching to different topographies were observed for both bacterial species demonstrating the efficacy of microstructured surfaces to influence bacterial attachment.

- Microfabricated alginate hydrogels were shown to be cytocompatible and support the growth of human mesenchymal stem cells (hMSCs). First results for hMSCs growing on various microstructured alginate surfaces were evaluated suggesting that micro-topographies could influence the attachment and morphology of MSC's cultured for 48 hours.

- The ability to fabricate alginate hydrogels with precise micron-sized features could be exploited to guide cell growth, promote specific cell morphologies as well as proliferation and differentiation within a more complex hydrogel scaffold for applications in regenerative medicine.

Chapter 6

Conclusion

The overarching goal of this work was to develop a novel and naturally derived photoresist for 2PP of hydrogels that allows to efficiently fabricate biocompatible hydrogels with sub-micron features. Alginate is one of the most prevalent biopolymers used in regenerative medicine. 2PP enables the fabrication of structures with sub-micron feature size, on the scale of single cells. Combining the high resolution of 2PP with the hydrogel properties of alginate, enables control of the mechanical and geometrical properties of artificial micro-environments.

The first aim of optimising the synthesis of methacrylated alginate and establishing a reliable protocol to produce alginates with different degrees of methacrylation was demonstrated in chapter 3. Varying methacrylation degrees could be synthesized and were used in the course of this project to investigate the importance of the number of cross-linking groups in addition to the viscosity and the biopolymer concentration of the photoresist.

Studying the 2PP characteristics of alginate in depth, formed part of the second aim discussed in chapter 4. Highly effective photoresists based on methacrylated alginate could be produced. Optimal 2PP processing parameters for alginate photoresists were determined based on a systematic study of varying alginate concentrations, degree of

functionalisation with cross-linker groups, and the laser power dosage. Concentrations of at least two weight percent of alginate should be used to fabricate stable hydrogel structures. Especially higher alginate concentrations showed crucial improvement in structural integrity of 3D hydrogels, which was determined through the deformation ratio of the hydrogels. The results suggest that increasing concentrations are improving the polymerization efficiency likely due to increased viscosities. Alginate photoresists with more functional groups resulted in decreased polymerization thresholds P_{th} and increased damage thresholds D_{th}, thereby maximising the dynamic power ranges. An unprecedented resolution for alginate hydrogels was demonstrated with minimal linewidths down to 175 nm for 2% w/v Alg-MA30.

Chapter 5 showed that the microfabricated alginate hydrogels were cytocompatible with bacterial and mammalian cells incubated for 18 hours and 48 hours, respectively. A representative for Gram-negative and a Gram-positive bacteria grown on a set of different micro-topographies resulted in distinct differences of bacterial attachment which could be exploited to prevent bacterial growth. The microfabricated alginate hydrogels were further shown to support the growth of human mesenchymal stem cells (hMSCs) with first results indicating that microstructures influence the attachment and morphology of hMSCs.

Efficient two-photon polymerization of alginate hydrogels with unprecedented resolution could be demonstrated in this thesis which were shown to be cytocompatible.
2PP of alginate allows for precisely engineering artificial cell environments which may enable novel tissue engineering strategies and microbiology investigations. The increased understanding of the variables influencing 2PP of alginate will inform and accelerate the development of other novel water-based photoresists for 2PP. Further development in the technology of automated two-photon set-ups will advance and promote the use of microfabricated hydrogels in biomedicine.

References

[1] W. E. Hennink and C. F. van Nostrum. Novel crosslinking methods to design hydrogels. *Advanced Drug Delivery Reviews*, 64(SUPPL.):223–236, 2012.

[2] O Wichterle and D Lim. Hydrophilic gels for biological use. *Nature*, 185(4706):117, 1960.

[3] O Wichterle and D Lim. Process for producing shaped articles from three-dimensional hydrophilic high polymers, March 28 1961. US Patent 2,976,576.

[4] JC Wheeler, JA Woods, MJ Cox, RW Cantrell, FH Watkins, and RF Edlich. Evolution of hydrogel polymers as contact lenses, surface coatings, dressings, and drug delivery systems. *Journal of long-term effects of medical implants*, 6(3-4):207–217, 1996.

[5] Kuen Yong Lee and David J Mooney. Hydrogels for tissue engineering. *Chemical reviews*, 101(7):1869–1880, 2001.

[6] Enrica Caló and Vitaliy V Khutoryanskiy. Biomedical applications of hydrogels: A review of patents and commercial products. *European Polymer Journal*, 65:252–267, 2015.

[7] Adrianne M Rosales and Kristi S Anseth. The design of reversible hydrogels to capture extracellular matrix dynamics. *Nature Reviews Materials*, 1(2):15012, 2016.

[8] Ellis Gruber. Clinical experience with the hydrophilic contact lens. *American journal of ophthalmology*, 70(5):833–842, 1970.

[9] Jeanie L Drury and David J Mooney. Hydrogels for tissue engineering: scaffold design variables and applications. *Biomaterials*, 24(24):4337–4351, 2003.

[10] Junmin Zhu. Bioactive modification of poly (ethylene glycol) hydrogels for tissue engineering. *Biomaterials*, 31(17):4639–4656, 2010.

[11] Marine Verhulsel, Maéva Vignes, Stéphanie Descroix, Laurent Malaquin, Danijela M Vignjevic, and Jean-Louis Viovy. A review of microfabrication and hydrogel engineering for micro-organs on chips. *Biomaterials*, 35(6):1816–1832, 2014.

[12] Mina Suh, Deborah Proctor, Grace Chappell, Julia Rager, Chad Thompson, Susan Borghoff, Lavorgie Finch, Robert Ellis-Hutchings, and Karin Wiench. A review of the genotoxic, mutagenic, and carcinogenic potentials of several lower acrylates. *Toxicology*, 402:50–67, 2018.

[13] Elyssa L Monzack, Karien J Rodriguez, Chloe M McCoy, Xiaoxiao Gu, and Kristyn S Masters. Natural materials in tissue engineering applications. In *Biomaterials for Tissue Engineering Applications*, pages 209–241. Springer, 2011.

[14] Lian Cen, WEI Liu, LEI Cui, Wenjie Zhang, and Yilin Cao. Collagen tissue engineering: development of novel biomaterials and applications. *Pediatric research*, 63(5):492, 2008.

[15] S. Van Vlierberghe, P. Dubruel, and E. Schacht. Biopolymer-based hydrogels as scaffolds for tissue engineering applications: A review. *Biomacromolecules*, 12(5):1387–1408, 2011.

[16] Xiaohong Wang, Qiang Ao, Xiaohong Tian, Jun Fan, Hao Tong, Weijian Hou, and Shuling Bai. Gelatin-based hydrogels for organ 3d bioprinting. *Polymers*, 9(9):401, 2017.

[17] Susan M Tosh and Alejandro G Marangoni. Determination of the maximum gelation temperature in gelatin gels. *Applied Physics Letters*, 84(21):4242–4244, 2004.

[18] Jason W. Nichol, Sandeep T. Koshy, Hojae Bae, Chang M. Hwang, Seda Yamanlar, and Ali Khademhosseini. Cell-laden microengineered gelatin methacrylate hydrogels. *Biomaterials*, 31(21):5536–5544, 2010.

[19] a I Van Den Bulcke, B Bogdanov, N De Rooze, E H Schacht, M Cornelissen, and H Berghmans. Structural and rheological properties of methacrylamide modified gelatin hydrogels. *Biomacromolecules*, 1(1):31–38, 2000.

[20] Lena Möller, Andreas Krause, Julia Dahlmann, Ina Gruh, Andreas Kirschning, and Gerald Dräger. Preparation and evaluation of hydrogel-composites from methacrylated hyaluronic acid, alginate, and gelatin for tissue engineering. *The International journal of artificial organs*, 34(2):93–102, 2011.

[21] M Enamul Hoque, Tamrin Nuge, Tshai Kim Yeow, Norshariza Nordin, and RGSV Prasad. Gelatin based scaffolds for tissue engineering-a review. *Polymers Research Journal*, 9(1):15, 2015.

[22] Jaepyoung Cho, Marie-Claude Heuzey, André Bégin, and Pierre J Carreau. Physical gelation of chitosan in the presence of β-glycerophosphate: the effect of temperature. *Biomacromolecules*, 6(6):3267–3275, 2005.

[23] JBLBP Necas, L Bartosikova, P Brauner, J Kolar, et al. Hyaluronic acid (hyaluronan): a review. *Veterinarni medicina*, 53(8):397–411, 2008.

[24] Maurice N Collins and Colin Birkinshaw. Hyaluronic acid based scaffolds for tissue engineering—a review. *Carbohydrate polymers*, 92(2):1262–1279, 2013.

[25] Jason A Burdick and Glenn D Prestwich. Hyaluronic acid hydrogels for biomedical applications. *Advanced materials*, 23(12):H41–H56, 2011.

[26] Sidi A. Bencherif, Abiraman Srinivasan, Ferenc Horkay, Jeffrey O. Hollinger, Krzysztof Matyjaszewski, and Newell R. Washburn. Influence of the degree of methacrylation on hyaluronic acid hydrogels properties. *Biomaterials*, 29(12):1739–1749, 2008.

[27] Siddhesh N. Pawar and Kevin J. Edgar. Alginate derivatization: A review of chemistry, properties and applications. *Biomaterials*, 33(11):3279–3305, 2012.

[28] Kuen Yong Lee and David J. Mooney. Alginate: Properties and biomedical applications. *Progress in Polymer Science (Oxford)*, 37(1):106–126, 2012.

[29] Arturo J. Vegas, Omid Veiseh, Joshua C. Doloff, Minglin Ma, Hok Hei Tam, Kaitlin Bratlie, Jie Li, Andrew R. Bader, Erin Langan, Karsten Olejnik, Patrick Fenton, Jeon Woong Kang, Jennifer Hollister-Locke, Matthew A. Bochenek, Alan Chiu, Sean Siebert, Katherine Tang, Siddharth Jhunjhunwala, Stephanie Aresta-Dasilva, Nimit Dholakia, Raj Thakrar, Thema Vietti, Michael Chen, Josh Cohen, Karolina Siniakowicz, Meirigeng Qi, James McGarrigle, Stephen Lyle, David M. Harlan, Dale L. Greiner, Jose Oberholzer, Gordon C. Weir, Robert Langer, and Daniel G. Anderson. Supplemental Information - Combinatorial hydrogel library enables identification of materials that mitigate the foreign body response in primates. *Nature biotechnology*, 34(3):345–352, 2016.

[30] Oju Jeon, Caitlin Powell, Shaoly M. Ahmed, and Eben Alsberg. Biodegradable, Photocrosslinked Alginate Hydrogels with Independently Tailorable Physical Properties and Cell Adhesivity. *Tissue Engineering Part A*, 16(9):2915–2925, 2010.

[31] Ali Khademhosseini, George Eng, Judy Yeh, Junji Fukuda, James Blumling III, Robert Langer, and Jason A Burdick. Micromolding of photocrosslinkable hyaluronic acid for cell encapsulation and entrapment. *Journal of Biomedical Materials Research Part A: An Official Journal of The Society for Biomaterials, The Japanese Society for Biomaterials, and The Australian Society for Biomaterials and the Korean Society for Biomaterials*, 79(3):522–532, 2006.

[32] Bethany C Gross, Jayda L Erkal, Sarah Y Lockwood, Chengpeng Chen, and Dana M Spence. Evaluation of 3d printing and its potential impact on biotechnology and the chemical sciences, 2014.

[33] Charles W Hull. Apparatus for production of three-dimensional objects by stereolithography, March 11 1986. US Patent 4,575,330.

[34] Thomas Billiet, Mieke Vandenhaute, Jorg Schelfhout, Sandra Van Vlierberghe, and Peter Dubruel. A review of trends and limitations in hydrogel-rapid prototyping for tissue engineering. *Biomaterials*, 33(26):6020–6041, 2012.

[35] Alberto Piaggesi, Severin Låuchli, Franco Bassetto, Thomas Biedermann, Alexandra Marques, Bijan Najafi, Ilaria Palla, Carlotta Scarpa, Diane Seimetz, Isotta Triulzi, et al. Advanced therapies in wound management: cell and tissue based therapies, physical and bio-physical therapies smart and it based technologies. *Journal of wound care*, 27(Sup6a):S1–S137, 2018.

[36] Paul Calvert. Inkjet printing for materials and devices. *Chemistry of materials*, 13(10):3299–3305, 2001.

[37] Brian Derby. Inkjet printing of functional and structural materials: fluid property requirements, feature stability, and resolution. *Annual Review of Materials Research*, 40:395–414, 2010.

[38] Anand Doraiswamy, Timothy M Dunaway, Jonathan J Wilker, and Roger J Narayan. Inkjet printing of bioadhesives. *Journal of Biomedical Materials Research Part B: Applied Biomaterials: An Official Journal of The Society for Biomaterials, The Japanese Society for Biomaterials, and The Australian Society for Biomaterials and the Korean Society for Biomaterials*, 89(1):28–35, 2009.

[39] Tao Xu, Weixin Zhao, Jian-Ming Zhu, Mohammad Z Albanna, James J Yoo, and Anthony Atala. Complex heterogeneous tissue constructs containing multiple cell types prepared by inkjet printing technology. *Biomaterials*, 34(1):130–139, 2013.

[40] Ralf Zimmermann, Christoph Hentschel, Felix Schrön, Denise Moedder, Teresa Büttner, Passant Atallah, Thomas Wegener, Thomas Gehring, Steffen Howitz, Uwe Freudenberg, et al. High resolution bioprinting of multi-component hydrogels. *Biofabrication*, 2019.

[41] Jyrki Korpela, Anne Kokkari, Harri Korhonen, Minna Malin, Timo Närhi, and Jukka Seppälä. Biodegradable and bioactive porous scaffold structures prepared using fused deposition modeling. *Journal of Biomedical Materials Research Part B: Applied Biomaterials*, 101(4):610–619, 2013.

[42] Li Liu, Zhuo Xiong, Yongnian Yan, Renji Zhang, Xiaohong Wang, and Le Jin. Multinozzle low-temperature deposition system for construction of gradient tissue engineering scaffolds. *Journal of Biomedical Materials Research Part B: Applied Biomaterials: An Official Journal of The Society for Biomaterials, The Japanese Society for Biomaterials, and The Australian Society for Biomaterials and the Korean Society for Biomaterials*, 88(1):254–263, 2009.

[43] Ferry PW Melchels, Jan Feijen, and Dirk W Grijpma. A review on stereolithography and its applications in biomedical engineering. *Biomaterials*, 31(24):6121–6130, 2010.

[44] John T Fourkas. *Chapter 1.3 - Fundamentals of Two-Photon Fabrication*. Elsevier Inc., 2016.

[45] Ping Yun Zhang, Zhen Liang Xu, Hu Yang, Yong Ming Wei, Wen Zhi Wu, Linjie Li, John T. Fourkas, E. S. Jönsson, T. Y. Lee, K. Viswanathan, C. E. Hoyle, T. M. Roper, C. A. Guymon, C. Nason, I. V. Khudyakov, Ewa Andrzejewska, Sergio O Martinez-Chapa, Arnoldo Salazar, Marc J Madou, B Husár, M Hatzenbichler, V Mironov, R Liska, J Stampfl, A Ovsianikov, Markus Woehrmann Additional, Michael Toepper, Markus Woehrmann, Michael Toepper, Jean-pierre Fouassier, Fabrice Morlet-savary, Jacques Lalevée, Xavier Allonas, and Nancy L Oleinick. *Chapter 2 – Free Radical Photopolymerization of Multifunctional Monomers*, volume 52. Elsevier Inc., 2016.

[46] Xiaoqin Zhou, Yihong Hou, and Jieqiong Lin. A review on the processing accuracy of two-photon polymerization. *AIP Advances*, 5(3):030701, 2015.

[47] Hiroaki Nishiyama and Yoshinori Hirat. Femtosecond Laser Nonlinear Lithography. *Lithography*, (February), 2010.

[48] Maria Göppert-Mayer. Über elementarakte mit zwei quantensprüngen. *Annalen der Physik*, 401(3):273–294, 1931.

[49] Winfried Denk and Karel Svoboda. Photon upmanship: why multiphoton imaging is more than a gimmick. *Neuron*, 18(3):351–357, 1997.

[50] Winfried Denk, James H Strickler, and Watt W Webb. Two-photon laser scanning fluorescence microscopy. *Science*, 248(4951):73–76, 1990.

[51] S Maruo, O Nakamura, and S Kawata. Three-dimensional microfabrication with two-photon-absorbed photopolymerization. *Optics letters*, 22(2):132–134, 1997.

[52] Jonathan D Pitts, Paul J Campagnola, Gary A Epling, and Steven L Goodman. Submicron Multiphoton Free-Form Fabrication of Proteins and Polymers: Studies of Reaction Efficiencies and Applications in Sustained Release. pages 1514–1523, 2000.

[53] Ewa Andrzejewska. Chapter 2 - free radical photopolymerization of multifunctional monomers. In Tommaso Baldacchini, editor, *Three-Dimensional Microfabrication Using Two-photon Polymerization*, Micro and Nano Technologies, pages 62 – 81. William Andrew Publishing, Oxford, 2016.

[54] Rong Jin and Pieter J Dijkstra. Hydrogels for Tissue Engineering Applications. 101(7):203–225, 2010.

[55] Chris Xu and Watt W Webb. Measurement of two-photon excitation cross sections of molecular fluorophores with data from 690 to 1050 nm. *JOSA B*, 13(3):481–491, 1996.

[56] Brian H Cumpston, Sundaravel P Ananthavel, Stephen Barlow, Daniel L Dyer, Jeffrey E Ehrlich, Lael L Erskine, Ahmed A Heikal, Stephen M Kuebler, I-Y Sandy Lee, Dianne McCord-Maughon, et al. Two-photon polymerization initiators for three-dimensional optical data storage and microfabrication. *Nature*, 398(6722):51, 1999.

[57] Markus Lunzer, Liyang Shi, Orestis G Andriotis, Peter Gruber, Marica Markovic, Philipp J Thurner, Dmitri Ossipov, Robert Liska, and Aleksandr Ovsianikov. A modular approach to sensitized two-photon patterning of photodegradable hydrogels. *Angewandte Chemie*, 130(46):15342–15347, 2018.

[58] Marius Albota, David Beljonne, Jean-Luc Brédas, Jeffrey E Ehrlich, Jia-Ying Fu, Ahmed A Heikal, Samuel E Hess, Thierry Kogej, Michael D Levin, Seth R Marder, et al. Design of organic molecules with large two-photon absorption cross sections. *Science*, 281(5383):1653–1656, 1998.

[59] Christopher LaFratta and Tommaso Baldacchini. Two-photon polymerization metrology: Characterization methods of mechanisms and microstructures. *Micromachines*, 8(4):101, 2017.

[60] Jonathan B Mueller, Joachim Fischer, Yatin J Mange, Thomas Nann, and Martin Wegener. In-situ local temperature measurement during three-dimensional direct laser writing. *Applied Physics Letters*, 103(12):123107, 2013.

[61] Jonathan B Mueller, Joachim Fischer, Frederik Mayer, Muamer Kadic, and Martin Wegener. Polymerization kinetics in three-dimensional direct laser writing. *Advanced Materials*, 26(38):6566–6571, 2014.

[62] Fariba Ganji, Farahani S Vasheghani, and FARAAHANI E VASHEGHANI. Theoretical description of hydrogel swelling: a review. *Iranian Polymer Journal*, 19(5):375–398, 2006.

[63] Jodi L. Connell, Jiyeon Kim, Jason B. Shear, Allen J. Bard, and Marvin Whiteley. Real-time monitoring of quorum sensing in 3D-printed bacterial aggregates using scanning electrochemical microscopy. *Proceedings of the National Academy of Sciences of the United States of America*, 111(51):18255–60, 2014.

[64] Hong Bo Sun and Satoshi Kawata. Two-photon photopolymerization and 3D lithographic microfabrication. *Advances in Polymer Science*, 170:169–273, 2004.

[65] Aleksandr Ovsianikov, Severin M??hleder, Jan Torgersen, Zhiquan Li, Xiao Hua Qin, Sandra Van Vlierberghe, Peter Dubruel, Wolfgang Holnthoner, Heinz Redl, Robert Liska, and J??rgen Stampfl. Laser photofabrication of cell-containing hydrogel constructs. *Langmuir*, 30(13):3787–3794, 2014.

[66] Aleksandr Ovsianikov, Andrea Deiwick, Sandra Van Vlierberghe, Peter Dubruel, Lena Möller, Gerald Drager, and Boris Chichkov. Laser fabrication of three-dimensional CAD scaffolds from photosensitive gelatin for applications in tissue engineering. *Biomacromolecules*, 12(4):851–858, 2011.

[67] Jasper Van Hoorick, Peter Gruber, Marica Markovic, Maximilian Tromayer, Ju Van Erps, and Sandra Van Vlierberghe. Cross-Linkable Gelatins with Superior Mechanical Properties Through Carboxylic Acid Modi fi cation: Increasing the Two-Photon Polymerization Potential. pages 3260–3272, 2017.

[68] Zhiquan Li, Niklas Pucher, Klaus Cicha, Jan Torgersen, Samuel C Ligon, Aliasghar Ajami, Wolfgang Husinsky, Arnulf Rosspeintner, Eric Vauthey, Sergej Naumov, Tom Scherzer, and Robert Liska. A Straightforward Synthesis and Structure Activity Relationship of Highly E ffi cient Initiators for Two-Photon Polymerization. 2012.

[69] Maximilian Tromayer, Peter Gruber, Marica Markovic, Arnulf Rosspeintner, Eric Vauthey, Heinz Redl, Aleksandr Ovsianikov, and Robert Liska. A biocompatible macromolecular two-photon initiator based on hyaluronan. *Polym. Chem.*, 2016.

[70] Maximilian Tromayer, Agnes Dobos, Peter Gruber, Aliasghar Ajami, Roman Dedic, Aleksandr Ovsianikov, and Robert Liska. Polymer Chemistry A biocompatible diazosulfonate initiator for direct encapsulation of human stem cells via. *Polymer Chemistry*, 2018.

[71] Yong-Chao Zheng, Yuan-Yuan Zhao, Mei-Ling Zheng, Shi-Lu Chen, Jie Liu, Feng Jin, Xian-Zi Dong, Zhen-Sheng Zhao, and Xuan-Ming Duan. Cucurbit [7] uril-carbazole two-photon photoinitiators for the fabrication of biocompatible three-dimensional hydrogel scaffolds by laser direct writing in aqueous solutions. *ACS applied materials & interfaces*, 11(2):1782–1789, 2019.

[72] Jan Torgersen, Xiao Hua Qin, Zhiquan Li, Aleksandr Ovsianikov, Robert Liska, and Jürgen Stampfl. Hydrogels for two-photon polymerization: A toolbox for mimicking the extracellular matrix. *Advanced Functional Materials*, 23(36):4542–4554, 2013.

[73] A Ovsianikov, M Malinauskas, S Schlie, B Chichkov, S Gittard, R Narayan, M Löbler, K Sternberg, K-P Schmitz, and A Haverich. Three-dimensional laser micro-and nano-structuring of acrylated poly (ethylene glycol) materials and evaluation of their cytoxicity for tissue engineering applications. *Acta biomaterialia*, 7(3):967–974, 2011.

[74] Shalin J Jhaveri, Jesse D McMullen, Rint Sijbesma, Loon-Seng Tan, Warren Zipfel, and Christopher K Ober. Direct three-dimensional microfabrication of hydrogels via two-photon lithography in aqueous solution. *Chemistry of materials*, 21(10):2003–2006, 2009.

[75] Aleksandr Ovsianikov, M Gruene, M Pflaum, L Koch, F Maiorana, M Wilhelmi, A Haverich, and Boris Chichkov. Laser printing of cells into 3D scaffolds. *Biofabrication*, 2(1):014104, 2010.

[76] Mark W Tibbitt, April M Kloxin, Kiran U Dyamenahalli, and Kristi S Anseth. Controlled two-photon photodegradation of peg hydrogels to study and manipulate subcellular interactions on soft materials. *Soft Matter*, 6(20):5100–5108, 2010.

[77] Elli Käpylä, Tomáš Sedlačík, Dogu Baran Aydogan, Jouko Viitanen, František Rypáček, and Minna Kellomäki. Direct laser writing of synthetic poly (amino acid) hydrogels and poly (ethylene glycol) diacrylates by two-photon polymerization. *Materials Science and Engineering: C*, 43:280–289, 2014.

[78] Guoqiang Liu, Yongsan Li, Lei Yang, Yen Wei, Xing Wang, Zhiming Wang, and Lei Tao. Cytotoxicity study of polyethylene glycol derivatives. *RSC Advances*, 7(30):18252–18259, 2017.

[79] Daniela Serien and Shoji Takeuchi. Fabrication of submicron proteinaceous structures by direct laser writing. *Applied Physics Letters*, 107(1):013702, 2015.

[80] Shuxin Wei, Jie Liu, Yuanyuan Zhao, Tingbin Zhang, Meiling Zheng, Feng Jin, Xianzi Dong, Jinfeng Xing, and Xuanming Duan. Protein-based 3d microstructures with controllable morphology and ph-responsive properties. *ACS applied materials & interfaces*, 9(48):42247–42257, 2017.

[81] Chee Leng Lay, Yih Hong Lee, Mian Rong Lee, In Yee Phang, and Xing Yi Ling. Formulating an Ideal Protein Photoresist for Fabricating Dynamic Microstructures with High Aspect Ratios and Uniform Responsiveness. *ACS Applied Materials and Interfaces*, 8(12):8145–8153, 2016.

[82] Jodi L Connell, Aimee K Wessel, and Matthew R Parsek. er Traps"Probing Prokaryotic Social Behaviors with Bacterial "Lobst. c(4):1–8, 2010.

[83] Jodi L Connell, Eric T Ritschdorff, Marvin Whiteley, and Jason B Shear. 3D printing of microscopic bacterial communities. *Proceedings of the National Academy of Sciences of the United States of America*, 110(46):18380–5, 2013.

[84] Jodi L Connell, Eric T Ritschdorff, and Jason B Shear. 3D Printing of Photoresponsive Biomaterials for Control of Bacterial Microenvironments. *Analytical chemistry*, 2016.

[85] Olga Kufelt, Ayman El-tamer, Camilla Sehring, Sabrina Schlie-wolter, and Boris N Chichkov. Hyaluronic Acid Based Materials for Sca ff olding via Two-Photon Polymerization. *Biomacromolecules*, 15:650–659, 2014.

[86] Claudia Loebel, Nicolas Broguiere, Mauro Alini, Marcy Zenobi-Wong, and David Eglin. Microfabrication of photo-cross-linked hyaluronan hydrogels by single- and two-photon tyramine oxidation. *Biomacromolecules*, 16(9):2624–2630, 2015.

[87] Olga Kufelt, Ayman El-Tamer, Camilla Sehring, Marita Meißner, Sabrina Schlie-Wolter, and Boris N. Chichkov. Water-soluble photopolymerizable chitosan hydrogels for biofabrication via two-photon polymerization. *Acta Biomaterialia*, 18:186–195, 2015.

[88] George M Abouna. Organ shortage crisis: problems and possible solutions. In *Transplantation proceedings*, volume 40, pages 34–38. Elsevier, 2008.

[89] Dongeun Huh, Geraldine A Hamilton, and Donald E Ingber. From 3d cell culture to organs-on-chips. *Trends in cell biology*, 21(12):745–754, 2011.

[90] Hong-Bo Sun, Makoto Maeda, Kenji Takada, James WM Chon, Min Gu, and Satoshi Kawata. Experimental investigation of single voxels for laser nanofabrication via two-photon photopolymerization. *Applied physics letters*, 83(5):819–821, 2003.

[91] Catia Cilene Nass Sebrao, Arandi Ginane Bezerra Jr, Paulo Henrique Condeixa de França, Leslie Ecker Ferreira, and Vania Portela Ditzel Westphalen. Comparison of the efficiency of rose bengal and methylene blue as photosensitizers in photodynamic therapy techniques for enterococcus faecalis inactivation. *Photomedicine and laser surgery*, 35(1):18–23, 2017.

[92] Suraj Deshmukh, Matthew T Bishop, Daniel Dermody, Laura Dietsche, Tzu-Chi Kuo, Melissa Mushrush, Keith Harris, Jonathan Zieman, Paul Morabito, Brian Orvosh, and Don Patrick. A novel high-throughput viscometer. *ACS Combinatorial Science*, 103(18):405–423, 2016.

[93] Zuoxin Zhou, Laura Ruiz Cantu, Xuesheng Chen, Morgan R. Alexander, Clive J. Roberts, Richard Hague, Christopher Tuck, Derek Irvine, and Ricky Wildman. High-throughput determination of printability for three-dimensional inkjet formulations. *Manuskript submitted*, 2019.

[94] Frank Burmeister, Sönke Steenhusen, Ruth Houbertz, Uwe D Zeitner, Stefan Nolte, and Andreas Tünnermann. Materials and technologies for fabrication of three-dimensional microstructures with sub-100 nm feature sizes by two-photon polymerization. *Journal of Laser Applications*, 24(4):042014, 2012.

[95] Li Jia Jiang, Yun Shen Zhou, Wei Xiong, Yang Gao, Xi Huang, Lan Jiang, Tommaso Baldacchini, Jean-Francois Silvain, and Yong Feng Lu. Two-photon polymerization: investigation of chemical and mechanical properties of resins using raman microspectroscopy. *Optics letters*, 39(10):3034–3037, 2014.

[96] Xiao-Hua Qin, Peter Gruber, Marica Markovic, Birgit Plochberger, Enrico Klotzsch, Jürgen Stampfl, Aleksandr Ovsianikov, and Robert Liska. Enzymatic synthesis of hyaluronic acid vinyl esters for two-photon microfabrication of biocompatible and biodegradable hydrogel constructs. *Polym. Chem.*, 5(22):6523–6533, 2014.

[97] A. I. Chou, S. O. Akintoye, and S. B. Nicoll. Photo-crosslinked alginate hydrogels support enhanced matrix accumulation by nucleus pulposus cells in vivo. *Osteoarthritis and Cartilage*, 17(10):1377–1384, 2009.

[98] Rajiv M. Desai, Sandeep T. Koshy, Scott A. Hilderbrand, David J. Mooney, and Neel S. Joshi. Versatile click alginate hydrogels crosslinked via tetrazine-norbornene chemistry. *Biomaterials*, 50(1):30–37, 2015.

[99] R S Stowers, S C Allen, and L J Suggs. Dynamic phototuning of 3D hydrogel stiffness. *Proceedings of the National Academy of Sciences of the United States of America*, 112(7):1953–1958, 2015.

[100] Oju Jeon, Kamal H. Bouhadir, Joseph M. Mansour, and Eben Alsberg. Photocrosslinked alginate hydrogels with tunable biodegradation rates and mechanical properties. *Biomaterials*, 30(14):2724–2734, may 2009.

[101] M M Stanton, J Samitier, and S Sánchez. Lab on a Chip. *Lab on a Chip*, 15:3111–3115, 2015.

[102] Therese Andersen, Pia Auk-Emblem, and Michael Dornish. 3d cell culture in alginate hydrogels. *Microarrays*, 4(2):133–161, 2015.

[103] Eric Valeur and Mark Bradley. Amide bond formation: Beyond the myth of coupling reagents. *Chemical Society Reviews*, 38(2):606–631, 2009.

[104] J B Xu, J P Bartley, and R A Johnson. Preparation and characterization of alginate hydrogel membranes crosslinked using a water-soluble carbodiimide. *Journal of Applied Polymer Science*, 90(3):747–753, 2003.

[105] Tarfah I Al-Warhi, Hassan M A Al-Hazimi, and Ayman El-Faham. Recent development in peptide coupling reagents. *Journal of Saudi Chemical Society*, 16(2):97–116, 2012.

[106] Christine E. Garrett, Xinglong Jiang, Kapa Prasad, and Oljan Repič. New observations on peptide bond formation using CDMT. *Tetrahedron Letters*, 43(23):4161–4165, 2002.

[107] Zhiquan Li, Jan Torgersen, Aliasghar Ajami, Severin Mühleder, Xiaohua Qin, Wolfgang Husinsky, Wolfgang Holnthoner, Aleksandr Ovsianikov, Jürgen Stampfl, and Robert Liska. Initiation efficiency and cytotoxicity of novel water-soluble two-photon photoinitiators for direct 3D microfabrication of hydrogels. *RSC Advances*, 3:15939, 2013.

[108] Arturo J Vegas, Omid Veiseh, Joshua C Doloff, Minglin Ma, Hok Hei Tam, Kaitlin Bratlie, Jie Li, Andrew R Bader, Erin Langan, Karsten Olejnik, Patrick Fenton, Jeon Woong Kang, Jennifer Hollister-Locke, Matthew A Bochenek, Alan Chiu, Sean Siebert, Katherine Tang, Siddharth Jhunjhunwala, Stephanie Aresta-Dasilva, Nimit Dholakia, Raj Thakrar, Thema Vietti, Michael Chen, Josh Cohen,

Karolina Siniakowicz, Meirigeng Qi, James McGarrigle, Stephen Lyle, David M Harlan, Dale L Greiner, Jose Oberholzer, Gordon C Weir, Robert Langer, and Daniel G Anderson. Combinatorial hydrogel library enables identification of materials that mitigate the foreign body response in primates. *Nature Biotechnology*, (February 2015), 2016.

[109] E G, V K, and A Nudelman. NMR Chemical Shifts of Common Laboratory Solvents as Trace Impurities. 3263:7512–7515, 1997.

[110] Andrew L. Hook, Chien Yi Chang, Jing Yang, Steve Atkinson, Robert Langer, Daniel G. Anderson, Martyn C. Davies, Paul Williams, and Morgan R. Alexander. Discovery of novel materials with broad resistance to bacterial attachment using combinatorial polymer microarrays. *Advanced Materials*, 25(18):2542–2547, 2013.

[111] Erin R. West, Min Xu, Teresa K. Woodruff, and Lonnie D. Shea. Physical properties of alginate hydrogels and their effects on in vitro follicle development. *Biomaterials*, 28(30):4439–4448, 2007.

[112] Prakriti Tayalia, Cleber R Mendonca, Tommaso Baldacchini, David J Mooney, and Eric Mazur. 3d cell-migration studies using two-photon engineered polymer scaffolds. *Advanced materials*, 20(23):4494–4498, 2008.

[113] An I Van Den Bulcke, Bogdan Bogdanov, Nadine De Rooze, Etienne H Schacht, Maria Cornelissen, and Hugo Berghmans. Structural and rheological properties of methacrylamide modified gelatin hydrogels. *Biomacromolecules*, 1(1):31–38, 2000.

[114] H Staudinger and E Husemann. Über hochpolymere verbindungen, 116. mitteil.: Über das begrenzt quellbare poly-styrol. *Berichte der deutschen chemischen Gesellschaft (A and B Series)*, 68(8):1618–1634, 1935.

[115] Thomas Holt and William Simpson. Observations on intramolecular reaction in addition polymerization systems. *Proceedings of the Royal Society of London. Series A. Mathematical and Physical Sciences*, 238(1213):154–174, 1956.

[116] Jennifer S Young and Christopher N Bowman. Effect of polymerization temperature and cross-linker concentration on reaction diffusion controlled termination. *Macromolecules*, 32(19):6073–6081, 1999.

[117] Hong-Bo Sun, Makoto Maeda, Kenji Takada, James WM Chon, Min Gu, and Satoshi Kawata. Experimental investigation of single voxels for laser nanofabrication via two-photon photopolymerization. *Applied physics letters*, 83(5):819–821, 2003.

[118] Claude Martineau, R Anémian, C Andraud, I Wang, M Bouriau, and PL Baldeck. Efficient initiators for two-photon induced polymerization in the visible range. *Chemical physics letters*, 362(3-4):291–295, 2002.

[119] Gustavo de Miguel, Giuseppe Vicidomini, Benjamin Harke, and Alberto Diaspro. Linewidth and writing resolution. In *Three-Dimensional Microfabrication Using Two-photon Polymerization*, pages 190–220. Elsevier, 2016.

[120] Barbara Pui Chan, Jiao Ni Ma, Jin Ye Xu, Chuen Wai Li, Jin Ping Cheng, and Shuk Han Cheng. Femto-second Laser-based free writing of 3D protein microstructures and micropatterns with Sub-micrometer features: A study on voxels, porosity, and cytocompatibility. *Advanced Functional Materials*, 24(3):277–294, 2014.

[121] Tommaso Baldacchini and Ruben Zadoyan. In situ and real time monitoring of two-photon polymerization using broadband coherent anti-stokes raman scattering microscopy. *Opt. Express*, 18(18):19219–19231, Aug 2010.

[122] Hansoo Park, Xuan Guo, Johnna S Temenoff, Yasuhiko Tabata, Arnold I Caplan, F Kurtis Kasper, and Antonios G Mikos. Effect of swelling ratio of injectable hydrogel composites on chondrogenic differentiation of encapsulated rabbit marrow mesenchymal stem cells in vitro. *Biomacromolecules*, 10(3):541–546, 2009.

[123] Steven L Percival, Louise Suleman, Claudia Vuotto, and Gianfranco Donelli. Healthcare-associated infections, medical devices and biofilms: risk, tolerance and control. *Journal of medical microbiology*, 64(4):323–334, 2015.

[124] J William Costerton. Cystic fibrosis pathogenesis and the role of biofilms in persistent infection. *Trends in microbiology*, 9(2):50–52, 2001.

[125] Frank P Barry and J Mary Murphy. Mesenchymal stem cells: clinical applications and biological characterization. *The international journal of biochemistry & cell biology*, 36(4):568–584, 2004.

[126] Michael J Poellmann, Patrick A Harrell, William P King, and Amy J Wagoner Johnson. Geometric microenvironment directs cell morphology on topographically patterned hydrogel substrates. *Acta biomaterialia*, 6(9):3514–3523, 2010.

[127] Murat Guvendiren and Jason A Burdick. The control of stem cell morphology and differentiation by hydrogel surface wrinkles. *Biomaterials*, 31(25):6511–6518, 2010.

[128] Carson H Thomas, Joel H Collier, Charles S Sfeir, and Kevin E Healy. Engineering gene expression and protein synthesis by modulation of nuclear shape. *Proceedings of the National Academy of Sciences*, 99(4):1972–1977, 2002.

[129] Kristopher A Kilian, Branimir Bugarija, Bruce T Lahn, and Milan Mrksich. Geometric cues for directing the differentiation of mesenchymal stem cells. *Proceedings of the National Academy of Sciences*, 107(11):4872–4877, 2010.

[130] Caroline Ceccaldi, Sophie Girod Fullana, Chiara Alfarano, Olivier Lairez, Denis Calise, Daniel Cussac, Angelo Parini, and Brigitte Sallerin. Alginate scaffolds for mesenchymal stem cell cardiac therapy: influence of alginate composition. *Cell transplantation*, 21(9):1969–1984, 2012.

[131] Giulio Abagnale, Michael Steger, Vu Hoa Nguyen, Nils Hersch, Antonio Sechi, Sylvia Joussen, Bernd Denecke, Rudolf Merkel, Bernd Hoffmann, Alice Dreser, et al. Surface topography enhances differentiation of mesenchymal stem cells towards osteogenic and adipogenic lineages. *Biomaterials*, 61:316–326, 2015.

[132] Frits FB Hulshof, Bernke Papenburg, Aliaksei Vasilevich, Marc Hulsman, Yiping Zhao, Marloes Levers, Natalie Fekete, Meint De Boer, Huipin Yuan, Shantanu Singh, et al. Mining for osteogenic surface topographies: In silico design to in vivo osseo-integration. *Biomaterials*, 137:49–60, 2017.

[133] Kenneth K Chung, James F Schumacher, Edith M Sampson, Robert A Burne, Patrick J Antonelli, and Anthony B Brennan. Impact of engineered surface microtopography on biofilm formation of staphylococcus aureus. *Biointerphases*, 2(2):89–94, 2007.

[134] Shravanthi T Reddy, Kenneth K Chung, Clinton J McDaniel, Rabih O Darouiche, Jaime Landman, and Anthony B Brennan. Micropatterned surfaces for reducing the risk of catheter-associated urinary tract infection: an in vitro study on the effect of sharklet micropatterned surfaces to inhibit bacterial colonization and migration of uropathogenic escherichia coli. *Journal of endourology*, 25(9):1547–1552, 2011.

[135] Jaione Valle, Saioa Burgui, Denise Langheinrich, Carmen Gil, Cristina Solano, Alejandro Toledo-Arana, Ralf Helbig, Andrés Lasagni, and Iñigo Lasa. Evaluation of Surface Microtopography Engineered by Direct Laser Interference for Bacterial Anti-Biofouling. *Macromolecular Bioscience*, 15(8):1060–1069, 2015.

[136] Lillian C. Hsu, Jean Fang, Diana A. Borca-Tasciuc, Randy W. Worobo, and Carmen I. Moraru. Effect of micro- and nanoscale topography on the adhesion of bacterial cells to solid surfaces. *Applied and Environmental Microbiology*, 79(8):2703–2712, 2013.

[137] David Perera-costa and Jose Morales Bruque. Studying the In fl uence of Surface Topography on Bacterial Adhesion using Spatially Organized Microtopographic Surface Patterns. 2014.

[138] SA Bezman, PA Burtis, TPJ Izod, and MA Thayer. Photodynamic inactivation of e. coli by rose bengal immobilized on polystyrene beads. *Photochemistry and photobiology*, 28(3):325–329, 1978.

[139] David Gwilym Davies, Ananda M Chakrabarty, and Gill G Geesey. Exopolysaccharide production in biofilms: substratum activation of alginate gene expression by pseudomonas aeruginosa. *Appl. Environ. Microbiol.*, 59(4):1181–1186, 1993.

[140] Thomas B May and AM Chakrabarty. Pseudomonas aeruginosa: genes and enzymes of alginate synthesis. *Trends in microbiology*, 2(5):151–157, 1994.

[141] Kathryn A Whitehead and Joanna Verran. The effect of surface topography on the retention of microorganisms. *Food and bioproducts processing*, 84(4):253–259, 2006.

[142] Priyalakshmi Viswanathan, Matthew G Ondeck, Somyot Chirasatitsin, Kamolchanok Ngamkham, Gwendolen C Reilly, Adam J Engler, and Giuseppe Battaglia. 3d surface topology guides stem cell adhesion and differentiation. *Biomaterials*, 52:140–147, 2015.

[143] Christopher J Bettinger, Robert Langer, and Jeffrey T Borenstein. Engineering substrate topography at the micro-and nanoscale to control cell function. *Angewandte Chemie International Edition*, 48(30):5406–5415, 2009.

[144] Rajat K Das and Omar F Zouani. A review of the effects of the cell environment physicochemical nanoarchitecture on stem cell commitment. *Biomaterials*, 35(20):5278–5293, 2014.

[145] Kristan S Worthington, Anh-Vu Do, Rasheid Smith, Budd A Tucker, and Aliasger K Salem. Two-photon polymerization as a tool for studying 3d printed topography-induced stem cell fate. *Macromolecular bioscience*, 19(2):1800370, 2019.

[146] Hemant V Unadkat, Marc Hulsman, Kamiel Cornelissen, Bernke J Papenburg, Roman K Truckenmüller, Anne E Carpenter, Matthias Wessling, Gerhard F Post, Marc Uetz, Marcel JT Reinders, et al. An algorithm-based topographical biomaterials library to instruct cell fate. *Proceedings of the National Academy of Sciences*, 108(40):16565–16570, 2011.

Appendix A

Appendix 1

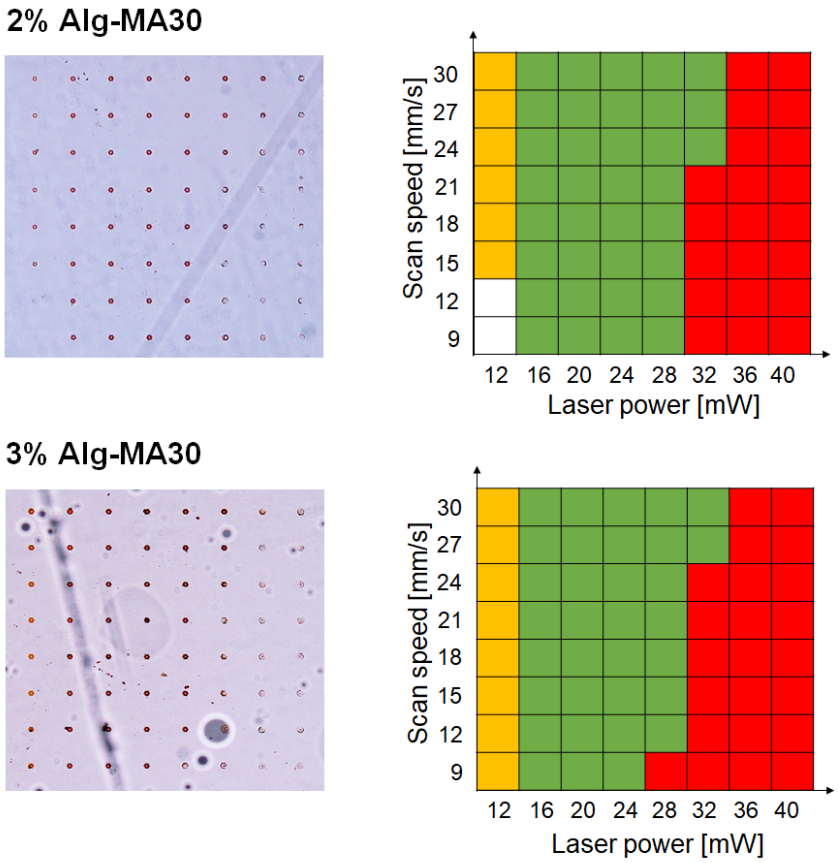


Fig. A.1 Bright-field images of energy dose array for 2% and 3% w/v Alg-MA30 with the associated processing windows.

Table A.1 Raw viscosity values for various alginate concentrations and DoF of alginate with methacrylate groups.

	1st	2nd	3rd
Alg-MA 18, 1%	5.688857	5.970945	5.721681
Alg-MA 18, 2%	10.44079	10.54278	10.51227
Alg-MA 18, 3%	16.63736	16.40409	16.47245
Alg-MA 30, 1%	6.542578	6.226316	6.67372
Alg-MA 30, 2%	10.65494	10.67474	10.57696
Alg-MA 30, 3%	20.62454	20.70252	20.89199
Alg-MA 40, 1%	6.971127	6.650664	6.867297
Alg-MA 40, 2%	11.92054	11.94739	11.58881
Alg-MA 40, 3%	22.08203	21.79806	21.91035